SOLAR ULTRAVIOLET RADIATION PREDICTIONS UNDER CLOUD COVER EFFECTS WITH ARTIFICIAL INTELLIGENCE APPROACHES

A Thesis submitted by

Salvin Sanjesh Prasad
BSc (Mathematics & Physics), PGCE (Education), MSc (Physics)

For the award of

Doctor of Philosophy

2023

ABSTRACT

Solar ultraviolet (UV) radiation causes deleterious health effects on the skin and eyes. Skin-based malignant keratinocyte cancers, cataracts, and pterygium can be triggered by prolonged UV radiation exposure. In plants, UV radiation can damage photosynthetic processes. To address these pressing issues, this doctoral thesis developed computationally efficient artificial intelligence (AI) predictive frameworks to deliver early warnings of sun exposure times through short-term forecasting of solar UV radiation in terms of ultraviolet index (UVI) and UV radiation in category A (UV-A), with model explanations. The first objective is to develop an AI model which integrates cloud chromatic properties from sky images to forecast short-term UVI at multiple time-step horizons. The UVI forecast is generated for the four seasons of autumn, summer, spring and winter for the Toowoomba, Queensland study site in Australia that receives a high UV exposure. For the second objective, we design an AI model incorporating cloud statistical properties extracted from sky images to forecast 20-minute ahead UV-A in Toowoomba. The proposed model is calibrated through uncertainty quantification to improve predictive performance, model reliability, and generate interpretable results. In the third objective, explainable AI (xAI) is applied to forecast hourly UVI using satellite-derived predictor variables and to provide model-agnostic explanations for four Australian hotspots affected by solar UV radiation. The model is explained locally with local interpretable model-agnostic explanations (LIME) and globally with Shapley additive explanations (SHAP) and permutation feature importance (PFI). The objective model trained with satellite-derived cloud cover conditions, aerosol effects, precipitation and ozone effects extends its applicability to other geographical locations, especially in remote regions. In order to help mitigate skin and eye health risks under stochastic cloud cover conditions, the outcomes of this PhD research are expected to serve as a promising decision-support tool for delivering more accurate sun-protection times to the public. The findings can also facilitate further studies into the harmful effects of UV radiation on terrestrial plants and animals. The xAI-generated model explanations provide information on the predictive contributions of each satellite-derived variable to improve model predictability, stability, and trustworthiness for end-users. This overcomes the complex problem of UV radiation intermittency. The overall research outcomes of this project can provide a real-time UV predictive framework for the health sector, industry, government, and major stakeholders.

CERTIFICATION OF THESIS

I Salvin Sanjesh Prasad declare that the PhD Thesis entitled *Solar Ultraviolet Radiation Predictions under Cloud Cover Effects with Artificial Intelligence Approaches* is not more than 100,000 words in length including quotes and exclusive of tables, figures, appendices, bibliography, references, and footnotes.

This thesis is the work of Salvin Sanjesh Prasad except where otherwise acknowledged, with the majority of the contribution to the papers presented as a Thesis by Publication undertaken by the student. The work is original and has not previously been submitted for any other award, except where acknowledged.

Date: 21/09/2023

Endorsed by:

Professor Ravinesh C. Deo
Principal Supervisor

Associate Professor Nathan Downs
Associate Supervisor

Honorary Professor Alfio V. Parisi
Associate Supervisor

Dr. Damien Igoe
External Supervisor

Professor Jeffrey Soar
Associate Supervisor

Student and supervisors' signatures of endorsement are held at the University.

STATEMENT OF CONTRIBUTION

This PhD thesis by publications has produced 3 high quality (*Quartile* 1) publications during the candidature. The details of joint authorship and agreed share of these contributions in the publications are detailed as follows:

Paper 1 (Chapter 4):

Prasad, S. S., Deo, R. C., Downs, N., Igoe, D., Parisi, A. V., & Soar, J. (2022). Cloud affected solar UV prediction with three-phase wavelet hybrid convolutional long short-term memory network multi-step forecast system, *IEEE Access,* 10, 24704-24720. https://doi.org/10.1109/ACCESS.2022.3153475. (Scopus Ranked *Q1*; Impact Factor: *3.9*, SNIP: *1.734*; *92nd percentile* in category: Engineering - Engineering (all)).

Salvin S. Prasad contributed 70% to this paper. Collectively Ravinesh C. Deo, Nathan Downs, Damien Igoe and Jeffrey Soar contributed the remainder.

Paper 2 (Chapter 5):

Prasad, S. S., Deo, R. C., Downs, N., Casillas-Perez, D., Salcedo-Sanz, S., & Parisi, A. (2023). Very Short-Term Solar Ultraviolet-A Radiation Forecasting System with Cloud Cover Images and a Bayesian Optimized Interpretable Artificial Intelligence Model, *Expert Systems with Applications*, 236, 121273. https://doi.org/10.1016/j.eswa.2023.121273. (Scopus Ranked *Q1*; Impact Factor: *8.665*, SNIP: *2.696*; *97th percentile* in category: Engineering - General Engineering).

Salvin S. Prasad contributed 75% to this paper. Collectively Ravinesh C. Deo, Nathan Downs, David Casillas-P´erez and Sancho Salcedo-Sanz contributed the remainder.

Paper 3 (Chapter 6):

Prasad, S. S., Deo, R. C., Downs, N., Casillas-Perez, D., Salcedo-Sanz, S., & Parisi, A. (2023). Enhanced joint hybrid deep neural networks explainable artificial intelligence model with satellite-derived predictor variables for solar ultraviolet index prediction, *Computer Methods and Programs in Biomedicine,* 241, 107737. https://doi.org/10.1016/j.cmpb.2023.107737. (Scopus Ranked *Q1*; Impact Factor: *7.027*, SNIP: *2.08*; *92nd percentile* in category: Medicine - Health Informatics).

Salvin S. Prasad contributed 80% to this paper. Collectively Ravinesh C. Deo, Nathan Downs, David Casillas-P´erez and Sancho Salcedo-Sanz contributed the remainder.

ACKNOWLEDGEMENTS

In completion of this research project, I wish to acknowledge the joint support of my supervisory team, institutions, and other incredible individuals. My PhD journey, accomplished with publications in high impact factor journals would not have been successful without their valuable assistance and scientific guidance. Firstly, I would convey my sincere appreciation and gratitude to my Principal Supervisor, Professor Ravinesh C. Deo for playing an instrumental role in delivering tireless support and timely feedback towards achieving all my research milestones. I duly appreciate his motivation, inspiration and words of encouragement during the crucial phases of designing hybridized models.

I would further express my appreciation to all the associate supervisors who were Associate Professor Nathan Downs, Honorary Professor Alfio V. Parisi, Dr Damien Igoe and Professor Jeffrey Soar. A special thanks to Associate Professor Nathan Downs and Honorary Professor Alfio V. Parisi for providing UV radiation-related scientific advice and knowledge on accessing/processing datasets from the Spectroradiometer, Biometer and Total Sky Imager. In accomplishing objective 1 of my PhD research, I would thank Dr Damien Igoe for his essential guidance on extracting cloud statistical properties from sky images and Professor Jeffrey Soar for sharing his expertise and important suggestions.

I would also offer my appreciation to the external international supervisors, Dr. David Casillas-P´erez and Professor Sancho Salcedo-Sanz for their valuable contributions towards accomplishing objectives 2 and 3 of my PhD research. I further thank them for sharing their expertise in using the Latex software.

I take this opportunity to thank the University of Southern Queensland (UniSQ), in particular, the Graduate Research School (GRS) for eventuating this research and awarding the International PhD Research and Stipend Scholarship. I am also grateful to the School of Mathematics, Physics and Computing for extending support and guidance when needed. I would also thank my research colleagues from the Advanced Data Analytics: Environmental Modelling and Simulation Group (led by Professor Ravinesh C. Deo) for constructive discussions and research-related brainstorming.

Finally, I am thankful to my parents, wife and kids for their enormous support and encouragement throughout the duration of my PhD research. I also acknowledge all my friends and family for their words of encouragement towards my PhD studies.

DEDICATION

This PhD thesis is warmly dedicated to the dearest people of my life, my parents Mr Surendra Prasad and Mrs Manjita Prasad, My wife Kaleshni Vandhana and my kids Shivek, Krishnav and Maithili.

TABLE OF CONTENTS

LIST OF TABLES

LIST OF FIGURES

ABBREVIATIONS

AB	Adaboost
AI	Artificial Intelligence
ANN	Artificial Neural Network
ARPANSA	Australian Radiation Protection and Nuclear Safety Agency
BiLSTM	Bidirectional Long Short-Term Memory
BRR	Bayesian Ridge Regression
CCF	Cross-Correlation Functions
CNN	Convolution Neural Network
ConvLSTM	Convolutional Long Short-Term Memory
DL	Deep Learning
DM	Diebold-Mariano
DNN	Deep Neural Network
DT	Decision Tree
DWT	Discrete Wavelet Transform
ELM	Extreme Learning Machine
FCN	Fully Convolutional Network
GIOVANNI	Goddard Online Interactive Visualization and Analysis Infrastructure
ICNIRP	International Commission on Non-Ionizing Radiation Protection
LIME	Local Interpretable Model-Agnostic Explanations
LM	Legates-Mccabe's Index
LSTM	Long Short-Term Memory
MAE	Mean Absolute Error
MERRA	Moder n-Era Retrospective Analysis for Research and Applications
ML	Machine Learning
MLP	Multilayer Perceptrons
NASA	National Aeronautics and Space Administration
N-BEATS	Neural Basis Expansion Analysis for Interpretable Time Series
NCA	Neighbourhood Component Analysis

NSE	Nash–Sutcliffe Efficiency
NT	Northern Territory
PA	Passive-Aggressive
PACF	Partial Autocorrelation Function
PFI	Permutation Feature Importance
QLD	Queensland
r	Pearson’s Correlation Coefficient
r_{cross}	Cross-Correlation Coefficient
RF	Random Forest
RMAE	Relative Mean Absolute Error
RMSE	Root Mean Square Error
RRMSE	Relative Root Mean Square Error
SGD	Stochastic Gradient Descent
SHAP	Shapley Additive Explanations
SS	Skill Score
SVR	Support Vector Regression
SWT	Stationary Wavelet Transform
SZA	Solar Zenith Angle
UNEP	United Nations Environment Programme
UniSQ	University of Southern Queensland
UV	Ultraviolet
UV-A	Ultraviolet Radiation in Category A
UV-B	Ultraviolet Radiation in Category B
UV-C	Ultraviolet Radiation in Category C
UVI	Ultraviolet Index
WHO	World Health Organization
WI	Willmott's Index
WMO	World Meteorological Organization
xAI	Explainable Artificial Intelligence

CHAPTER 1: INTRODUCTION

1.1. Background

Exposure to solar ultraviolet (UV) radiation in the waveband of 280-400 nm poses both detrimental and beneficial effects on people and the terrestrial life of animals and plants. Since ancient days, UV exposure has been significantly beneficial for the production of sufficient vitamin D in human bodies to strengthen bones, muscles and the entire immune system (Juzeniene & Moan 2012). UV radiation has been utilized in the food and water industries as an effective disinfectant that inactivates disease-causing micro-organisms (Hijnen et al. 2006). Further application of UV radiation was significant during the recent COVID-19 pandemic for disinfecting surfaces contaminated with the novel coronavirus (Heilingloh et al. 2020). Though UV exposure has some important benefits, the overriding harmful effects have become a major concern. Prolonged exposure to UV irradiance in plants can cause temporary or irreversible destruction to the process of photosynthesis due to the damage triggered in the genetic system and cell membrane (Piri et al. 2011). Elevated UV exposure in animals creates oxidative stress on the skin through excessive production of reactive oxygen species and the consequences can cause cell damage, cell ageing or cancer (Olarte Saucedo et al. 2019). Among all living beings, UV exposure risks to human health have become the most pressing concern for the health sector. Exposure to erythemally-effective UV radiation poses deleterious effects on humans by causing skin-based diseases that include malignant keratinocyte cancers (Deo et al. 2017). Additionally, such exposure risks induce eye health ailments, including cataracts and pterygium (Turner et al. 2020). Overall, the deleterious UV-exposure risks on humans and terrestrial plant and animal life have become a serious concern.

UV-radiation exposure-associated skin cancers are more prevalent among populations of fair skin type, especially for those residing in countries having high ambient temperatures. On a global basis, the skin cancer-led death rates for these countries are quite substantial. For instance, the global skin cancer mortality statistics for the year 2018 recorded 126,000 deaths (Parker 2021). Furthermore, the global statistics for the year 2021 revealed that Australia and New Zealand were the most affected countries, recording the highest incidence of melanoma and keratinocyte

carcinoma (Gordon, Leung, et al. 2022). Therefore, it is crucial that the aforementioned UV exposure risks and subsequent damaging effects are well monitored and explored.

The UV spectrum is categorized by photobiologists into the three spectral ranges of UV-A (320-400 nm), UV-B (280-320 nm) and UV-C (100-280 nm) wavebands. Among them, the UV-C waveband is filtered completely by stratospheric oxygen, ozone and atmospheric moisture, while the UV-A and UV-B wavebands are moderated by ozone, suspended aerosols and clouds before reaching the earth's surface (DeBuys et al. 2000). Exposure to the UV-B waveband is highly harmful and carcinogenic (Diffey et al. 1982). High doses of UV-A radiation are also linked to elevated risks of skin cancer as it is abundantly available and the harmful rays are capable of penetrating much deeper into the skin tissues to cause severe biological damage (DeBuys et al. 2000). To implement sun protection from ground-level UV-exposure effects, the World Health Organization (WHO), International Commission on Non-Ionizing Radiation Protection (ICNIRP), World Meteorological Organization (WMO) and United Nations Environment Programme (UNEP) developed the global solar ultraviolet index (UVI) as a numerical public health indicator to help mitigate skin and eye health risks (World Health Organization et al. 2002). The numerical-scale for UVI ranges from 0 to 11^{+}, whereby an increase in these values indicates a rise in the severity exposure risk of UV irradiance. Practically, the estimations of UV irradiance have been acquired through surface and satellite measurement systems and by designing physical models, which frequently entailed some modelling constraints (Deo et al. 2017). The limitations of these measurement systems have led to a need for designing a more intelligent tool that could robustly provide UV radiation exposure information.

To address the aforementioned gaps in knowledge, artificial intelligence (AI) inspired predictive frameworks are state-of-art alternatives that are currently gaining more prominence over traditional measurement systems and conventional predictive models. Unlike the measurement and physical modelling methods, the AI-based data-driven frameworks are cost-effective and accessible for most remote locations. These data-driven frameworks, which include machine learning (ML) and advanced deep learning (DL) models, can efficiently capture relevant predictive elements from historical datasets to generate highly accurate and flexible future predictions (Ghimire et al. 2019b). Having remarkable predictive performance, these ML and DL models

are highly applicable to the solar UV radiation forecasting domain which is influenced strongly by the dynamic nature of the atmosphere.

1.2. **Statement of the problem**

Solar UV-exposure-related skin diseases and eye health ailments have burdened most health sectors in many temperate countries across the globe. For Australians, the health sector is highly burdened by the skin-associated public health problem with an estimated expense of 1.7 billion dollars every year (Gordon, Shih, et al. 2022). In regards to the mortality rate, a survey in the year 2019 reported 1,726 death cases with cutaneous malignant melanoma and 714 deaths with keratinocyte cancer (squamous cell carcinoma and basal cell carcinoma) for this country (Dexter et al. 2020). To address this critical issue and minimize the associated excessive healthcare costs, innovative decision support tools designed using expert AI-based predictive systems can be applied for delivering real-time sun exposure information to the public for mitigating UV-exposure-related health risks at various locations in Australia that place the population at risk of potentially harmful exposures.

A number of predictor variables are known to influence the incident UV radiation on the earth's surface and these inputs can successfully be integrated with AI frameworks for generating more efficient and flexible UV radiation dynamic prediction. An important atmospheric variable that poses a significant effect on ground-level UV irradiance is the stochastic cloud cover conditions. Cloud scatters short wavelength UV radiation. Often, incident UV radiation is scattered back into space, reducing the surface irradiance. At times this radiation can also be backscattered towards the surface. Generally, an increase in cloud cover results in the attenuation of the UV irradiance with increasing wavelength (Aun et al. 2011). Under unbroken cloud cover conditions, the solar UV irradiance reduces by 50 to 60% with increasing wavelengths and during precipitation, it reduces even further (Allaart et al. 2004). However, under partial intermittent cloud cover conditions, the scattering of solar UV radiation can trigger escalated UV spikes on the earth's surface that exceed the nominal cloud-free surface UV irradiance (Deo et al. 2017). The sudden escalated spikes in ground-level UV radiation can impose even more severe UV exposure-associated damaging effects on the skin and eyes. So far, a minimal number of studies have examined cloud cover effects, particularly the cloud statistical properties extracted from the sky images as

inputs for model building suited to a machine learning process that can improve UV radiation predictions.

Another predictor variable that influences the level of UV radiation is the solar zenith angle (SZA). As the incident radiation transverses through the earth's atmosphere, the attribute of SZA governs the optical path length (Pecenak et al. 2016). In a recent study, SZA has been utilized as an input predictor to forecast solar UVI (Deo et al. 2017). However, SZA has not been integrated with intermittent cloud cover effects in any previous research for simulating solar UV radiation using AI technology. Stratospheric ozone and aerosol effects are other meteorological variables that impact ground-level UV radiation through absorption and scattering (Downs et al. 2016). All these aforementioned attributes have not been collectively integrated with the stochastic cloud cover effects to train an AI-based model for generating more accurate predictions of ground-level UV radiation (UV-A and UV-B) or UVI for various Australian hotspots, including locations at risk of elevated UV radiation exposure.

Some previous studies have applied AI-powered standalone ML and DL models to forecast UVI in some temperate countries (Latosińska et al. 2015; Deo et al. 2017; Oliveira et al. 2020). In comparison with classical standalone models, hybrid AI models through several feature selection, feature decomposition and feature extraction stages can efficiently capture most compound relationships within the input features for delivering more accurate predictive outputs (Ahmed et al. 2021). Feature selection with wrapper-based and filter-based methods is capable of a robust selection of the pertinent features from any given pool of attributes (Selvakumar & Muneeswaran 2019). These powerful algorithms can capture important feature information to enhance the predictive performance and reduce the feature dimensionality for achieving high computational efficiency.

Some recent studies have recommended that feature extraction using a remarkable convolution neural network (CNN) can improve the model prediction skills (Zhang et al. 2020). On the other hand, the application of stationary wavelet transform (SWT) can also enhance the predictive performance through high-frequency and low-frequency decompositions of the atmospheric variable datasets using stationary wavelet transform (SWT). The SWT algorithm can greatly improve the efficacy of non-stationarity behaviour, periodicity, noise and random fluctuations in the input variables over the temporal scales (Ospina et al. 2019). Considering the complex behaviour and intermittency issue of UV radiation variables, the aforementioned hybridized AI

frameworks can also be designed and explored for further performance enhancement in simulating more accurate UV predictions for various Australian hotspots receiving high UV radiation exposure.

In terms of predictive performance, comparisons of ML and DL methods reveal that most researchers prefer to apply the latter algorithm as it can eminently handle large datasets and issues of overfitting led by the intricate and non-linear interactions between the input variables (Ghimire et al. 2019a). The ensemble framework constructed by training a single DL model on different loss functions can be calibrated through uncertainty quantification to further enhance the predictive performance and model reliability (Stevenson et al. 2022). So far, such an ensemble approach has not been designed and calibrated through uncertainty quantification for any UV radiation predictive system. Furthermore, the architecture of the DL models is of a “black-box” type, where the internal workings are non-explainable complicated networks (Machlev et al. 2022). Explainable artificial intelligence (xAI) methods can enable end-users and decision-makers to obtain more interpretable and transparent outcomes from the DL models to further affirm the model’s trustworthiness (Saleem et al. 2022). The xAI tool can robustly offer local and global model-agnostic explanations of the predictions made by the “black-box” DL models. Some recent studies have used the local interpretable model-agnostic explanations (LIME) to offer local explanations of the instance-based “black-box” model predictions (Petch et al. 2022). Other studies have employed the Shapley additive explanations (SHAP) and permutation feature importance (PFI) frameworks to interpret the entire decisions on the outcomes of the “black-box” predictive models (Chaibi et al. 2021). On the same notion, no previous study has applied the model-agnostic tools in the xAI domain to offer local or global model explanations on how the individual atmospheric predictors impact the predictions of ground-level UV radiation.

Overall, this doctoral thesis intends to confront issues concerning pertinent input selection, non-linearity and non-stationarity of the input predictors in the context of predicting ground-level UV radiation over short-term forecast horizons by designing hybrid DL frameworks for different seasons, as well as for various Australian locations at risk of receiving elevated UV irradiance under dynamic atmospheric conditions. The research further anticipates calibrating an ensemble of several single-point DL models trained on different key loss functions via uncertainty quantification to enhance the predictive performance and model reliability. Additionally, the study integrates the xAI

tools with the DL “back-box” models to explore the local and global model-agnostic explanations on the contributions of individual atmospheric variables towards generating UV radiation forecasts with the DL back-box models.

1.3. **Objectives**

The key aim of this doctoral research, presented as a collection of journal papers was to develop innovative decision-support systems using high-precision AI-inspired modelling strategies capable of forecasting short-term UV radiation in terms of the UVI and UV-A for various Australian hotspots that record high ambient UV radiation. In accomplishing the proposed aim, this research project adopted a plethora of hybridized DL and ML techniques to address three distinct objectives that are presented as a collection of Quartile 1 (Q1) papers in this doctoral thesis. Sequentially, this research addressed the following specific objectives:

Objective 1: ***Develop a three-phase wavelet hybrid deep learning model for a short-term forecast of the cloud-affected UVI at multiple time-step horizons.***

- To design a hybridized UVI forecasting model by integrating BorutaShap for feature selection, SWT for data decomposition and Optuna optimizer for hyperparameter tuning with convolutional long short-term memory (convLSTM) network. The research incorporated cloud statistical properties extracted from sky images (that define the cloud cover conditions) and SZA as input predictors to forecast short-term UVI for the experimental site in Toowoomba (latitude of 27.60 °S and longitude of 153.93 °E), Queensland. The multi-step forecasts were generated at 10 min, 20 min, 30 min and hourly horizons. The enhanced performance of the newly developed hybrid model was validated using other hybrid DL and ML competing counterpart models.
- The outcome of this research has been published in the *IEEE Access* journal, ranked as Q1 (2022, Vol. 10, Pages 24704–24720).

Objective 2: ***Design and calibrate a hybrid ensemble deep learning model through uncertainty quantification for further enhancement of performance and model reliability in forecasting short-term UV-A radiation.***

- To develop a hybrid DL neural basis expansion analysis for interpretable time series (N-BEATS) model by adopting an ensemble approach, together with the application of neighbourhood component analysis (NCA) for input selection and a Bayesian optimizer for hyperparameter tuning. An ensemble of 15 single-point N-BEATS models was constructed by training five single-point N-BEATS models on three different key loss functions. The model trained on cloud statistical properties and SZA forecasted a 20-minute ahead UV-A for four different seasons and its performance was validated using other hybrid DL and ML benchmarked models for the Toowoomba-based experimental site. The newly prescribed hybrid ensemble model was further calibrated through uncertainty quantification to enhance the predictive performance and model reliability.
- The outcome of this research has been published in the *Expert Systems with Applications* journal, ranked as Q1 (2023, Vol. 236, page 121273).

Objective 3: ***Construct an enhanced joint hybrid deep learning framework with explainable artificial intelligence (xAI) tools for delivering UVI predictions with model-agnostic explanations.***

- To design an enhanced joint hybrid DL model by applying dual-phase feature selection, a Bayesian optimizer algorithm for hyperparameter tuning and xAI model-agnostic tools with deep neural network (DNN) for obtaining model explanations on UVI predictions. Local instance-based model explanations on UVI predictions were extracted using LIME, while the global explanations were achieved using SHAP and PFI. The proposed model was trained on satellite-derived meteorological variables, SZA and historical lagged memory of UVI extracted from the Australian Radiation Protection and Nuclear Safety Agency (ARPANSA) to forecast hourly horizon UVI for four Australian hotspots subjected to high ambient UV radiation and validated with other robust benchmarked models. These hotspots were Darwin (12.43 °S and 130.89 °E), Alice Springs (23.80 °S and 133.89 °E), Townsville (23.53 °S and 148.16 °E) and Emerald (19.33 °S and 146.76 °E). Having trained on the satellite-derived cloud cover effects, aerosol scattering and ozone effect datasets, the newly

developed explainable UVI forecasting framework can be applied to similar tropical to sub-tropical countries facing UV-exposure-related health risks.

- The outcome of this research has been published in the *Computer Methods and Programs in Biomedicine* journal, ranked as Q1 (2023, Vol. 241, page 107737).

1.4. **Research significance**

The findings of this research are highly significant for Australia, particularly for the populated hotspots that are subjected to high ground-level UV exposures. While UV exposure is deleterious for people, it is also harmful to the terrestrial animal and plant life in this country (Parisi & Kimlin 1999). In particular, excessive UV exposure has become a serious health concern for this nation as it poses non-melanoma and malignant melanoma skin cancer risks for the general public (Parisi et al. 2003).

The AI-powered UV radiation predictive frameworks constructed in this research can deliver more accurate forecasts of UV radiation in terms of UVI and UV-A with explainable outputs. The outcomes of this study with the newly developed decision-support tools can robustly aid UV radiation experts and health sector stakeholders to provide real-time sun-exposure information to the public and help mitigate skin and eye-related health risks. The prescribed tools can also support the decision-makers and the UV radiation researchers to explore the solar UV-exposure-related damaging effects on terrestrial plants and animals to further benefit the agricultural sector.

1.5. **Thesis layout**

The schematic structure presented in Figure 1 illustrates the overview of the thesis. It clearly highlights the significant linkages between the atmospheric variables with the ground-level UV radiation exposure and outlines the need for an accurate, reliable and trustworthy forecasting system by integrating AI-inspired technologies. This thesis is organized into 7 distinct chapters, given as follows:

Chapter 1 Delivers the introductory background, provides the statement of the problem to highlight the importance of this research and presents the objectives of this study.

Chapter 2 Presents the literature review to summarise the existing research and development of intelligent decision-support tools towards mitigating UV-exposure-related skin and eye diseases.

Chapter 3 Describes the research site, datasets and general methodology applied in this study. Detailed descriptions of specific study areas, data and methods are provided in chapters that present the respective journal articles.

Chapter 4 This chapter is presented as a published article in the *IEEE ACCESS* journal (DOI: 10.1109/ACCESS.2022.3153475). It addresses the first research objective of this study, as it is devoted towards the construction of a SWT-based multiple input multi-step output convLSTM model integrated with BorutaShap and Optuna algorithms to forecast short-term UVI at different forecast horizons. It utilizes cloud statistical properties extracted from the sky images and SZA as predictor inputs in developing the hybrid model.

Chapter 5 This chapter is presented as a published article in the *Expert Systems with Applications* journal (DOI: 10.1016/j.eswa.2023.121273). It describes the establishment of a hybridized ensemble N-BEATS model that forecasts short-term UV-A radiation for the seasons of autumn, winter, spring and summer to address the second research objective of this study. The ensemble model is developed with 15 single-point models trained on three different key loss functions. Model calibration is carried out through uncertainty quantification to further enhance model reliability and forecasting performance.

Chapter 6 This chapter is presented as a published article in the *Computer Methods and Programs in Biomedicine* journal (DOI: 10.1016/j.cmpb.2023.107737). The chapter is in response to the third objective of this study and it describes the design of a hybrid explainable DNN model that integrates dual-phase feature selection algorithms and a Bayesian optimizer to forecast short-term UVI. This early warning tool remarkably provides explanations of UVI predictions by integrating xAI-based model-agnostic tools that include LIME, SHAP and PFI algorithms.

Chapter 7 This chapter discusses the synthesis of the study and presents the concluding remarks, limitations and recommendations for future research.

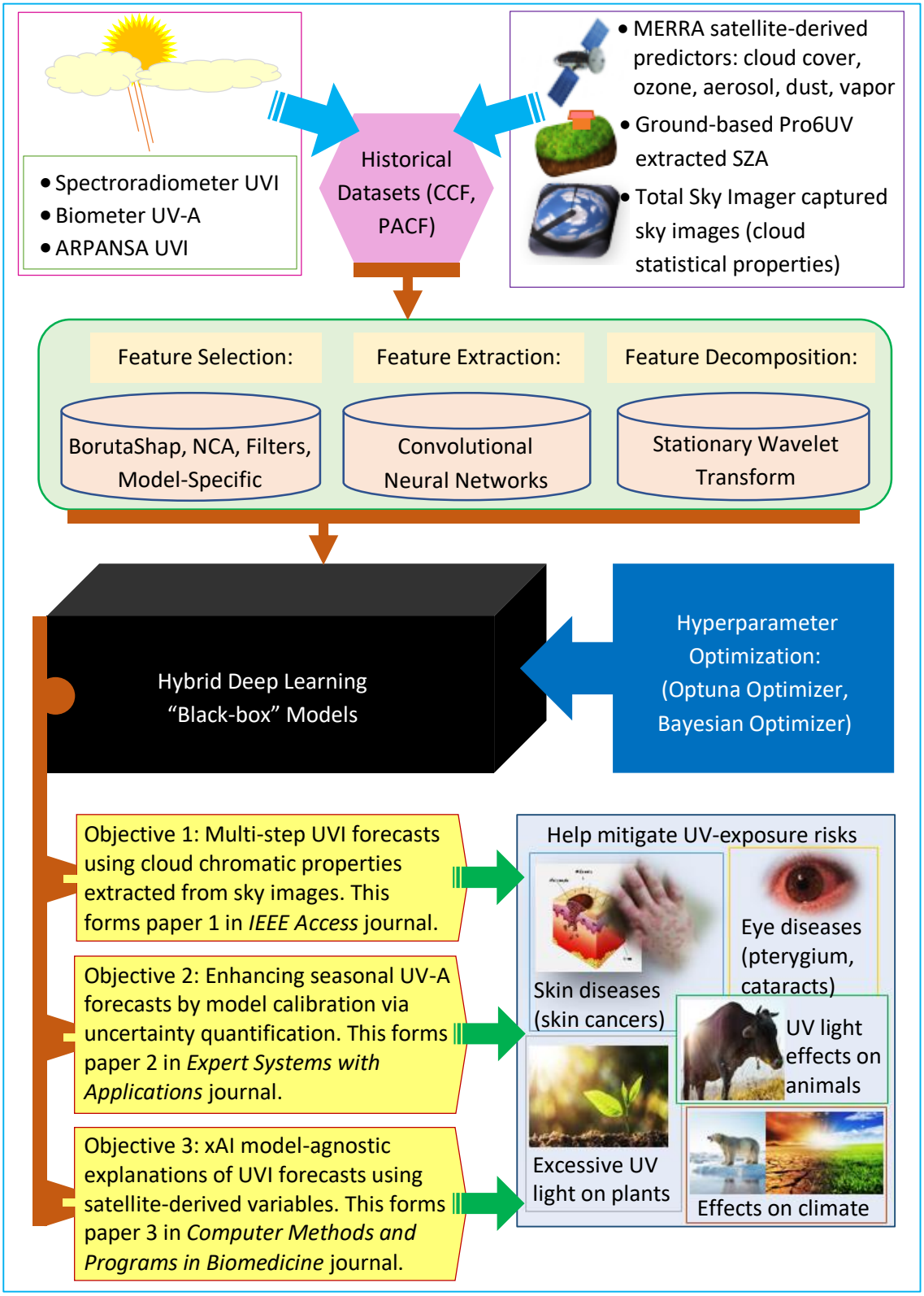

Figure 1 Schematic structure of the content of this PhD thesis.

CHAPTER 2: LITERATURE REVIEW

This chapter presents the literature and relevant backgrounds to the study and reviews the key issues related to the harmful impacts of exposure to solar UV radiation. Subsequently, a critical analysis of the challenges in previous and current approaches adopted in predicting ground-level UV radiation is provided. The chapter further outlines the knowledge gaps in the existing literature, consequently highlighting the essential modelling approaches of UV radiation that can be adopted for designing a robust decision support tool to help mitigate the adverse effects of UV exposure.

2.1. Implementing sun protection against the harmful exposure effects of solar UV radiation

Solar radiation is an important factor that helps sustain life on earth. Apart from its beneficial effects, prolonged exposure to the UV waveband is known to pose detrimental effects on human skin and eyes. In most cases, skin-based diseases through exposure to erythemally-effective UV radiation can become more severe and carcinogenic (Saraiya et al. 2004). Particularly, chronic exposure to UV radiation has become a substantial risk factor that can lead to melanoma and non-melanoma cancers (Sivamani et al. 2009). Apart from humans, the harmful UV rays also pose severe damaging effects on terrestrial animal and plant life (Paul & Gwynn-Jones 2003).

Australia is one of the countries that receives high doses of UV radiation during the year and the consequent impact of UV exposure on the people and the terrestrial life has become a growing concern. In particular, skin cancer cases that include malignant keratinocyte cancers have been burdening the Australian economy through its health sector (Dexter et al. 2020). To implement sun protection, it is essential that accurate real-time UV exposure advice is delivered to the general public, as well as the UV radiation researchers for any geographical location within the country, including remote areas. In this respect, the harmful UV-exposure effects can be best mitigated through the development and applications of robust decision-support tools that are capable of providing more accurate and flexible predictions of UV radiation depending on the existing conditions.

2.2. Mechanistic and deterministic-modelling methods in predicting UV radiation

For many decades, predictions of solar UV radiation have been achieved in terms of UVI, as well as UV-A and UV-B using traditional mechanistic methods that involved mounting and monitoring of spectroradiometers or radiometers in open space (Kudish et al. 2005; Deo et al. 2017). Similarly, estimations of the incident solar irradiance have been commonly obtained by deploying satellite-based instrumentations. The two approaches can offer accurate UV-exposure information but their practical utility is highly constrained by the high costs of installation, operation and maintenance (Koskela et al. 2006; Bernhard et al. 2020). Together with these flaws and accessibility-related issues for most remote locations, an alternative deterministic method has been utilized in predicting UV radiation.

The deterministic approach is also very effective, however, the overall predictive accuracy of this technique is affected by the limitations of model initialization with preconceived boundary conditions derived from existing or assumed parameters (Deo et al. 2017). In the Australian context, some recent researchers have mentioned the application of smartphones in the monitoring and prediction of UVI or UV-A radiation by utilizing image sensors as UV radiation detectors (Igoe et al. 2013; Turner et al. 2020). Though this approach is promising, the broad application of this technology entails considerable challenges associated with accessibility and costs. In addition, ARPANSA also provides information on UV radiation measured using a network of UV detectors for selected geographical locations, mostly for the major cities (Deo et al. 2017). However, other locations outside the range of the ARPANSA network are disadvantaged. Thus, a more robust and cost-effective UV radiation prediction system is needed that can be accessible for any given location, including remote areas.

2.3. Artificial intelligence-inspired predictive frameworks as modelling approaches towards UV radiation prediction

AI-based expert predictive systems have the capacity to robustly address the shortcomings of the mechanistic and deterministic approaches to forecast more accurate ground-level UV radiation. The AI-powered ML and DL algorithms are remarkable forecasting platforms that effectively handle any non-linearity in the input data series with high computational efficiencies (Ahmed et al. 2022). Some earlier

studies have explored the potential of ML methods in forecasting solar UVI. A feed-forward multi-layered supervised artificial neural network (ANN) was applied to generate accurate forecasts of medium and high UVI on a long-term basis (Latosińska et al. 2015). In another study, the artificial neural network (ANN) was found to exhibit strong predictive ability in delivering forecasts of solar UV erythemal irradiance for seven Spanish sites (Alados et al. 2007). The data-driven ANN model has also been integrated with the radiative-based models in approximating the radiative transfer codes for estimating UV-A and UV-B radiation (Takenaka et al. 2011). Moreover, a near-real-time UVI was forecasted for Toowoomba, Australia by integrating a skilful extreme learning machine (ELM) with SZA (Deo et al. 2017).

Other studies have preferred to utilize the DL technique over the ML methods in time-series forecasting. The DL frameworks are capable of implementing a non-linear model with an architecture having many hidden layers to efficiently learn the complex input-output relationships (Chauhan & Singh 2018). In comparison with DL technology, the ML approach also exhibits some overfitting constraints, which can affect the overall testing phase accuracies (Barboza et al. 2017). The DL technique can independently detect relevant features in high dimensional data, which is another strength of this framework over the conventional ML methods (Indolia et al. 2018). In the case of forecasting solar UV radiation, a DL long short-term memory (LSTM) network was implemented in forecasting three days ahead UVI with model input ranging from univariate to multivariate (Oliveira et al. 2020). However, other robust DL models, such as convLSTM and N-BEATS are not explored for UV radiation forecasting. While the multiple input multi-step output convLSTM model revealed remarkable performance in a study that entailed flood index forecasting (Moishin et al. 2021), the N-BEATS model demonstrated robust performance in a recent study for forecasting the solar radio flux (Stevenson et al. 2022).

Most of the hotspots at risk of UV exposure in Australia have not been explored for validating a DL UV radiation forecasting framework to provide real-time UV exposure information and appropriate sun-protection behaviour recommendations to the general public, as well as UV researchers. As most Australian regions are exposed to high UV radiation exposure, it is essential to establish a more accurate AI-inspired UV radiation forecasting framework as an early warning tool for this country.

2.4. **Performance enhancement approaches for the AI-based predictive systems**

To achieve enhanced performance by ML and DL predictive systems, several input pre-processing and modelling approaches can be adopted prior to model construction. Firstly, it is important to select the best time-lagged inputs at the most significant lag for modelling the target variable. In this respect, the cross-correlation functions (CCF) in terms of the cross-correlation coefficient (r_{cross}) have been assessed in several studies to obtain the best time-lagged predictor inputs at the most significant lag (Deo et al. 2017; Ghimire et al. 2019a). On the same notion, the partial autocorrelation function (PACF) has also been assessed and the most significant lagged inputs were selected for model building (Ghimire et al. 2019b).

The high-frequency input variables when normalized between 0 and 1 using the min-max normalization prevent the variables from having large ranges of numerical values (Moosavi & Bardsiri 2017). Through the data normalization process, each variable exhibits the same order of magnitude, thus increasing the training phase efficiency of the predictive models.

To further optimize the predictive performance of any ML and DL technologies in the respective forecasting domain, there are some eminent hybridized approaches that can be implemented during the model design phase. For instance, a powerful hybrid predictive framework can be developed with robust ML or DL algorithms by integrating a number of skilful modelling strategies that include feature selection, data decomposition, and hyperparameter optimization (Jayasinghe et al. 2021).

2.4.1. ***Wrapper and filter methods for feature selection***

Feature selection algorithms enable the selection of the most informative and pertinent features through the dimensionality reduction of large sets of feature variables. Through effective feature selection, the irrelevant and largely redundant features are successfully eliminated during the model design phase to optimize the predictive performance and reduce computational costs (Hu et al. 2015). In a wrapper-based feature selection method, the usefulness of a feature subset is measured through the actual training of the predictive model on this subset. Some recent researchers have applied wrapper algorithms and noted significant improvement in forecasting accuracies. Among the wrapper approach, BorutaShap is one elegant method that combines the Boruta feature selection algorithm with the shapely additive

explanations. In a recent study, the BorutaShap method was applied by integrating a tree-based learner as a base model to select the most pertinent attributes and to offer the individual feature contribution towards generating model predictions in forecasting the stock prices for normal time and during the period of COVID-19 pandemic (Ghosh & Chaudhuri 2022). The NCA algorithm is another intelligent wrapper method that can select the most informative attributes from high-dimensional data series. For instance, the NCA tool applied in generating accurate soil moisture forecasts with multivariate hydro-meteorological predictors efficiently captured the significant temporal dynamics of historical behaviour to select the meaningful attributes for model building (Prasad et al. 2018). However, the aforementioned BorutaShap and NCA algorithms have not been applied as feature selection tools in any UV radiation predictive system.

On the other hand, feature selection using filter-based strategies measures the relevance of the predictor variables through their respective correlation with the dependent variable. Such selective-filtering methods were applied in some recent studies during the model-building phase to generate efficient forecasts of pan evaporation (Jayasinghe et al. 2022) and solar radiation (Ghimire et al. 2022). While the filter methods are highly efficient, their applications have not been explored in forecasting solar UV radiation in a dynamic atmosphere.

2.4.2. ***Data decomposition***

Data decomposition is another effective approach to reducing the dimensionality of the input variables and extracting the predictive patterns to fine-tune the model generalizations towards achieving optimal performance. Through data decomposition, the input variables decomposed into the underlying patterns and temporal behaviour enables addressing of the non-stationarity, non-linearity and noise in the datasets so that the relevant patterns are well represented through the resulting components when fed into an intelligent predictive model (Al-Musaylh et al. 2020; Sharma et al. 2020). SWT is one powerful mathematical tool that can carry out efficient data decomposition for this purpose. It is a modified version of discrete wavelet transform (DWT), systematically designed to handle the signal decimation issues that constrained the DWT applications (Rajput et al. 2015). In a recent study, SWT was applied to decompose the historical photovoltaic (PV) power datasets into respective detailed and approximation components that were fed into a DL LSTM-DNN model for generating excellent forecasts of PV power output (Ospina et al. 2019). While the

SWT-integrated DL model demonstrated superior forecasting skills in this domain, its promising data decomposition capability can also be integrated with a DL UV radiation forecasting framework for the current research.

2.4.3. *Hyperparameter optimization*

Efficient hyperparameter tuning of an intelligent predictive system enables the model to deliver optimum performance in any forecasting domain. In most previous studies, the grid and random search techniques were implemented to tune several important model hyperparameters. For instance, a random search algorithm was employed to efficiently tune the hyperparameters of a DNN model to enhance its performance in power consumption forecasting (Torres et al. 2019). Similarly, a grid search algorithm was utilized to optimize the hyperparameters of a solar radiation forecasting model (Yagli et al. 2019). Although these algorithms are commonly utilized, the search strategy can be computationally expensive during the tuning process as each evaluation in its iterations is independent of prior iterations due to which, the unsatisfactory performing hyperparameters are unavoidably assessed (Putatunda & Rama 2019). Alternatively, other skilful algorithms like Optuna and Bayesian optimizer algorithms do not suffer these constraints and these methods exhibit superior performance in optimizing any ML and DL model hyperparameters.

The Optuna algorithm possesses powerful sampling and pruning efficiency in tuning model hyperparameters, which was evident in a study that utilized a LSTM model to forecast offshore wind power (Hanifi et al. 2022). In a similar manner, the powerful Bayesian optimizer was applied to achieve optimally tuned hyperparameters of support vector regression (SVR) and bidirectional long short-term memory (BiLSTM) models to forecast hybrid electricity price for the German energy exchange (Cheng et al. 2019). Considering the strong hyperparameter tuning competency of both the Optuna and Bayesian optimizers, their robustness can be explored in optimizing the hyperparameters of the UV radiation forecasting systems in this research.

2.5. **Calibration of artificial intelligence-based forecasting systems through uncertainty quantification**

Model calibration through uncertainty quantification is a meritorious technique for further improving the predictive performance, as well as enhancing the reliability of an intelligent forecasting framework (Lakshminarayanan et al. 2017). In this respect, uncertainty estimates of the forecasts can be generated through deep ensembles of single-point DL learning models trained on different key loss functions. A recent study constructed an ensemble of a DL model that was trained on different loss functions to reduce the potential sources of uncertainty and training biases (Stevenson et al. 2022). In this research, the ensemble DL model was calibrated and it offered integrated uncertainty quantification to confirm the reliability of the solar radio flux forecasting model. A similar approach can be applied to a UV radiation forecasting framework to improve the model performance and reliability for the current research.

2.6. **Model-Agnostic Explanations with xAI Tools**

DL learning models are known to have a “black-box” architecture where the complex internal decisions towards generating an outcome are hidden and unexplained to the end-users. In this respect, the state-of-art xAI tools provide avenues to extract more transparent, trustworthy and understandable explanations for the model decisions and actions in generating predictions (Vilone & Longo 2021). The model-agnostic xAI tools can offer both local and global explanations that are instrumental to understanding how the different predictor variables influence the predictions made by a “black-box” model (Ryo et al. 2021). Recently, the LIME model-agnostic tool was applied to obtain the local interpretability for different configurations of the LSTM networks to gain more insight into forecasting the heat demand for the operation of the district heating systems (Zdravković et al. 2022). A similar research integrated xAI-powered model-agnostic SHAP and PFI explainers with a RF model to offer global interpretations based on interactions of the input attributes in predicting solar radiation (Chaibi et al. 2021). SHAP explainers exhibit powerful performance in providing global post-hoc interpretations based on the input perturbations and this was evident through a comprehensive survey using a DNN model (Saleem et al. 2022).

Both the local and global explainers have their own strengths and limitations. For instance, the LIME method is much faster than the SHAP tool in executing the

instance-based interpretations on the contribution of individual predictor variables towards the model predictions (Islam et al. 2022). In comparison with LIME, the SHAP technique efficiently provides intuitive explanations for the entire decision of the "black-box" model at a global level (Joseph et al. 2022). As a result, most researchers have opted to implement both the local (LIME) and global (SHAP and PFI) explainers to extract more rigorous and faithful "black-box" model interpretations for making better decisions (Alabi et al. 2022; Zheng et al. 2022). So far, none of these xAI tools has been integrated with any DL UV radiation forecasting domain. This opens the room to further explore the xAI methods in this research to explain how the satellite-derived and ground-based predictor variables impact the UV radiation forecasts generated by the DL-based "black-box" models.

2.7. **Summary highlighting the gap in the literature**

The literature review outlined the key findings and research gaps in designing a highly robust and accessible UV radiation forecasting framework. So far, the aforementioned DL models have not been integrated with sky image-derived cloud statistical properties (that depict the cloud cover effects) as input predictor variables to forecast the ground-level UV radiation for most Australian hotspots receiving high UV exposure. Additionally, the UV radiation forecasting models have not been calibrated through integrating uncertainty quantification for deep ensemble-based models to enhance performance and model reliability. The literature also presented remarkable feature selection techniques (such as BorutaShap and NCA), hyperparameter optimization tools (such as Optuna and Bayesian optimizers) and data decomposition using SWT. These methods have not been employed in any UV radiation forecasting framework to further optimize the model performance. In addition, the powerful xAI tools have not been integrated with the DL UV radiation forecasting models to offer model-agnostic explanations using the satellite-derived and ground-based predictor variables. In this regard, the local and global model-agnostic explanations can enable the end-users to make better decisions and confirm the trustworthiness of the UV forecasting model. Thus, the current PhD research addresses and fills the aforementioned gap in the literature to design a more accurate, reliable and explainable UV radiation forecasting framework that can serve as a

decision support tool to help mitigate UV exposure-related deleterious effects on people and terrestrial life.

CHAPTER 3: DATA, STUDY AREA AND METHODOLOGY

This chapter presents an overview of the geographical location of the study sites in developing and validating the hybrid DL intelligent UV radiation forecasting models. A number of different study sites were selected for experimenting the different objectives outlined for this research and their detailed descriptions are provided in the upcoming chapters. Where needed, the proposed forecasting models were also validated for different seasons. The chapter describes the datasets along with the length of data and it further accounts for limitations, if any. Additionally, a brief introduction of the methodology is provided, while the details of specific model development methods are given in the respective forthcoming chapters.

3.1. Study area

To establish and validate the merits of the prescribed DL hybrid models in forecasting solar UV radiation, the major focus area for this study was the Australian hotspots that receive high ground-level UV radiation exposure. Specifically, these hotspots include Toowoomba (UniSQ-based experimental site), Townsville and Emerald from the state of Queensland (QLD), while the Darwin and Alice Springs hotspots were selected from the Northern Territory (NT). The selected hotspots are known to be tropical and subtropical regions and these areas record a large number of sunshine hours annually (Deo et al. 2017). Within these sites, the harmful UV-exposure-related effects on the skin and eyes pose a significant burden on the health sector (Dexter et al. 2020), and concurrently, elevated UV radiation exposure further impacts terrestrial animal and plant life. The geographical locations of these hotspots are illustrated in Figure 2.

3.2. Data description

A range of data from different sources was selected as inputs in constructing the high-precision DL hybrid models for the different research objectives. Table 1 succinctly describes the datasets utilized in achieving each objective, along with the data source, study period (indicating the length of data) and the forecast horizons.

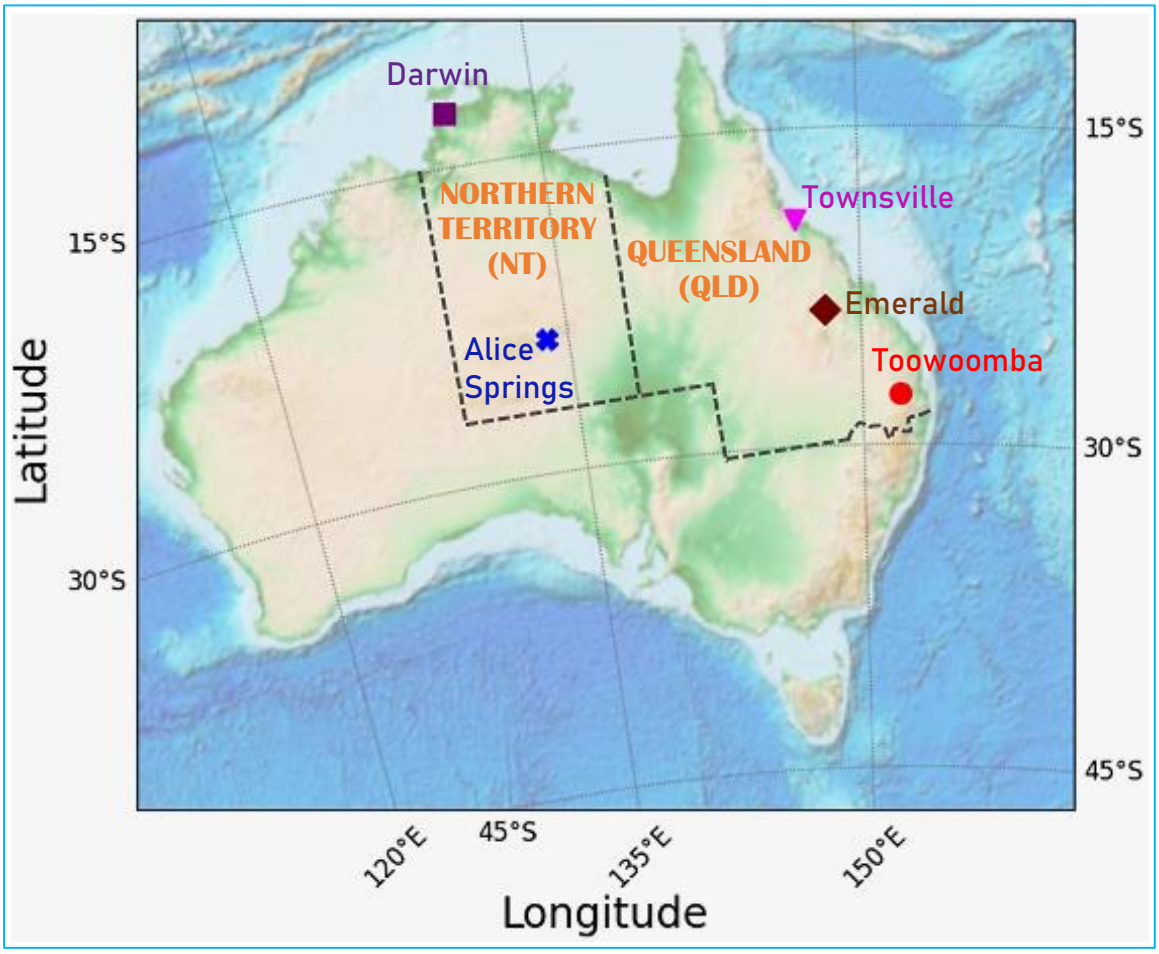

Figure 2 Map of Australia showing the selected hotspots within the study region of Queensland (QLD) and the Northern Territory (NT).

3.2.1. ***Ground-based experimental datasets***

The ground-based datasets were extracted at a 10-minute time resolution from the major experimental site located at the UniSQ campus in Toowoomba, Queensland, as indicated in Figure 2. At this site, the main source of the UVI dataset was the roof-top mounted Bentham DTM300 Spectroradiometer (Bentham Instruments Inc., UK), as shown in Figure 3 (a). Figure 3 (b) illustrates a co-located 501 broadband UVR Biometer (Solar Light Co., USA) that was used to acquire the UV-A (mW m^{-2}) datasets. Moreover, Figure 3 (c) shows a synchronous Total Sky Imager, TSI440 set-up (Yankee Environmental Systems Inc., USA) that was mounted at the same location to capture the sky images. These sky images were stored in the Total Sky Imager repository. Along with the Total Sky Imager, an integrated Pro6UV model (Deo et al. 2017) was applied simultaneously to record SZA (°). The study designed a robust image processing algorithm to segment the cloud statistical properties datasets from

the time series sky images. The detailed descriptions of these cloud statistical properties are presented in Table 2.

Table 1 Description of datasets used in this research.

Objectives	Data Used	Source	Study Period	Forecast Horizon
1 (*Chapter 4*)	Target: UVI Predictors: Sky image-derived cloud statistical properties, SZA	Spectroradiometer for UVI, Total Sky Imager for sky images and Pro6UV for SZA	March 2003 to February 2004	Multistep: 10-minute, 20-minute, 30-minute, Hourly
2 (*Chapter 5*)	Target: UV-A Predictors: Cloud chromatic properties from sky images, SZA	Biometer for UV-A, Total Sky Imager for sky images and Pro6UV for SZA	September 2002 to August 2003	20-minute ahead UV-A (seasonal-based forecast for spring, summer, autumn, winter)
3 (*Chapter 6*)	Target: UVI Predictors: Atmospheric variables, SZA	ARPANSA for UVI, MERRA satellite for atmospheric variables and Pro6UV for SZA	January 2020 to December 2021	Hourly forecast of UVI with model-agnostic explanations

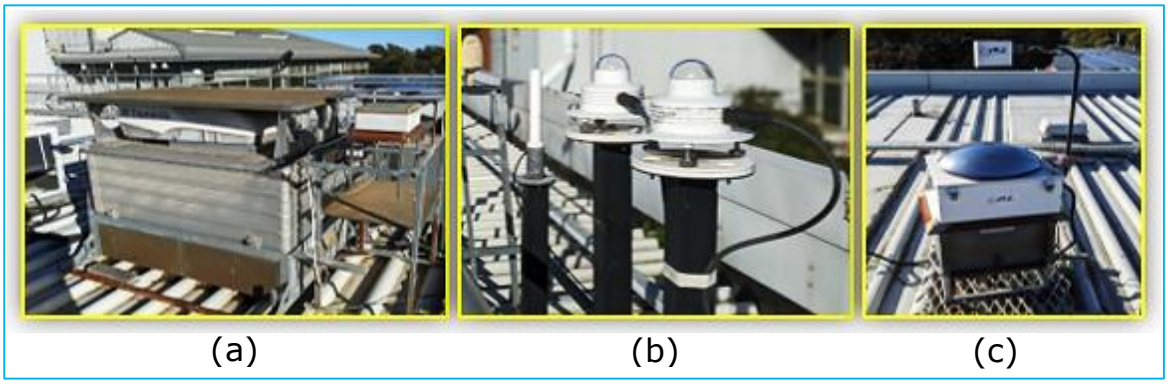

Figure 3 Roof-top mounted experimental set-up at UniSQ campus in Toowoomba to acquire ground-based modelling datasets. (a) Bentham DTM300 Spectroradiometer, (b) 501 broadband UVR Biometer, (c) Total Sky Imager, TSI440.

Table 2 Description of cloud statistical properties datasets segmented from the sky images. It is to be noted that the cloud statistical properties are unitless variables.

Cloud Statistical Properties	Acronyms	Description
Red channel-based cloud average	*Cra*	Red channel mean pixel value that represents cloud cover
Red and blue channel-based sky ratio	*SRBr*	Red & blue channel mean pixel value ratio that represents blue sky
Blue channel-based cloud average	*Cba*	Blue channel mean pixel value that represents cloud cover
Opaque cloud	*OC*	Proportion of thick cloud cover in the sky
Cloud fraction	*CF*	Fraction of number of cloud pixels out of the total number of unmasked pixels
Red & blue channel-based cloud ratio	*CRBr*	Red & blue channel mean pixel value ratio that represents cloud cover
Red & blue channel-based normalized cloud ratio	*CNRBr*	Red & blue channel normalized pixel value ratio that represents cloud cover
Red & blue channel-based cloud difference	*CRBd*	Red & blue channel mean pixel value difference that represents cloud cover
Thin Cloud	*TC*	Proportion of thin cloud cover in sky
Red channel-based cloud standard deviation	*CRs*	Red channel pixel value standard deviation that represents cloud cover
Red channel-based sky average	*Sra*	Red channel mean pixel value that represents blue sky
Blue channel-based cloud standard deviation	*CBs*	Blue channel pixel value standard deviation that represents cloud cover
Red channel-based sky standard deviation	*SRs*	Red channel pixel value standard deviation that represents blue sky
Blue channel-based sky standard deviation	*SBs*	Blue channel pixel value standard deviation that represents blue sky
Blue channel-based sky average	*Sba*	Blue channel mean pixel value that represents blue sky
Red & blue channel-based sky difference	*SRBd*	Red & blue channel mean pixel value difference that represents blue sky
Red & blue channel-based normalized sky ratio	*SNRBr*	Red & blue channel normalized pixel value ratio that represents blue sky

3.2.2. ***Satellite-derived atmospheric datasets***

The satellite-derived datasets have been sourced from the National Aeronautics and Space Administration (NASA) database, particularly the Goddard Online Interactive Visualization and Analysis Infrastructure (GIOVANNI) geoscience

data repository from https://giovanni.gsfc.nasa.gov/giovanni/. GIOVANNI acquires data for over 2000 satellite variables, for which it eminently provides online-based visualizations and analytical platforms (Chen et al. 2010). As per the GIOVANNI repository, these datasets were extracted using the Modern-Era Retrospective Analysis for Research and Applications (MERRA) satellite at hourly time resolution. These datasets were extracted at a spatial resolution of 0.5° × 0.625° and are detailed in Table 3.

Table 3. Description of the Modern-Era Retrospective Analysis for Research and Applications (MERRA) satellite-derived predictor variables.

Attribute Description	Acronyms	Units	Instrument
Cloud area fraction for high clouds	CAFHC	-	M2T1NXRAD v5.12.4
Cloud area fraction for mid clouds	CAFMC	-	M2T1NXRAD v5.12.4
Cloud area fraction for low clouds	CAFLC	-	M2T1NXRAD v5.12.4
Total aerosol angstrom parameter	TAAP	-	M2T1NXAER v5.12.4
Total aerosol scattering AOT	TAS		M2T1NXAER v5.12.4
Dust scattering AOT	DS		M2T1NXADG v5.12.4
Total column ozone	TCO	Dobsons	M2T1NXSLV v5.12.4
Total precipitable water vapor	TPWV	kg m^{-2}	M2T1NXSLV v5.12.4

3.2.3. *Australian Radiation Protection and Nuclear Safety Agency (ARPANSA) datasets*

ARPANSA is known to be the primary authority on radiation protection that administers and maintains an ultraviolet radiation monitoring network for the Australian Government. At ARPANSA, accurate procedure and cost-effectiveness are ensured through monitoring regular data assessment and quality checks. For the purpose of this research, ARPANSA provided the ground data for the target variable UVI at hourly time resolution. These datasets were accessed from https://www.arpansa.gov.au for the four Australian hotspots that include Townsville, Emerald, Darwin and Alice Springs.

3.3. **Objective-specific sites and data allocation**

Objective 1 focused on the development of a UVI forecasting model for the UniSQ-based Toowoomba experimental site, as indicated in Table 1. In this regard, the target variable was UVI and the respective datasets were mainly extracted with a Spectroradiometer. As illustrated in Table 2, the selected predictor variables for this objective were the cloud statistical properties that depicted the cloud cover effects on the ground-level UVI. The cloud statistical properties extracted from the sky images were captured using a Total Sky Imager. SZA was another predictor input for model building, obtained using the Pro6UV model.

Objective 2 developed a UV-A forecasting model at a 20-minute horizon for the Toowoomba study site, as highlighted in Table 1. For model building, the target variable was UV-A and the datasets for this variable were extracted using a Biometer. The predictor inputs were cloud statistical properties extracted from the sky images and SZA measured with Pro6UV. Like objective 1, this objective also utilized the sky images as inputs for model building. The sky images were only available for the Toowoomba experimental site and for this reason, the study sites were the same for both objectives. However, the target variables for these objectives were different with different UV-A measurement equipment for objective 2. The selected length of datasets was also different for the two objectives. As mentioned before, objective 2 entails calibration of the UV-A forecasting model via uncertainty quantification while objective 1 designs a multiple-input multi-step output model for UVI forecasting.

For objective 3, an xAI-inspired explainable UVI forecasting model was constructed for the Darwin, Alice Springs, Townsville and Emerald sites, as shown in Table 1. In this respect, the target variable was UVI, for which, the datasets were obtained from the ARPANSA networks. The predictor variables for this objective were the MERRA satellite-derived atmospheric variables and the Pro6UV model-based SZA for the four hotspots. As illustrated in Table 3, the selected atmospheric variables are highly interconnected with the solar UVI, which included cloud cover conditions, atmospheric aerosol column, ozone effects, dust concentrations and water vapour content.

3.3.1. *Some minor limitations regarding data availability*

In objective 1, the input data of UVI, cloud statistical properties and SZA were extracted at a 10-minute time resolution for model building. In this regard, the aerosol and ozone datasets could not be used because these were not available for the Toowoomba experimental site at a 10-minute time resolution. However, to account for the aerosol and ozone effects in the model training, the time-lagged Bentham UVI datasets that already captured some ozone and aerosol effects were utilized. Additionally, the geographical location of the experimental site is nearly 100 km inland relative to the ocean, due to which this region experiences limited aerosol and anthropogenic effects (Deo et al. 2017).

The aforementioned limitation for objective 1 equally applies to objective 2, which entails the design of the UV-A forecasting model. Consequently, this objective also utilized the time-lagged Biometer UV-A datasets that captured some ozone and aerosol effects in the historical memory of UV-A.

In objective 3, the sky images were not available for the Darwin, Alice Springs, Townsville and Emerald hotspots, so the cloud statistical properties could not be utilized in designing the UVI forecasting models for these sites. Nevertheless, these attributes were well represented by the satellite-derived cloud cover conditions, along with atmospheric aerosol column, ozone effects, dust concentrations and water vapour content extracted at hourly time resolution.

3.4. **General methodology**

A number of pre-processing tasks were applied to the input variables prior to model construction. For all the objectives, the most significant lagged outputs were extracted for the predictor variables by assessing the CCF in terms of their r_{cross} with the target variable. Similarly, the most significant lags for the target variable were also extracted by assessing the PACF. In the case of generating multi-step forecasts, the datasets for the predictor variables and the target were further converted to their required forecast horizons.

All three objectives entailed the feature selection phase as an essential component for the practical application of the proposed forecasting models. Effective feature selection reduces the dimensionality of the input attributes, minimizes the computational cost in training the predictive model and improves the forecasting accuracies (Bolón-Canedo et al. 2015; Pirbazari et al. 2019). Various feature selection

algorithms were incorporated for the different objectives, which included the BorutaShap algorithm in objective 1 and the NCA algorithm in objective 2. For objective 3, a dual-phase feature selection was applied, which included a model-specific feature selection with random forest (RF), followed by a filter-based approach to identify and eliminate the redundant features by exploring the correlations.

Data decomposition is another vital phase that can effectively handle the non-stationarity issues associated with the input datasets. For objective 1, SWT was applied as a data decomposition tool. Data decomposition using SWT reduces the dimensionality of the inputs and takes care of the non-stationarity and noise in the datasets to achieve more efficient forecasting capabilities by the predictive models (Zhang et al. 2013; Ospina et al. 2019). For objectives 2 and 3, the augmented Dickey-Fuller Test (e Silva et al. 2020) was applied to test the stationarity in the input datasets.

The model inputs were normalized between [0 – 1] using the min-max normalization to avoid the variables having large ranges of numerical values to achieve more efficient and effective model training. For each objective, a detailed description of the data normalization is provided in respective chapters. In general, the min-max data normalization approach (Moosavi & Bardsiri 2017) is defined as follows:

$$X_{Norm} = \frac{X_{Act} - X_{Min}}{X_{Max} - X_{Min}} \quad (1)$$

where X_{Norm} is the normalized value, X_{Act} is the actual input variable, X_{Max} is the maximum value and X_{Min} is the minimum value.

Applications of remarkable hyperparameter optimization algorithms further improve the predictive accuracy of AI-inspired forecasting models (Ghimire et al. 2022). For this purpose, a powerful Optuna algorithm was applied to optimally tune the hyperparameters of the UVI forecasting models in objective 1. Similarly, a robust Bayesian optimizer was applied for optimizing the model hyperparameters in objectives 2 and 3. These algorithms and the optimized hyperparameters are discussed in detail for each objective in the respective chapters.

This PhD research considers the development of various AI-inspired ML and DL predicting models and evaluating their ability to forecast ground-level solar UV radiation. In objective 1, a multistep UVI forecasting model was designed using a convLSTM model. Fundamentally, a convLSTM model is an extension of LSTM

networks and its architecture encapsulates the convolutional operation to efficiently capture the underlying spatial features in large-scale sequential and multi-dimensional datasets (Xingjian et al. 2015; Lee & Kim 2020). Other ML models, such as support vector regression (SVR) and passive-aggressive (PA) and DL models, such as convolutional neural network (CNN) were used in constructing the benchmarked models. The SVR model is constructed on a statistical learning theory-based ML framework that has been applied previously to solve high-dimensional regression problems (Salcedo-Sanz et al. 2014). The PA model is another competent ML algorithm that is mostly applied for large-scale learning with sequential incoming datasets (Zhai & Wang 2022). Additionally, the DL-based CNN model can robustly extract intrinsic features of the time series input variable to further improve the predictive capability (Morid et al. 2020).

Objective 2 further advances the first objective by designing an interpretable UV-A forecasting model with ensemble architecture to carry out uncertainty quantification and calibrate the DL N-BEATS model for achieving enhanced predictive performance and model reliability. The N-BEATS can generate interpretable outputs by enforcing the model to learn the seasonality and trend components of the input datasets (Oreshkin et al. 2019). Apart from N-BEATS, the LSTM and Bayesian ridge regression (BRR) models were also explored as powerful competing models in forecasting UV-A. The BRR model utilizes probability distributors to formulate linear regressions so that the poorly distributed datasets are handled efficiently (Shi et al. 2016). On the other hand, the DL LSTM is a type of recurrent neural network that exhibits an excellent ability to learn long-term dependencies in sequence-based prediction problems (Cui et al. 2020).

In objective 3, a DNN model was integrated with the xAI tools (such as LIME, SHAP and PFI) to offer local and global model-agnostic explanations based on the influence of the input features in generating the predictions of UVI. The design architecture of a DNN model contains networks of multiple hidden layers and nodes that can automatically and robustly extract relevant feature information from the input datasets (Keleko et al. 2023). Other competing benchmarked models applied in assessing the predictive performance included fully convolutional network (FCN), ANN, multilayer perceptrons (MLP), AdaBoost (AB), stochastic gradient descent (SGD) and decision tree (DT). In generating predictions using a DL FCN model, the task of fully connected layers can robustly be performed using 1×1 convolutions

(Phithakkitnukooon et al. 2021). The ANN model is another competent model having input, hidden (fully connected) and output layers that mimic the human brain to generate highly precise predictions (Okut et al. 2013). In an AB model, the principle of ensemble learning technique is adopted where the combined version of some poor-performing individual models forms a powerful ensemble model for generating highly accurate predictions (Xiao et al. 2018). Additionally, the SGD model is an iterative algorithm that can robustly make small adjustments to the model network to minimize its error and increase the predictive capability with reduced computations (Chen et al. 2021). On the other hand, the DT algorithm is a tree-based predictive model that is known for its intelligibility and simplicity in generating accurate predictions (Ghiasi et al. 2020).

For the purpose of this PhD research, hybridized versions of the aforementioned ML and DL models were constructed to forecast solar UV radiation in each objective. The specific hybrid models developed to achieve each objective are as follows:

1. A three-phase wavelet hybrid model, designated as W-O-convLSTM was constructed to forecast UVI at multi-step horizons (i.e., 10-minute, 20-minute, 30-minute and 1 hour). The hybridized version of the convLSTM model was constructed by integrating SWT, BorutaShap and Optuna algorithms. The non-wavelet benchmarked models were constructed using convLSTM, CNN, SVR and PA algorithms, which were designated as O-convLSTM, O-CNN, O-SVR, and O-PA, respectively. Additionally, a baseline model trained only on SZA was developed and was designated as W-O-convLSTM$_{sza}$ (Chapter 4).
2. A hybrid ensemble model, designated as B-E-NBEATS was designed to forecast 20-minute ahead UV-A radiation. The hybridized version of the interpretable N-BEATS model was achieved by applying the NCA and Bayesian optimizer algorithms, together with an ensemble of 15 single-point N-BEATS models being trained on three key loss functions. The benchmarked models include a hybridized ensemble LSTM model designated as B-E-LSTM and the non-ensemble N-BEATS, LSTM and BRR models designated as B-NBEATS, B-LSTM and B-BRR, respectively (Chapter 5).
3. An enhanced joint hybrid explainable model, designated as EJH-X-DNN was developed to forecast hourly ahead UVI. The hybridized version of the DNN model was obtained by integrating the model-specific and filter-based dual-

phase feature selection, Bayesian optimizer and the model-agnostic xAI tools (such as LIME, SHAP and PFI). Several hybridized benchmarked models were constructed using FCN, ANN, MLP, AB, SGD and DT algorithms, which were designated as EJH-FCN, EJH-ANN, EJH-MLP, EJH-AB, EJH-SGD and EJH-DT (Chapter 6).

To evaluate the performance of the newly developed data-intelligent models, a diverse range of robust statistical score metrics were applied. The set of these evaluation metrics includes Pearson's correlation coefficient (r), mean squared error (MSE), root mean square error (RMSE), mean absolute error (MAE), Willmott's index (WI), Nash–Sutcliffe efficiency (NSE) and the Legates-McCabe's index (LM). Additionally, the relative (%) error values based on the RMSE and MAE, known as relative root mean square error (RRMSE) and relative mean absolute error (RMAE), were employed for seasonal-based comparisons of the model performance. For further veracity of the newly developed models, the Diebold-Mariano (DM) tests skill score (SS) were also utilized. Apart from these performance metrics, the proposed predictive models were further analysed using visual infographics that included line graphs, radar plots, scatter plots, box plots, histograms, Taylor plots, time-series plots, occurrence maps and reliability diagrams. The model-agnostic explanations of the DL model predictions were presented as plots generated by LIME, SHAP and PFI algorithms.

CHAPTER 4: PAPER 1 – CLOUD AFFECTED SOLAR UV PREDICTION WITH THREE-PHASE WAVELET HYBRID CONVOLUTIONAL LONG SHORT-TERM MEMORY NETWORK MULTI-STEP FORECAST SYSTEM

4.1. Introduction

This chapter is an exact copy of the published article in *IEEE ACCESS* journal, Vol. 10, Pages 24704 – 24720 (2022) (Scopus Impact Factor 3.9).

The chapter describes the design of a hybrid multi-step UVI forecasting framework using the convLSTM model for the Toowoomba experimental site. It explores the influence of the stochastic cloud cover effects on ground-level UVI by integrating the proposed predictive framework with cloud statistical properties extracted from sky images. Together with these predictors, SZA is also applied as an input variable. The cloud statistical properties have been extracted by designing robust image segmentation algorithms.

The essential phases in constructing the wavelet hybrid convLSTM model are described in a schematic diagram presented in Figure 4. Firstly, the most significant time-lagged predictor inputs were selected by assessing the cross-correlations with UVI. Thereafter, the convLSTM model was hybridized by integrating a SWT algorithm for data decomposition, BorutaShap for feature selection and Optuna optimizer for hyperparameter tuning. For all the forecasting time scales (i.e., 10-minute, 20-minute, 30-minute and 1-hour horizons), the proposed hybrid model designated as W-O-convLSTM was rigorously evaluated against four other benchmarked models (O-convLSTM, O-CNN, O-SVR, and O-PA) and one baseline model (W-O-convLSTM$_{sza}$) trained only on SZA predictor.

The overall performance assessment outcome revealed a superior forecasting performance by the wavelet-based W-O-convLSTM model. Consequently, the application of the proposed objective model had a significant advantage as it outperformed the non-wavelet-based benchmarked models in forecasting short-term UVI for all four seasons. The prescribed data-intelligent model also captured better forecasting performance over the baseline model trained on a single predictor variable of SZA, thus confirming the significance of the intermittent cloud effects on ground-level UV radiation. It was also observed that more accurate and efficient forecasts of

solar UVI were captured at decreasing forecast horizons. The robustness of this newly proposed UVI forecasting system avers its practical utility in delivering more accurate sun-protection behaviour information to the general public to help mitigate UV-exposure-related public health risks.

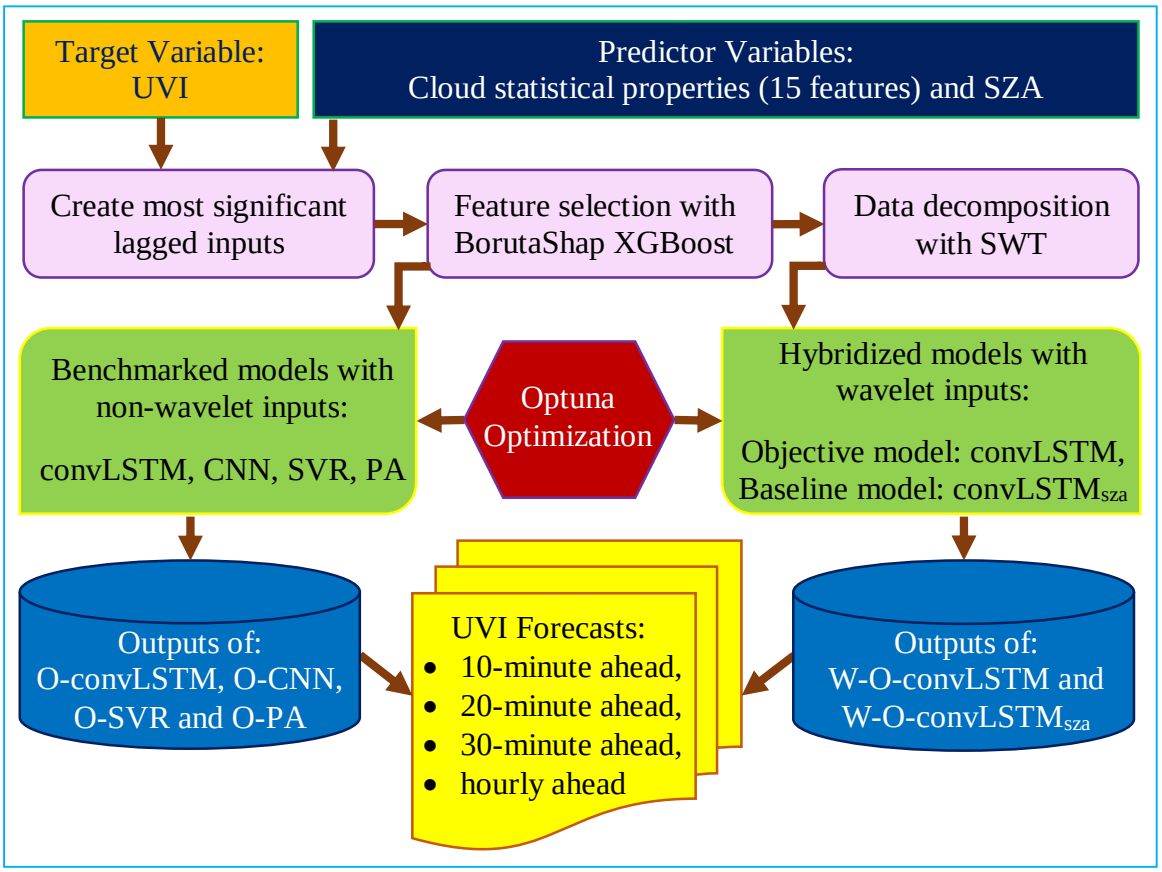

Figure 4 Schematic diagram of the proposed multi-step UVI forecasting system with cloud cover images using wavelet hybrid convLSTM model (W-O-convLSTM).

4.2. **Published paper**

IEEE Access
Multidisciplinary | Rapid Review | Open Access Journal

Received February 7, 2022, accepted February 19, 2022, date of publication February 22, 2022, date of current version March 9, 2022.

Digital Object Identifier 10.1109/ACCESS.2022.3153475

Cloud Affected Solar UV Prediction With Three-Phase Wavelet Hybrid Convolutional Long Short-Term Memory Network Multi-Step Forecast System

SALVIN S. PRASAD[1], RAVINESH C. DEO[1], (Senior Member, IEEE), NATHAN DOWNS[1], DAMIEN IGOE[2], ALFIO V. PARISI[2], AND JEFFREY SOAR[3]

[1]School of Mathematics, Physics, and Computing, University of Southern Queensland, Springfield, QLD 4300, Australia
[2]School of Mathematics, Physics, and Computing, University of Southern Queensland, Toowoomba, QLD 4350, Australia
[3]School of Business, University of Southern Queensland, Springfield, QLD 4300, Australia

Corresponding authors: Salvin S. Prasad (psdshalvin@gmail.com) and Ravinesh C. Deo (Ravinesh.Deo@usq.edu.au)

The work of Salvin S. Prasad was supported through the USQ Postgraduate Research Scholarship Awarded by the Graduate Research School (GRS), University of Southern Queensland (USQ), under Grant number 2020.

ABSTRACT Harmful exposure to erythemally-effective ultraviolet radiation (UVR) poses high health risks such as malignant keratinocyte cancers and eye-related diseases. Delivering short-term forecasts of the solar ultraviolet index (UVI) is an effective way to advise UVR exposure information to the public at risk. This research reports on a novel framework built to forecast UVI, integrating antecedent lagged memory of cloud statistical properties and the solar zenith angle (SZA). To produce the forecasts at multi-step horizon we design a 3-phase hybrid convolutional long short-term memory network (W-O-convLSTM) model, validated with Queensland-based datasets in near real-time (*i.e.*, 10-minute, 20-minute, 30-minute and 1 hour forecast horizon). Our approach in optimizing the performance also entails a robust selective filtering method using the BorutaShap algorithm, data decomposition with stationary wavelet transformation and hyperparameter optimization using the Optuna algorithm. We assess the performance of the proposed W-O-convLSTM model alongside the baseline and benchmark models. The captured results, through statistical metrics and visual infographics, elucidate the superior performance of the objective model in short-term UVI forecasting. For instance, at a 10-minute forecast horizon, our objective model yields a relatively high correlation coefficient of ∼0.961 in the autumn, 0.909 in the summer, 0.926 in the spring and 0.936 in the winter season. Overall, the proposed O-convLSTM model outperforms its competing counterpart models for all forecast horizons with the lowest absolute forecast error. The robustness of our newly proposed model avers its practical utility in delivering sun-protection behavior recommendations that can mitigate UV-exposure-related public health risk. We also recommend that future integration of aerosol and ozone effects with cloud cover data can enhance our forecasting framework for wider applications in solar energy or skin health monitoring systems.

INDEX TERMS Ultraviolet index forecasting, cloud effects, convolutional long short-term memory network, stationary wavelet transform.

I. INTRODUCTION

Solar ultraviolet radiation (UVR) has benefits and risks for the people, industry, and the natural terrestrial environment. Exposure to erythemally-effective UVR poses high health risks of skin-based diseases, such as malignant keratinocyte cancers, and eye diseases (pterygium and cataracts) in humans [1], [2]. In the agricultural sector, UVR reduces a plant's photosynthetic rate, CO_2 intake and oxygen outputs, thus hindering its water use efficiency [3]. However, solar radiation is a vital renewable energy resource in the energy sector for harnessing clean energy using solar photovoltaic (PV) technologies. Factors that affect terrestrial UV radiation are inclusive of time of the day, season,

The associate editor coordinating the review of this manuscript and approving it for publication was R. K. Tripathy.

geographical latitude, surface reflection, altitude and cloud cover [4]. While the intensity of solar UVR is largely dependent on solar zenith angle (SZA), the ground-level UVR is significantly affected by cloud movement. To implement sun-protection from such incident UVR, the World Health Organization (WHO), International Commission on Non-Ionizing Radiation Protection (ICNIRP), World Meteorological Organization (WMO) and United Nations Environment Programme (UNEP) developed the global solar ultraviolet index (UVI) for mitigating skin and eye health risks [5]. It is known that under unbroken cloud cover conditions, UVI reduces by 50 to 60%, and even further during precipitation [6]. However, under particular partial cloud cover conditions, scattering can escalate ground-based UV levels above the nominal cloud-free surface UV irradiation [7]. Thus, accurate forecasts of cloud-affected UVI are essential in delivering real-time sun-exposure advice to the public at risk of skin and eye-related diseases.

Malignant melanoma cases, which are more prevalent in fair skin types, increase with decreasing latitudes [8]. In Australia, 1726 and 714 deaths were reported in 2019 for cutaneous malignant melanoma and keratinocyte cancer (squamous cell carcinoma and basal cell carcinoma), respectively [9]. A survey in 2011-2014 revealed that among the Australian populations, Queensland recorded the highest person-based incidence of keratinocyte cancer excisions with 2679 per 100, 000 [10].

In this paper, we propose a deep learning (DL)-based novel wavelet hybrid convLSTM, to advance an earlier study [7], to forecast short-term UVI with cloud cover effects by integrating cloud segmented statistical properties extracted from whole sky images and SZA. The earlier study [7] neither considered cloud cover factor nor incorporated deep learning methods and multiple forecast horizons for solar UVI predictions. Considering the seasonal and diurnal variations of SZA, and the cloud movement, in this study, we also present forecasts of the four seasons tailored for multiple-step time horizons. Prior to modeling UVI, we utilize an intelligent BorutaShap algorithm to select the most informative input features from the cloud chromatic properties. In addressing the issues of non-stationarity, intermittent or stochastic variations, periodicity, and trends in the predictor variables, we apply a stationary wavelet transform (SWT) to decompose these input signals. To optimize the hyperparameters of the wavelet hybrid convLSTM, we employ a state-of-the-art Optuna (O) algorithm with powerful sampling and pruning efficiency. Hereafter, we designate the proposed 3 phase wavelet hybrid convLSTM model with O optimization as W-O-convLSTM. Thus, the contributions of this paper, which are distinct from an earlier study [7], are summarized as follows:

1) A novel hybrid W-O-convLSTM is proposed to forecast UVI for the first time using antecedent fluctuations in cloud cover condition and SZA at multi-step forecast horizon (*i.e.*, 10-minute, 20-minute, 30-minute & 1 hour).
2) An efficient self-adaptive Python tool is developed to segment cloud chromatic properties using real-time sky images from total sky image repositories.
3) In optimizing the performance of W-O-convLSTM, an intelligent wrapper-based BorutaShap algorithm is designed to select the most relevant features from the cloud segmented statistical properties. Further optimization is achieved through hyperparameter tuning using a state-of-the-art O optimizer.
4) The non-stationarity behavior, periodicity and random fluctuations in the cloud chromatic properties and SZA over the temporal scales are addressed through the application of SWT with high and low frequency decompositions.
5) The efficacy of W-O-convLSTM in forecasting UVI is explored for the four seasons with robust statistical score metrics and visual analysis of all tested data alongside other competing benchmark and baseline models.

The rest of this paper is organized as follows: In Section II, we briefly present the related work and in section III, we discuss the theoretical overview. Afterward, we provide the methodology detailing the comparative experiments for UVI forecasts in section IV and then we present the results and discussion in section V. Finally, in section VI, we discourse the concluding remarks and future work.

II. RELATED WORK

While UVI measurement can be achieved using mechanistic surface measurement methods including the use of a pyranometer or spectroradiometer, its potential for broad application can be constrained by high costs and calibration issues [11]. Previous researches have applied deterministic methods to predict UVI but such approaches are restricted by assumed fixed or estimated initial conditions [12], [13]. Artificial intelligence (AI) based data-driven and DL algorithms are robust, cost-effective and user-friendly [14] but have not yet been applied to predict short-term UVI by utilizing stochastic cloud cover conditions. Though solar UVI has been forecasted with applications of artificial neural networks (ANN) [15], extreme learning machine (ELM) [7], deep belief networks (DBN) [16] and long short-term memory (LSTM) [17], integrating cloud effects can further boost the performance of highly competitive machine learning (ML) and DL methods.

A multiple-input DL convolutional long short-term memory (convLSTM) is currently gaining prominence as a powerful predictive tool. Having the convolutional operation embedded inside the long short-term memory (LSTM) cell, it robustly extracts statistically significant antecedent lagged inputs from the predictive variables whilst the LSTM learns from the sequentially incorporated features for low latency predictions [18], [19]. Recently, convLSTM was applied for flood index forecasts [20] and precipitation forecasts [21], and these studies illustrated the superiority of convLSTM

over the benchmarked counterparts. Being an intelligent and versatile predictive model, convLSTM is highly suitable for modeling cloud-affected UVI.

Feature selection approaches are essential components of the model designing phase to achieve the optimum performance of a forecast model. The Python-based BorutaShap algorithm remarkably eliminates irrelevant and largely redundant features, as revealed in a study where it was employed in identifying the strongest data series of winning and losing the Belgian professional soccer [22]. Along with utilizing selective filtering, the application of robust data decomposition schemes such as SWT efficiently accomplishes dimensionality reduction of the input variables. As a pre-processing tool, SWT was applied by [23] to effectively decompose the input signals into low-frequency and high-frequency components. The non-stationarity in electrocardiogram signal inputs [24] was also exploited using SWT decomposition.

III. THEORETICAL OVERVIEW

This section provides a brief overview of the operational mechanism of convLSTM in designing the proposed hybridized W-O-convLSTM model. Furthermore, we briefly discuss the three major phases of the UVI forecasting framework that includes feature selection by BorutaShap, data decomposition using SWT and Hyperparameter optimization by O algorithm.

A. OPERATIONAL MECHANISMS OF ConvLSTM

ConvLSTM is fundamentally an extension of LSTM networks that encapsulates the convolutional operation to robustly capture the underlying spatial features in large scale sequential and multi-dimensional datasets [25], [26]. With a time-series predictive framework as in our case, the convolutional operation at each gate (input, forget and output) of the LSTM cell replaces matrix multiplication to suitably extract spatiotemporal patterns in the 2-dimensional inputs [21], [25]. The future state of a cell in convLSTM is determined by its local neighbors' input and past state. While convLSTM retains the strengths of LSTM to capture long short-term memory, it further minimizes the redundancy of the fully connected structure, thus improving the training and prediction efficiency [27]. The key equations governing the operation of a single convLSTM unit are as follows [26], [28]:

$$\textit{Forget Gate } f_t = \sigma(W_f * [h_{t-1}, x_t] + W_{cf} \circ C_{t-1} + b_f) \quad (1)$$

$$\textit{Input Gate } i_t = \sigma(W_i * [h_{t-1}, x_t] + W_{ci} \circ C_{t-1} + b_i) \quad (2)$$

$$\textit{Intermediate State } S_t = tanh(W_c * [h_{t-1}, x_t] + b_c) \quad (3)$$

$$\textit{Update Cell } C_t = f_t \circ C_{t-1} + i_t \circ S_t \quad (4)$$

$$\textit{Output Gate } o_t = \sigma(W_o * [h_{t-1}, x_t] + W_{co} \circ C_t + b_o) \quad (5)$$

$$\textit{Output } h_t = o_t \circ tanh(C_t) \quad (6)$$

where '*' denotes convolution operator, '$\circ$' denotes Hadamard product, h_t is hidden state at sequential time t, C_t is cell state, S_t is intermediate state and the convLSTM gates i_t, f_t, o_t, are 3-dimensional tensors having the last two dimensions as spatial dimensions (rows and columns).

The operational mechanisms and explanations of the benchmarked models constructed using CNN [29], SVR [30] and PA [31] are elucidated elsewhere, as these methods are well-renowned.

B. WRAPPER-BASED BORUTASHAP

BorutaShap is an elegant Python-based wrapper method that combines the Boruta feature selection algorithm with shapely additive explanations. It is highly compatible and facilitates any tree-based learner such as RF, XGBoost, decision tree (DT), etc. as the base model [22], [32]. To select the most significant features, the Boruta algorithm creates shadow features (exact replicas) of each feature and shuffles the values in the shadowed features to remove their correlations with the response variable [33]. Thereafter, it passes the actual and shadow-shuffled features in the tree-based model to predict the target variable using the tree-based learner. It then determines the permutation importance or Mean Decrease Accuracy (MDA) for the actual and the shadow-shuffled inputs for overall trees (m_{tree}), given by the expression [34], [35]:

$$\text{MDA} = \frac{1}{m_{tree}} \sum_{m=1}^{m_{tree}} \frac{\sum_{t \in OOB} I\,(y_t = f\,(x_t)) - \sum_{t \in OOB} I\,(y_t = f\,(x_t^n))}{|OOB|} \quad (7)$$

where, x_t is group of predictor variables ($x_t \in R^n$) and y_t is target variable ($y_t \in R$) for n number of inputs in the set T (where $t = 1, 2, \ldots, T$), $I(\bullet)$ is indicator function, OOB is Out-of-Bag predictive error, $y_t = f\,(x_t)$ is predicted value before permuting and $y_t = f\,(x_t^n)$ is predicted value after permuting.

By performing a two-sided hypothesis test (t-test) for equality of both actual and shadowed, the algorithm calculates the z-score [32]. The z-score is determined by the expression:

$$\text{z score} = \frac{MDA}{SD} \quad (8)$$

where SD represents the standard deviation of accuracy losses. A threshold is set by the algorithm where the z-score of the actual feature must be greater than the maximum z-score (z_{max}) of the randomized shadow features. If the threshold criteria is met, the feature is selected to be important. Additionally, comparisons are made between the features and corresponding shadow features in terms of their shapely importance values (SHAP values), which produces a more consistent result [36].

C. STATIONARY WAVELET TRANSFORM (SWT)

SWT is a powerful mathematical tool for dimensionality reduction and data decomposition, which takes care of non-stationary, nonlinear and noisy signals [37]. It is a modified version of conventional discrete wavelet transform (DWT) that is designed to handle the issues of signal decimation in

DWT [38]. For a given signal, $x(t)$, its wavelet transform can be determined by the expression [37]:

$$X(\tau, a) = \frac{1}{\sqrt{|a|}} \int_{-\infty}^{\infty} x(t)\, \psi^* \left(\frac{t-\tau}{a} \right) dt \tag{9}$$

where '$*$' denotes complex conjugate, ψ is analyzing wavelet, a is time dilation, and τ is time translation. Therefore, the DWT of a signal, $x[m]$, is given by the expression:

$$X[k, l] = 2^{-(k/l)} \sum_{m=-\infty}^{\infty} x[m]\, \psi[2^{-k} m - 1] \tag{10}$$

By performing a DWT decomposition for the signal $x[m]$, the respective sub-signals of detailed components (DC) and approximation components (AC) are acquired [39]. However, due to signal decimation after each level of decomposition, the transform by DWT is not time-invariant, which makes the signal unsuitable for data preprocessing [37]. To overcome this drawback, SWT (an extension of DWT) is employed, as it uses the a-trous algorithm to solve the problem of shift-invariance [38]. Having undecimated wavelet transform, the size of SWT data is efficiently preserved through the low-pass and high-pass filters. Thus, the length of the detailed and approximation coefficients are the same in comparison with the original signal [40]. Using SWT, the decompositions can be computed using the expressions [41]:

$$cA_{n,m}^{SWT} = \sum_u cA_{n-1,m+2^n(u)}^{SWT} g(u) \tag{11}$$

$$cD_{n,m}^{SWT} = \sum_u cD_{n-1,m+2^n(u)}^{SWT} h(u) \tag{12}$$

where $cA_{n,m}^{SWT}$ is the approximation coefficient of SWT, $cD_{n,m}^{SWT}$ is the detailed coefficient of SWT, n, m is the number of decomposition levels and the position, $g(u)$ is the low pass filter and $h(u)$ is the high pass filter. The Python-based SWT presents several mother wavelets for data decomposition and signal denoising, among which 'haar' and 'db' are widely utilized [23], [24].

D. OPTUNA (O) OPTIMIZER

The O algorithm is a next-generation hyperparameter optimization framework with a define-by-run API that provides the platform to construct the parameter search space dynamically via efficient searching and pruning strategies [42]. In searching ideal hyperparameter values, O utilizes various samplers such as random, grid, Bayesian, and genetic calculations [43]. During the process of optimization, the O algorithm achieves optimal solution by repeatedly calling and evaluating the objective function of different parameter values. The following steps describe the optimization process by O algorithm [44]:

Step 1: Determine the direction of optimization, type of parameter, range of values and the maximum number of iterations.

Step 2: Enter the loop;

Step 2.1: Uniformly select a population of individuals within the function defining the parameter value range;

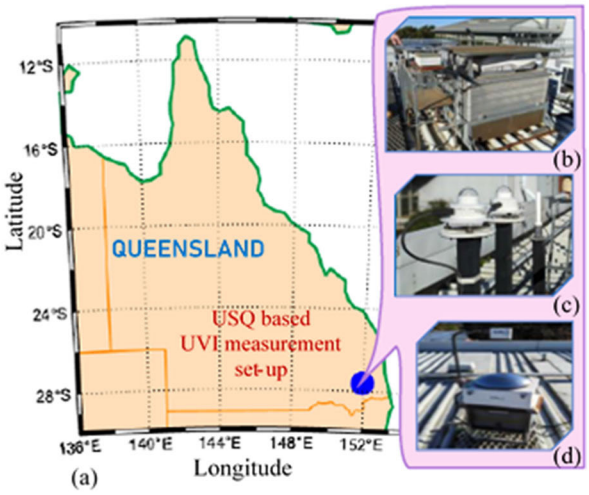

FIGURE 1. (a) Geographic location of the USQ-based experimental site in Toowoomba, Australia to validate wavelet hybrid convLSTM model. (b) Roof-top mounted Bentham DTM300 Spectroradiometer for UVR measurement. (c) Co-located 501 broadband UVR Biometer. (d) Synchronous Total Sky Imager, TSI440 set-up to capture sky images and record SZA.

Step 2.2: Automatically terminate the hopeless population individuals according to the trimming conditions with a trimmer;

Step 2.3: Determine the objective function value of the unpruned individual populations;

Step 2.4: Repeat the above steps for the loop and exit when the maximum number of iterations is reached.

Step 3: Provide the output as the optimal solution and optimal function value.

The O optimizer is gaining eminence as it provides an optimum combination of hyperparameters with relatively lower computation cost in comparison with other optimization methods such as exhausted grid search and random grid search [45].

IV. METHODOLOGY

In this section, we describe our study location and datasets for the UVI modeling experiments. Thereafter, we discuss the process of segmenting cloud statistical properties from the sky images. Finally, we present the stages involved in designing the proposed W-O-convLSTM model, followed by a discussion on model evaluation using robust statistical score metrics.

A. EXPERIMENTAL SITE AND DATASETS

To validate the W-O-convLSTM model, the study site of the experimental set-up was based at the University of Southern Queensland (USQ) in Toowoomba (Latitude of 27.60 °S and Longitude of 153.93 °E), Australia, as illustrated in Fig. 1(a). Geographically, the experimental site is located approximately 100 km inland relative to the ocean and experiences limited marine aerosol and anthropogenic effects [7]. Being

a subtropical region, Queensland receives a large number of sunshine days annually, which poses a significant impact on the public health sector in terms of UV-exposure-related skin and eye diseases.

We measured the time-series solar spectral irradiance using the Bentham DTM300 Spectroradiometer (Bentham Instruments Inc., UK), mounted on a roof-top at the USQ Toowoomba campus, as shown in Fig. 1(b). Using the measured solar spectral irradiance, the UVI data was calculated based on the International Commission on Illumination (CIE) reference action spectrum for UV-induced erythema on the human skin [5]. As per the CIE guidelines, we first determined the erythemally active UV irradiance (UVE) by integrating the monochromatic UV irradiance ($S(\lambda)$) that is weighted with the CIE spectral action function CIE(λ) and bounded within the wavelengths of 280 nm to 400 nm as follows [46]:

$$\mathrm{UVE} = \int_{280}^{400} S\,(\lambda)\,.\mathrm{CIE}\,(\lambda)\,.\mathrm{d}\lambda \tag{13}$$

Having one unit of UVI equivalent to 25 mW m^{-2} of erythemally effective exposure to UVR, we calculated the UVI from the UVE as follows [46], [6]:

$$\mathrm{UVI} = \frac{1}{25\mathrm{mWm}^{-2}} \int_{280}^{400} S\,(\lambda)\,.\mathrm{CIE}\,(\lambda)\,.\mathrm{d}\lambda \tag{14}$$

The calculated UVI is a unitless normalized index, for which the values range globally from 0 to 11+. As the UVI increases, the exposure severity and potential for damage to the skin and eye rises.

We acquired the UVI datasets at a time resolution of 10 minutes. However, there were instances when these datasets were missing due to power failure or maintenance of the spectroradiometer. The missing datasets were recovered with the UVI calculated using the minimal erythema dose (MED) measurements of a co-located 501 broadband UVR Biometer (Solar Light Co., USA), as shown in Fig. 1(c). To avoid any UVI anomalies measured by two different instruments, the Biometer was initially calibrated to the Bentham spectroradiometer using a time-dependent conversion factor (*CF*). Consequently, the Biometer-derived UVI was calculated as follows:

$$\mathrm{UVI} = (MED \times CF \times 40)/300 \tag{15}$$

where *MED* is the minimal erythema dose measured by the Biometer at every 5 minutes (300 s) and *CF* is a conversion factor (different for each season). Considering that one unit of MED is equivalent to 200 J/m^2 of erythemally weighted UV radiation [47], MED is converted to J/m^2 by multiplying with *CF*. UVI is calculated from the erythemally weighted UV by multiplying the erythemal irradiance in units of W/m^2 by 40.

Thereafter, we extracted the sky images that were captured by a synchronous co-located Total Sky Imager - TSI440 (TSI) (Yankee Environmental Systems Inc., USA), as shown in Fig. 1(d). These sky images were stored in the TSI repository. The records of SZA were also extracted from the TSI at 10 minutes intervals. We extracted the UVI, sky images and SZA data series for a complete year (from 01-Mar-2003 to 29-Feb-2004) to obtain the datasets for all 4 seasons. For each day, the datasets were extracted from 7.40 am to 4.10 pm. We segmented the sky images to extract the cloud statistical properties. While we utilized the UVI datasets as the target input, the cloud statistical properties and SZA datasets were employed as the input features in model building.

B. SEGMENTING CLOUD STATISTICAL PROPERTIES

Cloud statistical properties were essential input predictor variables in designing the W-O-convLSTM model and these variables were segmented from the sky images stored in the TSI repository. The TSI repository saves a suite of files that contain colored sky images in JPEG format, a properties text file and a TSI segmented image in PNG format with cloud and non-cloud parts of the clear sky. The properties text file contains the sun position, SZA and cloud fraction information. We utilized the TSI segmented PNG image and cloud fraction information to validate our segmented sky images through comparisons of blue sky and cloud cover. To segment the sky images from the suite of files, we designed an automated Python tool that reads all the 10 minutes sky images in JPEG format and extracts the cloud statistical properties for each image. The image segmentation algorithm, referred as the Python tool has been designed in the Python (version 3.7.9) environment. A flowchart shown in Fig. 2 demonstrates the algorithm execution process of the proposed automated Python tool to segment the cloud chromatic statistics. The Python-based ''glob'', ''os'' and ''cv2'' libraries were utilized to locate and read the real-time sky image and properties files. Using the ''linecache'' library, a common line was read from the properties file and if this line was missing, the image was reported as corrupt. Otherwise, the image of background, camera housing, camera arm and sun-shield captured in the sky image were all masked using the ''numpy'' library, as shown in Fig. 3. Thereafter, the sky image was split into red (R), green (G) and blue (B) channels, from which R and B channel arrays were utilized for further analysis by applying previously reported image segmentation techniques [48]. Using the R and B channels, the red-blue ratios (RBR) of the pixels were determined. RBR has been a commonly applied threshold in segmenting cloud cover and blue sky that maintains a high resolution of the image despite getting downsampled when saved in JPEG format [49]. To increase contrast, the RBR pixel values were scaled within 0 to 255 [50], [48]. A calculated threshold (T) was applied to binarize and segment the RBR-scaled pixels into black and white. The T was determined as follows:

$$T = (255 \times TF)/RBR\_max \tag{16}$$

where *TF* is a threshold factor of 0.56 [48] (usually between 0 to 1) and *RBR_max* is the maximum RBR. If the pixel values

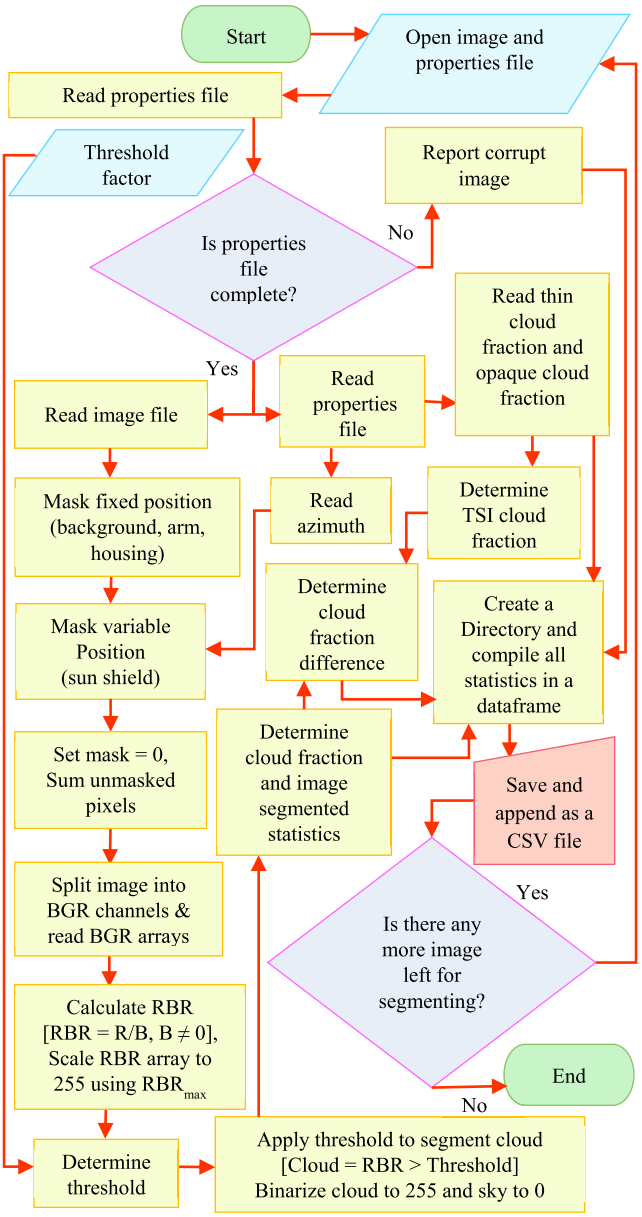

FIGURE 2. Flowchart describing the algorithm execution process of the proposed automated python tool for extracting the cloud statistical properties from the TSI440 repository-based sky images.

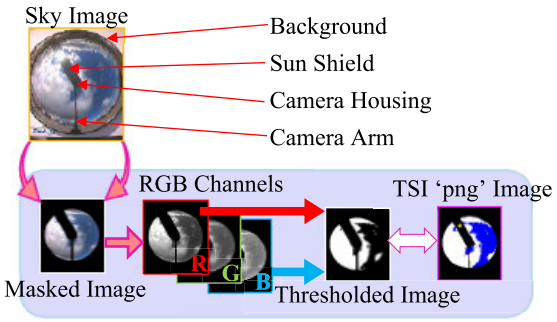

FIGURE 3. Sky image segmentation and comparisons with TSI segmented PNG image.

were greater than T, they were assigned 255 (white color) to represent the cloud cover, else, they were assigned 0 (black color) to represent the blue sky. The binarized pixel values of cloud cover and blue sky were masked onto the pixels of red and blue channels to obtain the segmented statistics of the sky image. Finally, the Python-based tool was automated via a for loop to perform the same operations in segmenting the entire JPEG sky images within the suite. Our segmentation program is an improvement of the previously reported methods [48], which shows very close segmentation with the segmented TSI PNG image, as illustrated in Fig. 3. Upon comparing our image segmentation with the TSI-based image segmentation in terms of cloud percentages, we achieve a very low cloud percent difference of 1.84%. Further comparisons showed that the original and calculated cloud fraction data of the segmented images had a very strong correlation of 0.991. The cloud statistical properties are segmented as red and blue channel pixel averages, standard deviations, ratios, differences, TSI-based thin cloud and TSI-based opaque cloud. The cloud chromatic properties and SZA provided 16 time-dependent predictor inputs to validate the proposed multiple input multi-step output W-O-convLSTM model for UVI forecasts. We present the descriptions of these 16 predictor variables and UVI (predictand) in Table 1.

C. MISSING DATA RECOVERY

After acquiring the data series, it was noted that there were some missing values in the UVI and cloud statistical properties data. However, the SZA datasets were complete. The cloud statistical properties were incomplete due to some missing and corrupt images from the TSI repository. In the case of the UVI datasets, some incomplete values were observed because the 501 Biometer UVI used to recover the Bentham UVI were missing occasionally. These missing values were duly imputed with the monthly median of the respective variable at the same daily time domain. Among the three commonly used imputation methods of mean, median and listwise deletion, the median imputation approach is more accurate and robust [51].

D. DEVELOPMENT OF THE PROPOSED PREDICTIVE MODEL

The scope of this research was to develop a wavelet hybrid convLSTM model that entails 3 major phases, which include feature selection by BorutaShap, decomposition of the selected features using SWT and hyperparameter optimization by O algorithm. In designing this AI-based UVI forecasting model, the Python programming language (version 3.7.9) was implemented. For hyperparameter optimization using the O algorithm, we used Google Colab with python programming as it provides freely available computing resources that include a graphics processing unit (GPU). The Python tool is highly versatile, as its virtual environment provides the platform for both ML and DL-based data

TABLE 1. Descriptions and inferential statistics of the predictor and target variables used to develop the proposed W-O-convLSTM model to forecast UVI.

Input Variables	Symbol	Definitions and Descriptions	Inferential Statistics of Predictor Variables						Cross correlations of Predictor Variables with UVI
			Mean	St. Dev.	Median	Min	Max	Skew	
Objective Variable									
Global Solar Ultraviolet Index	*UVI*	Global solar ultraviolet index is a measure of the level of ultraviolet radiation.	5.65	4.18	4.55	0.03	17.88	0.80	
Predictor Variables									
Solar Zenith Angle *(°)* (Baseline predictor variable)	*SZA*	Angular position of the sun measured as an angle between the position of the sun and normal to earth's horizontal plane.	45.28	17.15	47.67	4.59	80.68	-0.30	-0.89
Sky Ratio in Red and Blue Channel	SRB_r	Ratio of the pixel value averages in the red and blue channels representing blue sky.	0.49	0.16	0.53	0.00	0.78	-2.23	0.35
Cloud Standard Deviation in Blue Channel	CB_s	Standard deviation of pixel values in the blue channel representing cloud cover.	7.40	4.13	9.73	0.00	15.52	-1.07	0.26
Average Cloud in Blue Channel	CB_a	Average of pixel values in the blue channel representing cloud cover.	182.17	67.61	186.81	0.00	255.00	-1.59	-0.24
Average Cloud in Red Channel	CR_a	Average of pixel values in the red channel representing cloud cover.	159.84	57.04	166.84	0.00	236.95	-1.89	-0.24
Sky Difference in Red and Blue Channel	SRB_d	Difference in the average pixel values representing blue sky in red and blue channels.	75.35	38.52	74.35	-49.85	1239.50	3.14	-0.24
Cloud Difference in Red and Blue Channel	CRB_d	Difference in the average pixel values representing clouds in red and blue channels.	22.17	13.90	20.33	-12.03	111.29	0.24	-0.20
Cloud Standard Deviation in Red Channel	CR_s	Standard deviation of pixel values in the red channel representing cloud cover.	8.63	3.21	9.96	0.00	15.16	-2.11	0.15
Average Sky in Blue Channel	SB_a	Average of pixel values in the blue channel representing blue sky.	160.44	79.00	168.04	0.00	4219.50	13.24	-0.13
Opaque Cloud	*OC*	Thick cloud cover proportion in the sky.	0.35	0.36	0.24	0.00	1.00	0.69	-0.12
Cloud Ratio in Red and Blue Channel	CRB_r	Ratio of the pixel value averages in the red and blue channels representing clear sky.	0.80	0.26	0.87	0.00	1.07	-2.62	0.10
Sky standard deviation in blue channel	SB_s	Standard deviation of pixel values in the blue channel representing blue sky.	32.18	117.64	17.60	0.00	3830.95	15.37	-0.09
Cloud Fraction	*CF*	Fraction of the number of cloud pixels and the total number of unmasked pixels.	0.39	0.37	0.32	0.00	1.00	0.46	-0.09
Sky standard deviation in red channel	SR_s	Standard deviation of pixel values in the red channel representing blue sky.	32.33	113.91	17.73	0.00	3726.13	15.36	-0.07
Thin Cloud	*TC*	Thin cloud cover proportion in the sky.	0.03	0.05	0.01	0.00	0.62	4.30	-0.06
Average Sky in Red Channel	SR_a	Average of pixel values in the red channel representing blue sky.	84.51	45.18	92.00	0.00	2980.00	24.56	0.04

analysis through its eminent packages such as Scikit-learn, Tensorflow and Keras [52], [53], [54].

The schematic diagram in Fig. 4 provides an overview of the stages involved in designing the proposed predictive model. In accordance with the stages illustrated in the schematic diagram, the details of the methods adopted at each stage of the UVI forecasting framework are as follows:

Stage 1: This stage involves an assessment of the cross-correlations (r_{cross}) between the 10 minutes measured UVI (i.e. $UVI(t)$) and each of the 16 predictor variables (i.e. $X_1(t-n), X_2(t-n), X_3(t-n), \ldots\ldots, X_{16}(t-n)$, where t is time and n is the most significant antecedent lag). Statistically, the individual predictors exhibiting the most significant correlation from the lagged combinations were selected to generate UVI forecasts. Table 1 enumerates the r_{cross} values and the inferential statistics of these input variables. Once the significant antecedent lagged inputs of UVI and the 16 attributes were determined, the data series were reshaped for simulating the future UVI over multi-step horizons. We describe these forecast horizons in Table 2, where the 10 minutes, 20 minutes, 30 minutes and hourly ahead forecasts are designated as 10M, 20M, 30M and 60M, respectively. In reshaping the datasets, a lagged matrix was constructed for each of the four forecast timescales.

TABLE 2. Designation of models and forecast horizons (Note: ***10M indicates a 10-minute forecast horizon***).

Designated Model	Label	Forecast Horizon	Label
W-O-convLSTM	M1	10 minutes	10M
O-convLSTM	M2	20 minutes	20M
O-CNN	M3	30 minutes	30M
O-SVR	M4	1 hour	60M
O-PA	M5		
W-O-convLSTMsza	M6		

Stage 2: This stage describes the application of a wrapper-based BorutaShap algorithm for effective feature selection. After feeding the UVI and 16 attributes into BorutaShap, it robustly selected the pertinent features and captured the significant antecedent memory of UVI behavior to deliver

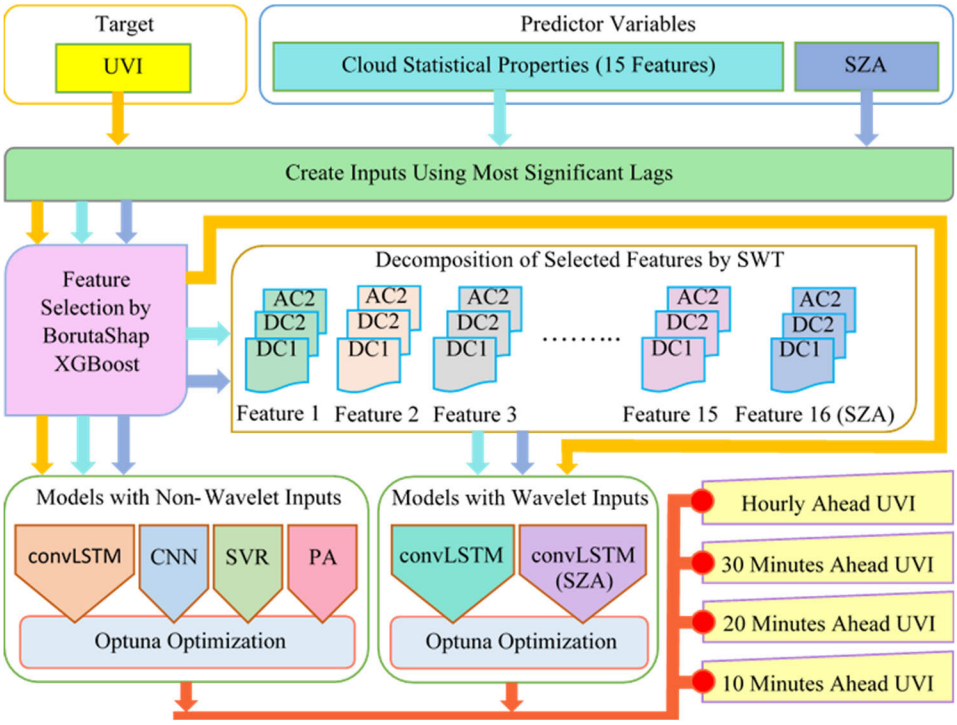

FIGURE 4. Schematic diagram detailing the construction of the proposed multiple input, multi-step output model for solar UVI forecasts.

multi-step forecasts. In identifying the most significant input variables, XGboost was utilized as the base model for screening each of the four forecast horizon data series. During the process of screening, consistency was maintained in identifying the feature importance through the aggregated and sorted SHAP values. The outcome of feature selection revealed that all the 16 predictor variables in each of the four forecast horizon datasets were pertinent and BorutaShap selected them as important features for model building. For instance, Fig. 5(a) presents the outcome of feature selection for 10 minutes forecast horizon datasets using the BorutaShap feature importance plot. The plot marks all the 16 predictors as pertinent. In addition, Fig. 5(b) presents a bee-swarm plot that illustrates the feature importance of these predictors based on their SHAP values.

The criterion in designing the proposed W-O-convLSTM model is to utilize the historical memories and BorutaShap feature selection of the inputs acquired from the diversified characteristics of UVI and cloud statistical properties data series. If the lagged values delay the two samples (i.e. predictors and predictand), by applying this criterion, they can be regarded as statistically independent.

Stage 3: This stage describes the segregation of input datasets into respective seasons, followed by the train-test split. The time-series datasets prepared for each forecast horizon were initially segregated into four different seasons. As detailed in Table 3, autumn (01-Mar-2003 to 31-May-2003), winter (01-Jun-2003 to 31-Aug-2003), spring (01-Sep-2003 to 30-Nov-2003) and summer (01-Dec-2003 to 29-Feb-2004) were assigned with 4784, 4784, 4732 and 4732 data points, respectively. Thereafter, each seasonal-based data series was split into a training set (84.6% to 84.8%), a validation set (10% of training data) and a testing set (15.2% to 15.4%). Such training and testing split were employed because we utilized 11 weeks datasets for training and 2 weeks datasets for testing during all four seasons. These datasets were extracted at 10 minutes interval, so we had a sufficient number of data points (4732 to 4784) for each season to develop the proposed model. Some earlier studies have also employed a similar train-test split. For instance, the study by [55] employed a train-test split on monthly-based datasets with a training split of 71.45% to 75.01% and a testing split of 12.59% to 14.39% for four sites. A similar approach for the train-test split was also adopted by [19] and [56]. Subsequently, all the model input datasets as per Table 1 were normalized between [0 – 1] to improve the efficiency and accuracy during training and testing phases [7].

Stage 4: This stage employs SWT to address the issues pertaining to non-stationarity and noise in the input data signals. The train-test split of the input datasets was conducted prior to SWT decomposition to prevent the leakage of training data into the testing sets, as this could add bias into the forecast [57]. In decomposing the lagged feature data series, SWT convolved each cloud statistical property and SZA signal through high and low pass filters into detailed components (DC) and approximation components (AC) without performing any decimation. Identifying

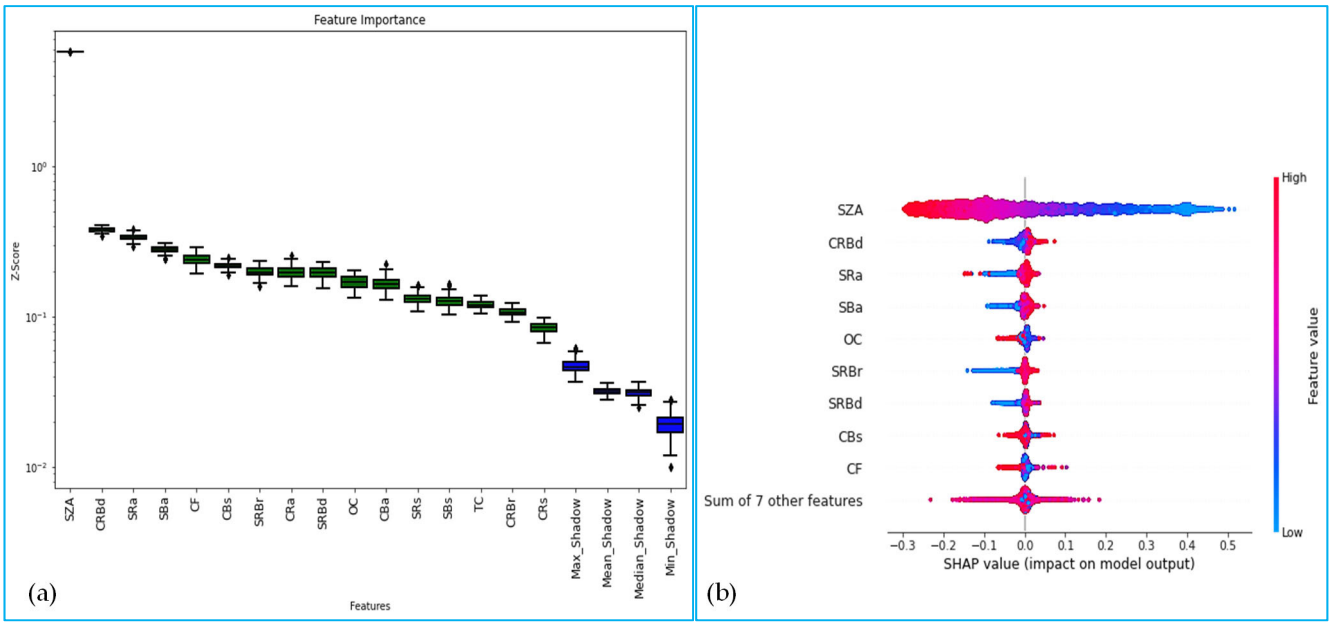

FIGURE 5. (a) BorutaShap-derived feature importance of the cloud segmented properties and SZA for 10 minutes forecast, (b) Beeswarm plot of feature importance based on shapely values.

TABLE 3. Seasonality-based data segregation into training, validation and testing phases to experiment the time-series W-O-convLSTM model in Toowoomba, Queensland.

Seasons	Period	Data Points	Training (84.6% to 84.8%)	Validation (% Data)	Testing (15.2% to 15.4%)
Autumn	01-Mar-2003 to 31-May-2003	4784	4056	10% of training data	728
Winter	01-Jul-2003 to 31-Aug-2003	4784	4056		728
Spring	01-Sep-2003 to 30-Nov-2003	4732	4004		728
Summer	01-Dec-2003 to 29-Feb-2004	4732	4004		728

the type of SWT scaling filter and level of decomposition was a critical task to achieve a remarkable wavelet-coupled model, as no specific method for such selection is confirmed in the literature [30], [39]. In our case, a trial and error method was adopted in selecting the best mother wavelet and decomposition level [58]. Among the SWT mother wavelets (that includes Daubechies (db), Haar (haar), Symlets (Sym), Coiflets (coif), Biorthogonal (bior), Reverse biorthogonal (rbio) and Gaussian (gaus)) and decomposition levels (that includes 2, 3, 4, 5, 6 and 7), optimum performance was achieved in designing the proposed model using haar wavelet at a decomposition level of 2. These SWT parameters search space and optimum parameters are highlighted in Table 4. Moreover, Fig. 6 illustrates the training phase decomposition of the attribute CBR_d into its detailed coefficients (D1 and D2) and approximation coefficient (A2) at 10 minutes forecast horizon in summer. The other attributes were decomposed in a similar manner for all four forecast timescales. While A2 seems to be in phase with the original undecomposed predictor variables, D1 and D2 turn out to replicate greater details of the subtle but significant patterns in the time-series inputs.

Stage 5: In this stage, we discuss the architectural design of the proposed hybridized convLSTM model and hyperparameter optimization using the O algorithm. The architecture of the deep learning convLSTM model consists of double convLSTM2D layers that robustly extract the complex behavior of antecedent lagged features. With RELU assigned as the activation function for the two layers, each layer was allocated with 100 and 44 filters, respectively. These were the optimal number of filters tuned by employing the powerful O algorithm. A flattening layer was integrated after each convLSTM2D layer. Finally, a dense layer was utilized to generate forecasts of future UVI as output. An improved performance was achieved with O optimized hyperparameters that include a batch size of 104 and epochs of 189. In adopting regularization to reduce overfitting and to improve the training performance, a good dropout of 0.1 was applied. To further minimize the issue of overfitting, we adopted a 10 fold cross-validation strategy. Table 4 presents the search space and

TABLE 4. Search space in the model design phase with optimum architecture of the objective model.

Model	SWT Parameters and Model Hyperparameters	SWT and O-based Model Search Space
W-O-convLSTM (M1)	Decomposition levels	2, 3, 4, 5, 6, 7
	Mother wavelets	db, haar, sym, coif, bior, rbio, gaus
	Filter 1, Filter 2	[40 - 130], [10 - 60]
	Activation function	[ReLU]
	Batch Size, Epochs	[100 - 300], [80 - 300]
	Dropout, Optimizer	[0.05, 0.1], [Adam]
O-convLSTM (M2)	Filter 1, Filter 2	[60 - 110], [20 - 60]
	Activation function	[ReLU]
	Batch Size, Epochs	[100 - 300], [80 - 300]
	Dropout, Optimizer	[0.05, 0.1], [Adam]
O-CNN (M3)	Filter 1, Filter 2, Filter 3	[80 - 500], [20 - 200], [2 - 50]
	Padding, Pooling size	Same, 2
	Activation function,	[ReLU],
	Batch Size, Epochs	[100 - 500], [100 - 500]
	Dropout, Optimizer	[0.05, 0.1], [Adam]
O-SVR (M4)	Kernel	[poly, rbf, sigmoid]
	Gamma, Epsilon	[scale, auto], [0.1 - 0.5]
	Degree, C	[2 - 5], 1
O-PA (M5)	Tol	[0.001 - 0.002]
	C, Epsilon	[1 - 2], 0.1
	Maximum iteration	[100 - 200]
W-O-convLSTMsza (M6)	Decomposition levels	2, 3, 4, 5, 6, 7
	Mother wavelets	db, haar, sym, coif, bior, rbio, gaus
	Filter 1, Filter 2	[40 - 130], [20 - 50]
	Activation function,	[ReLU]
	Batch Size, Epochs	[100 - 300], [80 - 300]
	Dropout, Optimizer	[0.05, 0.1], [Adam]

Optimum Architecture of the Proposed W-O-convLSTM

Optimum SWT Parameters:

Wavelet type: haar

Number of Decompositions = 2

Optimum O-Based Model Hyperparameters:

ConvLSTM2D layer 1 filters = 100

ConvLSTM2D layer 2 filters = 44

Activation function = ReLU, Dropout = 0.1,

Optimizer = Adam, Batch Size = 104, Epochs = 189

Learning rate = 0.001, $\beta_1 = 0.9$, $\beta_1 = 0.999$, Epsilon = $1x10^{-10}$

optimal hyperparameters of the proposed W-O-convLSTM model (also labeled as M1). To comprehensively benchmark the proposed W-O-convLSTM model, we deployed other highly competitive counterparts. These counterparts were non-wavelet-based models that were developed using convLSTM, convolutional neural network (CNN), support vector regression (SVR) and passive-aggressive (PA) models. The hyperparameters of these benchmarked models were also optimized using the O algorithm. We designated these models as O-convLSTM (also labeled as M2), O-CNN (M3), O-SVR (M4) and O-PA (M5), respectively. In an earlier study by [7], UVI was forecasted by developing machine learning models using a single predictor input of SZA without considering the cloud cover effects. In this study, we design our deep learning UVI forecasting model (M1) using the attributes of cloud statistical properties (that define the cloud cover conditions) and SZA to claim that M1 will yield superior performance in comparison with a deep learning baseline model developed using the predictor input of SZA alone. We designated the baseline model developed using SZA as W-O-convLSTMsza (also labeled as M6). Though M1 and M6 were fed with different predictor inputs, they were both wavelet hybrid convLSTM models with similar architectural designs. It was important to compare the performance of our objective model (M1) with the baseline model (M6) due to a significant dependence of UVI on SZA. It is known that when the sun is out, we have SZA and SZA is highly correlated with UVI. For instance, Table 1 displays the highest correlation (0.89) between SZA and UVI in comparison with all other predictors. The model designations and O-based hyperparameter search space of the objective, benchmarked and baseline models are presented in Table 2.

E. PERFORMANCE EVALUATION OF THE MODEL

To confirm the superiority of the W-O-convLSTM model in UVI forecasting, we evaluated this model against the baseline and benchmarked models. To validate that the use of cloud cover effects could further improve the performance of the objective model, we evaluated our model alongside the baseline model. Additionally, by evaluating our objective model (SWT-based model) alongside the benchmarked models (non-SWT-based models), we validated the superiority of employing SWT over non-SWT model design in forecasting UVI. Here, our focus was to evaluate SWT against non-SWT-based models, so other wavelet transforms such as DWT were not evaluated. While DWT is a known standard frequency transform, it was not applied to benchmark SWT in our study because the DWT algorithm exhibits significant problems associated with signal decimation. Such decimation effects induce a bias in the model that makes the signal unsuitable for data preprocessing [30], [37]. On the other hand, SWT is a modified version of the conventional DWT that utilizes an a-trous algorithm to overcome the issues of signal decimation [38]. This drawback of DWT confirms the superiority of SWT during data preprocessing, thus eliminating the need for evaluating the DWT-based models.

A number of robust statistical metrics were applied to rigorously evaluate the hybridized W-O-convLSTM model alongside other competing counterparts in forecasting short-term UVI. For this study, the commonly adopted model score metrics, such as Pearson's Correlation Coefficient (r),

TABLE 5. The testing phase performance of W-O-convLSTM model against competing counterparts in terms of correlation coefficient (r), root mean squared error (rmse), mean absolute error (mae) for UVI forecast.

Forecast Horizon	Model	Autumn			Winter			Spring			Summer		
		r	MAE	RMSE	r	MAE	RMSE	r	MAE	RMSE	r	MAE	RMSE
10 min	M1	**0.961**	**0.017**	**0.024**	**0.909**	**0.033**	**0.049**	**0.926**	**0.050**	**0.078**	0.936	**0.054**	**0.077**
	M2	0.958	0.020	0.025	0.905	0.035	0.049	0.918	0.051	0.080	**0.940**	**0.054**	0.079
	M3	0.931	0.032	0.040	0.902	0.035	0.050	0.915	0.067	0.090	0.929	0.058	0.079
	M4	0.873	0.043	0.055	0.822	0.057	0.072	0.876	0.079	0.101	0.904	0.071	0.094
	M5	0.875	0.040	0.051	0.845	0.057	0.071	0.883	0.079	0.097	0.855	0.096	0.123
	M6	0.932	0.030	0.042	0.866	0.050	0.065	0.858	0.069	0.104	0.906	0.085	0.102
20 min	M1	**0.960**	**0.016**	**0.025**	**0.903**	**0.035**	**0.051**	**0.919**	**0.054**	**0.083**	**0.933**	**0.052**	**0.077**
	M2	0.953	0.020	0.028	0.901	0.040	0.057	0.917	0.056	0.085	**0.933**	0.054	**0.077**
	M3	0.918	0.033	0.043	0.901	0.037	**0.051**	0.913	0.083	0.105	0.924	0.057	0.082
	M4	0.863	0.042	0.054	0.807	0.057	0.072	0.863	0.084	0.104	0.885	0.081	0.101
	M5	0.870	0.040	0.053	0.826	0.055	0.073	0.857	0.089	0.108	0.853	0.087	0.115
	M6	0.929	0.033	0.044	0.863	0.045	0.061	0.857	0.078	0.104	0.905	0.091	0.107
30 min	M1	**0.939**	**0.028**	**0.037**	**0.888**	**0.040**	**0.057**	**0.913**	**0.068**	**0.091**	**0.924**	**0.059**	**0.083**
	M2	0.918	0.042	0.051	0.875	0.044	0.058	0.907	0.070	0.098	0.921	0.060	0.088
	M3	0.875	0.039	0.048	0.840	0.050	0.068	0.887	0.091	0.117	0.919	0.068	0.092
	M4	0.758	0.053	0.064	0.707	0.069	0.083	0.757	0.109	0.136	0.771	0.111	0.137
	M5	0.758	0.088	0.105	0.695	0.072	0.089	0.697	0.125	0.150	0.757	0.142	0.182
	M6	0.922	0.038	0.049	0.860	0.045	0.062	0.848	0.075	0.110	0.899	0.077	0.097
Hourly	M1	**0.938**	**0.026**	**0.034**	**0.872**	**0.043**	**0.060**	**0.899**	**0.081**	**0.107**	**0.920**	**0.058**	**0.084**
	M2	0.899	0.057	0.066	0.858	0.049	0.066	0.882	0.082	0.115	0.911	0.065	0.091
	M3	0.810	0.066	0.083	0.855	0.048	0.064	0.883	0.083	0.110	0.919	0.065	0.089
	M4	0.693	0.058	0.071	0.653	0.074	0.089	0.718	0.118	0.147	0.736	0.119	0.146
	M5	0.622	0.140	0.157	0.643	0.074	0.089	0.659	0.174	0.215	0.672	0.132	0.159
	M6	0.929	**0.026**	0.035	0.854	0.045	0.062	0.825	**0.081**	0.115	0.895	0.081	0.099

Root Mean Squared Error (RMSE), Mean Absolute Error (MAE), Coefficient of Determination (R2), Legate-McCabe's Index (LM), Willmott's Index (WI), Nash-Sutcliffe Efficiency (NSE), Relative Root Mean Square Error (RRMSE) and Relative Mean Absolute Error (RMAE) [18] were employed.

$$r = \frac{\sum_{i=1}^{N}(UVI_i^O - \bar{UVI}^O)(UVI_i^F - \bar{UVI}^F)}{\sqrt{\sum_{i=1}^{N}(UVI_i^O - \bar{UVI}^O)^2}\sqrt{\sum_{i=1}^{N}(UVI_i^F - \bar{UVI}^F)^2}} \quad (17)$$

$$RMSE = \sqrt{\frac{1}{N}\sum_{i=1}^{N}(UVI_i^F - UVI_i^O)^2} \quad (18)$$

$$MAE = \frac{1}{N}\sum_{i=1}^{N}\left|UVI_i^F - UVI_i^O\right| \quad (19)$$

$$LM = 1 - \left[\frac{\sum_{i=1}^{N}\left|UVI_i^O - UVI_i^F\right|}{\sum_{i=1}^{N}\left|UVIi^O - \bar{UVI}^O\right|}\right] \quad (20)$$

$$WI = 1 - \left[\frac{\sum_{i=1}^{N}\left(UVI_i^F - UVI_i^O\right)^2}{\sum_{i=1}^{N}\left(\left|UVI_i^F - \bar{UVI}^O\right| + \left|UVI_i^O - \bar{UVI}^O\right|\right)^2}\right] \quad (21)$$

$$NSE = 1 - \left[\frac{\sum_{i=1}^{N}\left(UVI_i^O - UVI_i^F\right)^2}{\sum_{i=1}^{N}\left(UVI_i^O - \bar{UVI}^O\right)^2}\right] \quad (22)$$

$$RRMSE = \frac{\sqrt{\frac{1}{N}\sum_{i=1}^{N}(UVI_i^F - UVI_i^O)^2}}{\frac{1}{N}\sum_{i=1}^{N}(UVI_i^O)} \times 100 \quad (23)$$

$$RMAE = \frac{1}{N}\sum_{i=1}^{N}\left|\frac{UVI_i^F - UVI_i^O}{UVI_i^O}\right| \times 100 \quad (24)$$

where UVI_i^O, UVI_i^F = observed and forecasted UVI for the i^{th} observation, $\bar{UVI}^O, \bar{UVI}^F$ = average observed and forecasted UVI, N = Total number.

It is to be noted that the results obtained through these score metrics may also be due to chance or decisive. So, to prevent rejection of an equally good parallel model due to stochastically generated performance metrics, we further evaluate their forecast accuracies using an efficient statistical test, known as Diebold–Mariano (DM) test. For details of the DM test, the readers may refer to [59].

V. RESULTS AND DISCUSSION

This section presents an account of the empirical results to appraise and demonstrate the merits of the newly designed W-O-convLSTM model (M1) in UVI forecasting. The forecasting performance and efficacy are assessed against highly competitive counterparts of O-convLSTM (M2), O-CNN (M3), O-SVR (M4), O-PA (M5) and W-O-convLSTMsza (M6) at multi-step horizons using a plethora of statistical score metrics, as described in (17) – (24).

Table 5 presents the testing phase performance evaluation of the developed models for the seasons of autumn, winter, spring and summer at different forecasting timescales (the optimal performance is highlighted in red). For almost all the experimentally captured modeling aptitudes having the highest Pearson's correlation coefficient (r), lowest mean absolute error (MAE) and lowest root mean square error (RMSE), the proposed hybridized W-O-convLSTM model outperforms the comparative models in forecasting seasonal-based UVI at 10M, 20M, 30M and 60M horizons. Overall, the proposed model highlights its best performance against the competing counterparts in autumn-based 10M forecast horizon with statistical scores of r = 0.961, MAE = 0.017 and RMSE = 0.024 with respect to r = [0.873-0.958], MAE = [0.020-0.043] and RMSE = [0.025-0.055], where [-] denote lower and upper statistical bounds. In terms of r values, the W-O-convLSTM model shows the best performance in all the seasons for each forecast horizon, except for the summer-based 10M forecast. At this instance, the non-wavelet hybrid O-convLSTM model executes slightly better. Despite the subtle variation, our objective model shows a very close performance with respect to the O-convLSTM model, having a very low difference in r values (≈0.004). The MAE and RMSE values approach 0, indicating that our model is approaching a high level of precision. Moreover, a decline in performance accuracy is observed with increasing forecast horizons.

To completely gauge and understand the W-O-convLSTM model, it was rigorously evaluated with Willmott's Index (WI), Nash-Sutcliffe efficiency (NSE) and the most stringent metrics of Legate-McCabe's index (LM). These evaluation statistics are presented after aggregating the initial results of the four seasons with averages so that extensive comparative outcomes could be delivered at multiple forecasting timescales. The observed trends in aggregated and non-aggregated statistics were very similar. In Fig. 7, the comparisons of WI, NSE and LM aided by line graphs reveal that the W-O-convLSTM model performs significantly better than other predictive models. The objective model achieved the highest WI and NSE with WI = 0.962 and NSE = 0.864 at 10M, WI = 0.960 and NSE = 0.851 at 20M, WI = 0.946 and NSE = 0.801 at 30M and WI = 0.940 and NSE = 0.780 at 60M forecast horizons. Verification of the performance measure using LM consolidates superior performance by the hybrid W-O-convLSTM model, as it yields lowest stringent errors and highest LM statistics, where LM = 0.713 at 10M, LM = 0.706 at 20M, LM = 0.627 at 30M and LM = 0.609 at 10M forecast horizons. Again, the model performance drops with increasing forecast timescales.

In conjunction with the statistical metrics, the percentage errors, such as RRMSE and RMAE were further employed as alternative score metrics to enable the model comparison during the four different seasons. For instance, the seasonal-based performance comparison of the proposed W-O-convLSTM model against the counterparts are presented using radar plots in Fig. 8 at 10M forecast horizon. The objective model captured the lowest RRMSE and RMAE

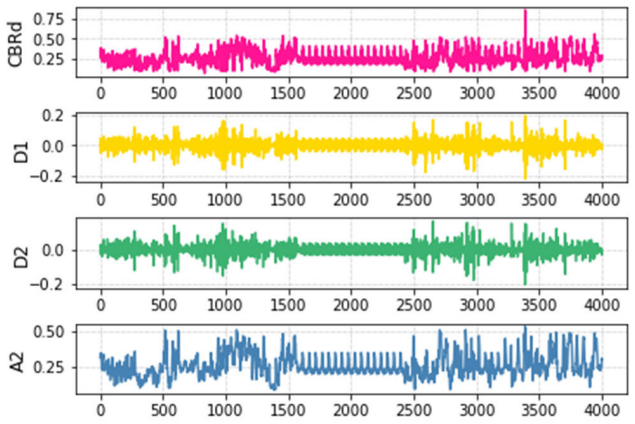

FIGURE 6. SWT decomposed detailed coefficients (D1 and D2) and approximation coefficient (A2) of CBR_d (predictor input) in the training period for summer-based 10 minutes forecast horizon.

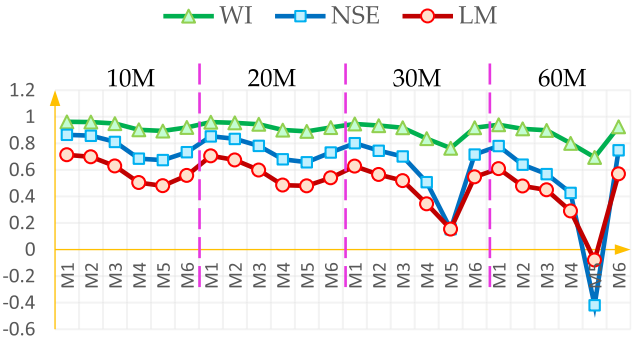

FIGURE 7. Line graphs of seasonal aggregated Legate-McCabe's Index (LM), Willmott's Index (WI) and Nash-Sutcliffe Efficiency (NSE) for W-O-convLSTM model (M1) against its comparatives (M2 – M6) during the testing phase.

values with RRMSE = 18.226% and RMAE = 28.426% in autumn, RRMSE = 26.324% and RMAE = 19.318% in winter, RRMSE = 17.697% and RMAE = 18.936% in spring and RRMSE = 17.173% and RMAE = 16.224% in summer. By displaying relatively better performance with respect to the comparative models in all four seasons, our newly designed model is highly competent for delivering more accurate forecasts of UVI at 10M forecast horizon. Similar performance was achieved by the objective model at all the other forecast horizons.

A DM test was implemented to compare the forecasting performance of the objective model with its counterparts. The null hypothesis (H_O) was set as: the observed differences between the performances of two forecasting models are not significant. H_O was tested against the alternative hypothesis (H_A), which was set as: the observed differences between the performances of two forecasting models are significant. By conducting this statistical test at a 5% level of significance, we rejected H_O if $|DM| > 1.96$. The outcomes of DM tests are presented in Table 6 for 10M horizon, where the calculated

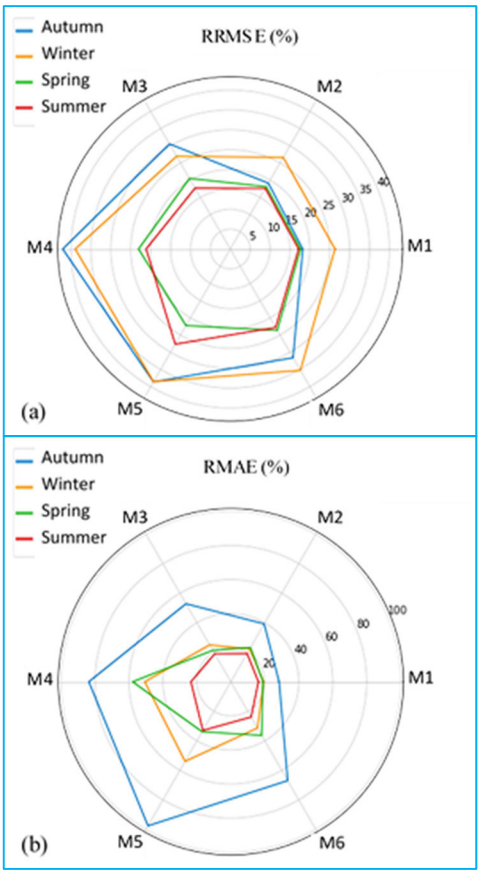

FIGURE 8. Radar plots showing the seasonal-based testing phase performance for W-O-convLSTM model (M1) against its comparatives (M2 – M6) measured by: (a) Relative Root Mean Square Error (RRMSE %) and (b) Relative Mean Absolute Error (RMAE %) at 10M forecast horizon.

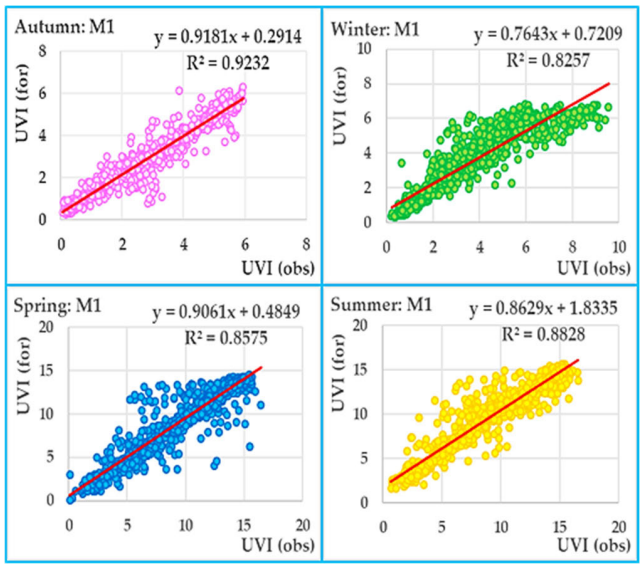

FIGURE 9. Scatterplots of the observed and forecasted UVI data in the testing phase with the optimal W-O-convLSTM model (M1) for 10M forecast horizon. Equations of linear regression and the coefficient of determination (R^2) are shown in each panel.

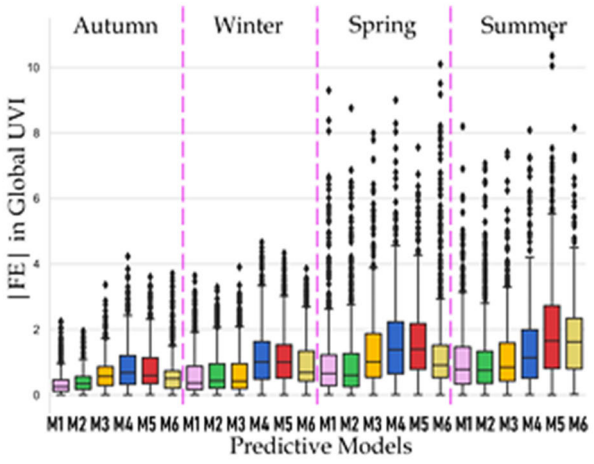

FIGURE 10. Boxplots of the absolute forecasted error |FE| in the seasonal-based testing datasets of UVI at 10M forecast horizon for W-O-convLSTM model relative to its counterparts.

DM statistics are mostly greater than 1.96 and less than -1.96. In accordance with these statistics, we conclude that the difference in UVI forecasts from the two predictive models is statistically significant in most cases (H_O is rejected). The test implies that our W-O-convLSTM model mostly shows greater accuracies. The only exceptions are for comparisons of our objective model with O-convLSTM (M2) in spring and summer, where the DM statistics are -0.359 and 0.161, respectively. Possibly due to stochastic interference, the observed differences between the performances of these two forecast models are not significant and they capture the same accuracies. Otherwise, in most cases, our proposed model delivers superior performance. Similar outcomes of DM tests were yielded for other forecast horizons.

To further examine the success of the W-O-convLSTM model in UVI forecasting, the observed and forecasted values were plotted as ordinate and abscissa (for the objective model) in Fig. 9 and as the absolute forecasted error (for all predictive models) in Fig. 10 for 10M horizon. The scatterplots presented in Fig. 9 display a least squares regression line ($UVI^{for} = mUVI^{obs} + c$, where c is the ordinate intercept and m is the gradient) between the observed and forecasted UVI. For an optimal performing model, its R^2 value is closer to 1, while the m and c values are very close to 1 and 0, respectively [58]. In our case, the W-O-convLSTM model performs very well in all seasons, having the most efficient performance in autumn with $R^2 = 0.923$, $m = 0.918$ and forecasts with robust adaptability to seasonal and diurnal variations, particularly for stochastic cloud cover conditions. As enumerated in Fig. 10, the boxplots of absolute forecasted error |FE| (i.e. $|FE| = UVI^{for} - UVI^{obs}$) explore the precision of the W-O-convLSTM model against comparative models in terms of statistics of the lower quartile, upper quartile, median, maximum, minimum and data outliers. Upon comparisons, the boxplots justify that the distributed errors for the objective model acquire significantly lower statistical error

TABLE 6. Outcomes of Diebold-Mariano (DM) tests to compare the forecast accuracy of W-O-convLSTM Model (M1) against the competing counterparts at 10M Forecast Horizon.

Season	DM Test	M1 vs. M2	M1 vs. M3	M1 vs. M4	M1 vs. M5	M1 vs. M6
Autumn	DM Statistic	-4.388	-14.358	-17.130	-18.091	-12.311
	p Value	0.000	0.000	0.000	0.000	0.000
	H_O	Reject	Reject	Reject	Reject	Reject
Winter	DM Statistic	-2.655	-2.399	-17.977	-19.068	-15.870
	p Value	0.008	0.016	0.000	0.000	0.000
	H_O	Reject	Reject	Reject	Reject	Reject
Spring	DM Statistic	-0.359	-9.672	-14.050	-13.437	-6.893
	p Value	0.719	0.000	0.000	0.000	0.000
	H_O	Accept	Reject	Reject	Reject	Reject
Summer	DM Statistic	0.161	-2.609	-7.857	-15.206	-16.303
	p Value	0.872	0.009	0.000	0.000	0.000
	H_O	Accept	Reject	Reject	Reject	Reject

criteria with smaller spread and relatively lower magnitude of quartile and median statistics. Due to the reason that the designed models did not achieve a correlation coefficient of 1, some outliers were observed in |FE|. Mostly in summer and spring, the designed models could not capture all higher variability in cloud type, ozone column and aerosol effects (i.e. dust and smoke). Despite the presence of some outliers in |FE|, the proposed W-O-convLSTM model yielded high values of r, (mostly greater than 0.9) in all four seasons and at all the forecast timescales, as indicated in Table 5.

The newly designed W-O-convLSTM model yielded high correlation coefficients (r values) in UVI forecasting. The high r values were achieved because the predictor inputs displayed a high correlation with the UVI. The study by [60] revealed that there is a high correlation between the monthly average SZA and UVI (≈88% or 0.88). Similarly, in our study, Table 1 shows a high r value of 0.89 between 10 minutes SZA and UVI. Together with SZA, we further integrated cloud statistical properties that were also correlated with UVI to generate UVI forecasts. Having highly correlated features with the target, the simulations of UVI forecasts in this study yielded high r values. Another similar study by [61] integrated SZA and cloud statistical properties with a CNN-LSTM model to forecast photosynthetic photon flux density (PPFD). The outcomes revealed that the model captured a high r value of 0.92 in generating forecasts of PPFD. Moreover, our study forecasted very short-term UVI at 10M, 20M, 30M and 60M. For a very short-term forecast, there would be a high correlation of immediate past value with the current value, and a high correlation of current value with future value. To further justify the high r values captured by the objective model we calculated Murphy's skill score (SS). The work of [62] reveals that the derived decompositions of SS yield analytical relationships between the respective skill scores and the coefficient of correlation between the observations and forecasts. Table 7 presents the SS of the W-O-convLSTM model in generating UVI forecasts at multi-step horizons for the four seasons. High values of SS validate high r values captured in UVI forecasts.

TABLE 7. Skill score (SS) of the W-O-convLSTM model at Multi-Step Forecast Horizon.

Forecast Horizon	Skill Score			
	Autumn	Winter	Spring	Summer
10M	0.922	0.816	0.847	0.870
20M	0.917	0.796	0.828	0.871
30M	0.820	0.748	0.789	0.848
60M	0.841	0.721	0.714	0.846

Overall, the evaluation outcomes and results exemplified in Table 5-6, as well as in Fig. 7-10 demonstrate the robustness and efficacy of the newly proposed W-O-convLSTM model in generating cloud-affected UVI forecasts with respect to its counterpart models at multi-step timescale. It was essential to apply several statistical criteria, as a single indicator may not portray the shortcomings of each predictive model [63]. After exploring the performance against benchmarked and baseline models, the findings reveal that our wavelet-based hybrid W-O-convLSTM captures comparatively larger values of r, WI and ENS, smaller values of MAE and RMSE, lower percentage errors of RRMSE and RMAE and better values of R^2, m and c. The superiority of W-O-convLSTM is further elucidated by larger values of the most stringent metric, i.e. LM. In terms of the forecast timescales, more accurate and efficient forecasts of cloud-affected UVI are achieved at a lower forecast horizon (10M). The stochastic nature of the cloud is best captured on short time scales, as even the slightest position change can vastly change the available UV. While our objective model presents the most precise performance by having lower |FE|, it demonstrates its forecasting adaptability for all four seasons in Queensland. Out of the four seasons, the aforementioned performance metrics statistics indicate that our wavelet-hybridized model

generates the best forecasts in autumn and delivers slightly lower performance in winter at all the forecasting timescales. However, such observed discrepancy is subtle and relative to other counterpart models, the proposed W-O-convLSTM model still delivers the best forecasting skills for all four seasons. The robustness of our SWT-based objective model over the non-SWT-based benchmarked models is an outcome of exploiting SWT that successfully addressed the issues of non-stationarity in the cloud statistical properties prior to simulating UVI forecasts.

To validate the influence of cloud movements on UVI, our cloud properties-based W-O-convLSTM model is gauged against the SZA-based W-O-convLSTMsza model (baseline model developed with a single predictor input of SZA). In accordance with the captured results in Table 5-6 and Fig. 7-10, the objective model displays superior performance over the baseline model, thus affirming the significance of stochastic cloud effects on ground level UVR.

In this study, the development of a multiple input multi-step output W-O-convLSTM model entails many advantages. Firstly, after rigorous evaluation using robust statistical metrics, the model displays superior and enhanced performance in forecasting short-term UVI for Australia. Secondly, the enhancement in simulations of future UVI can serve as a powerful clinical tool to inform more accurate sun-protection times to the public and mitigate skin and eye health risks under different cloud cover conditions. Moreover, our improved image segmentation technique avers its potential applicability in modeling UVI with cloud cover conditions for other temperate countries. Our image segmentation techniques may also be applicable in designing robust predictive models to improve solar radiation forecasts. This may benefit the energy sector for solar energy monitoring under cloud-affected skies. Additionally, such cloud segmentation techniques can be integrated into modeling photosynthetic active radiation to facilitate healthy plant growth and benefit the agricultural sector. Despite an excellent performance by the newly proposed W-O-convLSTM model, it exhibits a minor limitation. In model designing, we did not use the aerosol and ozone datasets, as these were not available for our site at 10 minutes time resolution. These are two important atmospheric variables that also affect the ground-based UVI through the absorption and scattering processes. However, in our study, we utilized the time-lagged Bentham UVI datasets that already captured some ozone and aerosol effects. For future studies, integrating ozone and aerosol datasets may further improve the UVI forecasting framework.

VI. CONCLUSION

We proposed a novel solar UVI forecasting framework by building a hybrid deep learning and multi-step input system, denoted as W-O-convLSTM model, integrating antecedent lagged memory of cloud cover properties with SZA. The newly developed model was further validated with data extracted for four different seasons at study sites in Queensland, Australia where solar UV radiation currently poses a serious risk in terms of increasing skin cancer and eye diseases such as Pterygium, cataracts, or other eye health ailments. A 3-phase model design approach was employed, which entailed an input selection process with BorutaShap, data decomposition using the SWT and a hyperparameter optimization stage with the Optuna algorithm. We performed a holistic evaluation of the predictive model through statistical metrics and diagnostic plots of predicted and measured UVI to elucidate the superior forecasting skill of the proposed W-O-convLSTM model over its benchmark models. For the forecast horizon of 10 minutes (10M), 20 minutes (20M), half-hourly (30M) and hourly (60M) scales we noted an accurate performance of the proposed W-O-convLSTM model that has also captured the stochastic effects of cloud cover. Thus, our newly proposed model is a likely tool to be adopted in real life for benefits to the public health area such as delivering sun protection behavior recommendations that can help mitigate skin cancer and eye disease risk.

Our study, advancing an earlier work [7] that has used solar zenith angle as a single input to predict the solar UV index, was a next stage pioneering research in developing an artificial intelligence-based predictive model particularly by integrating cloud cover conditions. However, in a future study, we may integrate the actual measured values of aerosol and ozone effects together with the solar zenith angle and the cloud cover effects to further enhance the predictive framework for real-time UVI forecasting.

ACKNOWLEDGMENT

The datasets were collected at the University of Southern Queensland (USQ), Toowoomba Campus experimental facility. The authors sincerely acknowledge all expert reviewers whose comments have improved the final article.

REFERENCES

[1] J. S. Paula, F. Thorn, and A. A. V. Cruz, "Prevalence of pterygium and cataract in indigenous populations of the Brazilian Amazon rain forest," *Eye*, vol. 20, no. 5, pp. 533–536, May 2006.

[2] C. M. Olsen, L. F. Wilson, A. C. Green, C. J. Bain, L. Fritschi, R. E. Neale, and D. C. Whiteman, "Cancers in Australia attributable to exposure to solar ultraviolet radiation and prevented by regular sunscreen use," *Austral. New Zealand J. Public Health*, vol. 39, no. 5, pp. 471–476, Oct. 2015.

[3] A. L. White and L. S. Jahnke, "Contrasting effects of UV-A and UV-B on photosynthesis and photoprotection of β-carotene in two *Dunaliella spp*," *Plant Cell Physiol.*, vol. 43, no. 8, pp. 877–884, 2002.

[4] B. L. Diffey, "Solar ultraviolet radiation effects on biological systems," *Phys. Med. Biol.*, vol. 36, no. 3, pp. 299–328, Mar. 1991.

[5] (2002). World Health Organization, World Meteorological Organization, United Nations Environment Programme, and International Commission on Non-Ionizing Radiation Protection. *Global Solar UV Index: A Practical Guide*. World Health Organization, Geneva, Switzerland. Accessed: Aug. 2, 2021. [Online]. Available: https://apps.who.int/iris/bitstream/handle/10665/42459/9241590076.pdf

[6] M. Allaart, M. van Weele, P. Fortuin, and H. Kelder, "An empirical model to predict the UV-index based on solar zenith angles and total ozone," *Meteorol. Appl.*, vol. 11, no. 1, pp. 59–65, Mar. 2004.

[7] R. C. Deo, N. Downs, A. V. Parisi, J. F. Adamowski, and J. M. Quilty, "Very short-term reactive forecasting of the solar ultraviolet index using an extreme learning machine integrated with the solar zenith angle," *Environ. Res.*, vol. 155, pp. 141–166, May 2017.

[8] M. J. Sneyd and B. Cox, "A comparison of trends in melanoma mortality in New Zealand and Australia: The two countries with the highest melanoma incidence and mortality in the world," *BMC Cancer*, vol. 13, no. 1, pp. 1–9, Dec. 2013.

[9] B. Dexter, R. King, A. Parisi, S. Harrison, D. Konovalov, and N. Downs, "Keratinocyte skin cancer risks for working school teachers: Scenarios and implications of the timing of scheduled duty periods in Queensland, Australia," *J. Photochem. Photobiol. B, Biol.*, vol. 213, Dec. 2020, Art. no. 112046.

[10] N. Pandeya, C. M. Olsen, and D. C. Whiteman, "The incidence and multiplicity rates of keratinocyte cancers in Australia," *Med. J. Aust.*, vol. 207, no. 8, pp. 339–343, Oct. 2017.

[11] T. Koskela, A. Heikkilä, J. Kaurola, A. Lindfors, A. Tanskanen, and P. D. Outer, "Spectral solar UV monitoring: worth it?" *Proc. SPIE*, vol. 6362, Oct. 2006, Art. no. 63622A.

[12] G. H. Bernhard, R. E. Neale, and P. W. Barnes, "Environmental effects of stratospheric ozone depletion, UV radiation and interactions with climate change: UNEP environmental effects assessment panel, update 2019," *Photochem. Photobiol. Sci.*, vol. 19, no. 5, pp. 542–584, 2020.

[13] J. M. Sabburg and A. V. Parisi, "Spectral dependency of cloud enhanced UV irradiance," *Atmos. Res.*, vol. 81, no. 3, pp. 206–214, Sep. 2006.

[14] S. Ghimire, R. C. Deo, N. Raj, and J. Mi, "Deep learning neural networks trained with MODIS satellite-derived predictors for long-term global solar radiation prediction," *Energies*, vol. 12, no. 12, p. 2407, 2019.

[15] J. N. Latosińska, M. Latosińska, and J. Bielak, "Towards modelling ultraviolet index in global scale. Artificial neural networks approach," *Aerosp. Sci. Technol.*, vol. 41, pp. 189–198, Feb. 2015.

[16] J. F. Puerta Barrera, D. Amaya Hurtado, and R. Jiménez Moreno, "Prediction system of erythemas for phototypes I and II, using deep-learning," *Revista Vitae*, vol. 22, no. 3, pp. 189–196, May 2015.

[17] P. Oliveira, B. Fernandes, C. Analide, and P. Novais, "Multi-step ultraviolet index forecasting using long short-term memory networks," in *Proc. Int. Symp. Distrib. Comput. Artif. Intell.*, L'Aquila, Italy, 2020, pp. 187–197.

[18] P. Arora, H. Kumar, and B. K. Panigrahi, "Prediction and analysis of COVID-19 positive cases using deep learning models: A descriptive case study of India," *Chaos, Solitons Fractals*, vol. 139, Oct. 2020, Art. no. 110017.

[19] S. Ghimire, R. C. Deo, N. Raj, and J. Mi, "Deep solar radiation forecasting with convolutional neural network and long short-term memory network algorithms," *Appl. Energy*, vol. 253, Nov. 2019, Art. no. 113541.

[20] M. Moishin, R. C. Deo, R. Prasad, N. Raj, and S. Abdulla, "Designing deep-based learning flood forecast model with ConvLSTM hybrid algorithm," *IEEE Access*, vol. 9, pp. 50982–50993, 2021.

[21] D. Niu, L. Diao, L. Xu, Z. Zang, X. Chen, and S. Liang, "Precipitation forecast based on multi-channel ConvLSTM and 3D-CNN," in *Proc. Int. Conf. Unmanned Aircr. Syst. (ICUAS)*, Athens, Greece, Sep. 2020, pp. 367–371.

[22] Y. Geurkink, J. Boone, S. Verstockt, and J. G. Bourgois, "Machine learning-based identification of the strongest predictive variables of winning and losing in Belgian professional soccer," *Appl. Sci.*, vol. 11, no. 5, p. 2378, 2021.

[23] M. R. M. Yusof, A. K. Ariffin, and M. Ismail, "Wavelet denoising as signal feature-dependent kernel convolution," in *Proc. Int. Conf. Res. Learn. Phys.*, Padang, Indonesia, 2019, pp. 1–10.

[24] L. E. Bouny, M. Khalil, and A. Adib, "ECG heartbeat classification based on multi-scale wavelet convolutional neural networks," in *Proc. IEEE Int. Conf. Acoust., Speech Signal Process. (ICASSP)*, Barcelona, Spain, May 2020, pp. 3212–3216.

[25] S. W. Lee and H. Y. Kim, "Stock market forecasting with super-high dimensional time-series data using ConvLSTM, trend sampling, and specialized data augmentation," *Expert Syst. Appl.*, vol. 161, Dec. 2020, Art. no. 113704.

[26] S. Xingjian, Z. Chen, H. Wang, D.-Y. Yeung, W.-K. Wong, and W.-C. Woo, "Convolutional LSTM network: A machine learning approach for precipitation nowcasting," in *Proc. Adv. Neural Inf. Process. Syst. (NIPS)*, Montreal, QC, Canada, 2015, pp. 802–810.

[27] B. Li, B. Tang, L. Deng, and M. Zhao, "Self-attention ConvLSTM and its application in RUL prediction of rolling bearings," *IEEE Trans. Instrum. Meas.*, vol. 70, pp. 1–11, 2021.

[28] G. Chitalia, M. Pipattanasomporn, V. Garg, and S. Rahman, "Robust short-term electrical load forecasting framework for commercial buildings using deep recurrent neural networks," *Appl. Energy*, vol. 278, Nov. 2020, Art. no. 115410.

[29] T.-T. Tran, J.-W. Choi, T.-T. H. Le, and J.-W. Kim, "A comparative study of deep CNN in forecasting and classifying the macronutrient deficiencies on development of tomato plant," *Appl. Sci.*, vol. 9, no. 8, p. 1601, 2019.

[30] S. Ghimire, R. C. Deo, N. Raj, and J. Mi, "Wavelet-based 3-phase hybrid SVR model trained with satellite-derived predictors, particle swarm optimization and maximum overlap discrete wavelet transform for solar radiation prediction," *Renew. Sustain. Energy Rev.*, vol. 113, Oct. 2019, Art. no. 109247.

[31] Z. Tian, "Prediction of information dissemination based on passive-aggressive algorithm," in *Proc. 5th Int. Conf. Comput. Eng. Netw.-PoS(CENet)*, Shanghai, China, Oct. 2015, pp. 1–8.

[32] Á. Peiró-Signes, M. Segarra-Oña, Óscar Trull-Domínguez, and J. Sánchez-Planelles, "Exposing the ideal combination of endogenous–exogenous drivers for companies' ecoinnovative orientation: Results from machine-learning methods," *Socio-Econ. Planning Sci.*, vol. 79, Feb. 2022, Art. no. 101145, doi: 10.1016/j.seps.2021.101145.

[33] M. J. Kleiman, E. Barenholtz, and J. E. Galvin, "Screening for early-stage Alzheimer's disease using optimized feature sets and machine learning," *J. Alzheimer's Disease*, vol. 81, no. 1, pp. 355–366, 2021, doi: 10.3233/JAD-201377.

[34] J.-H. Hur, S.-Y. Ihm, and Y.-H. Park, "A variable impacts measurement in random forest for mobile cloud computing," *Wireless Commun. Mobile Comput.*, vol. 2017, Sep. 2017, Art. no. 6817627.

[35] C. Strobl, A.-L. Boulesteix, T. Kneib, T. Augustin, and A. Zeileis, "Conditional variable importance for random forests," *BMC Bioinform.*, vol. 9, no. 307, pp. 1–11, 2008.

[36] L. Yao, Z. Leng, J. Jiang, and F. Ni, "Modelling of pavement performance evolution considering uncertainty and interpretability: A machine learning based framework," *Int. J. Pavement Eng.*, pp. 1–16, Nov. 2021, doi: 10.1080/10298436.2021.2001814.

[37] D. Štifanić, J. Musulin, A. Miočević, S. Baressi Šegota, R. Šubić, and Z. Car, "Impact of COVID-19 on forecasting stock prices: An integration of stationary wavelet transform and bidirectional long short-term memory," *Complexity*, vol. 2020, Jul. 2020, Art. no. 1846926.

[38] U. K. Rajput, R. Kumar, and G. Kumar, "Comparison between discrete wavelet transform and the stationary wavelet transform based techniques for the fusion of multi-focus images," *Emerg. Trends Electron. Commun.*, vol. 1, no. 2, pp. 202–208, 2015.

[39] R. C. Deo, X. Wen, and F. Qi, "A wavelet-coupled support vector machine model for forecasting global incident solar radiation using limited meteorological dataset," *Appl. Energy*, vol. 168, pp. 568–593, Apr. 2016.

[40] S. N. S. Sayed Daud and R. Sudirman, "Decomposition level comparison of stationary wavelet transform filter for visual task electroencephalogram," *J. Teknologi*, vol. 74, no. 6, pp. 7–13, May 2015.

[41] W. G. Morsi and M. E. El-Hawary, "A new perspective for the IEEE standard 1459-2000 via stationary wavelet transform in the presence of nonstationary power quality disturbance," *IEEE Trans. Power Del.*, vol. 23, no. 4, pp. 2356–2365, Oct. 2008.

[42] T. Akiba, S. Sano, T. Yanase, T. Ohta, and M. Koyama, "Optuna: A next-generation hyperparameter optimization framework," in *Proc. 25th ACM SIGKDD Int. Conf. Knowl. Discovery Data Mining*, Anchorage, AK, USA, 2019, pp. 2623–2631.

[43] S. Garg and P. Pundir, "MOFit: A framework to reduce obesity using machine learning and IoT," in *Proc. 44th Int. Conv. Inf., Commun. Electron. Technol. (MIPRO)*, Opatija, Croatia, Sep. 2021, pp. 1733–1740.

[44] S. Gao, J. Xu, W. Dan, Q. Li, and Y. Huang, "Research on optimal control of fractional order $PI^{\lambda}D^{\mu}$ parameters of SCR denitrification system," in *Proc. 3rd Int. Conf. Ind. Artif. Intell. (IAI)*, Shenyang, China, Nov. 2021, pp. 1–6.

[45] I. Ekundayo, "Optuna optimization-based CNN-LSTM networks for predicting energy consumption," M.S. thesis, School Comput., Nat. College Ireland, Dublin, Ireland, 2020.

[46] I. F. J. Badosa, "UV index measurement and model agreement: Uncertainties and limitations," Ph.D. dissertation, Itinerari de Física i Tecnologia Ambiental, Universitat de Girona, Girona, Spain, 2005.

[47] A. V. Parisi, N. Downs, J. Turner, and A. Amar, "Online educative activities for solar ultraviolet radiation based on measurements of cloud amount and solar exposures," *J. Photochem. Photobiol. B, Biol.*, vol. 162, pp. 434–440, Sep. 2016.

[48] D. P. Igoe, A. V. Parisi, and N. J. Downs, "Cloud segmentation property extraction from total sky image repositories using Python," *Instrum. Sci. Technol.*, vol. 47, no. 5, pp. 522–534, Sep. 2019.

[49] R. Chauvin, J. Nou, S. Thil, A. Traoré, and S. Grieu, "Cloud detection methodology based on a sky-imaging system," *Energy Proc.*, vol. 69, pp. 1970–1980, May 2015.
[50] W. Richardson, H. Krishnaswami, R. Vega, and M. Cervantes, "A low cost, edge computing, all-sky imager for cloud tracking and intra-hour irradiance forecasting," *Sustainability*, vol. 9, no. 4, p. 482, 2017.
[51] F. O. Odhiambo, "Comparative study of various methods of handling missing data," *Math. Model. Appl.*, vol. 5, no. 2, pp. 87–93, 2020.
[52] F. Pedregosa, G. Varoquaux, and A. Gramfort, "Scikit-learn: Machine learning in Python," *J. Mach. Learn. Res.*, vol. 12 no. 10, pp. 2825–2830, 2012.
[53] M. Abadi, P. Barham, J. Chen, Z. Chen, and A. Davis, "Tensorflow: A system for large-scale machine learning," in *Proc. 12th USENIX Symp. Operating Syst. Design Implement.*, Savannah, GA, USA, 2016, pp. 265–283.
[54] N. Ketkar, "Introduction to Keras," in *Deep Learning With Python*. Berkeley, CA, USA: Apress, 2017, pp. 97–111.
[55] E. Sharma, R. C. Deo, R. Prasad, A. V. Parisi, and N. Raj, "Deep air quality forecasts: Suspended particulate matter modeling with convolutional neural and long short-term memory networks," *IEEE Access*, vol. 8, pp. 209503–209516, 2020.
[56] A. A. M. Ahmed, R. C. Deo, N. Raj, A. Ghahramani, Q. Feng, Z. Yin, and L. Yang, "Deep learning forecasts of soil moisture: Convolutional neural network and gated recurrent unit models coupled with satellite-derived MODIS, observations and synoptic-scale climate index data," *Remote Sens.*, vol. 13, no. 4, p. 554, Feb. 2021.
[57] R. C. Deo, M. K. Tiwari, J. F. Adamowski, and J. M. Quilty, "Forecasting effective drought index using a wavelet extreme learning machine (W-ELM) model," *Stochastic Environ. Res. Risk Assessment*, vol. 31, no. 5, pp. 1211–1240, Jul. 2017.
[58] M. S. Al-Musaylh, R. C. Deo, and Y. Li, "Electrical energy demand forecasting model development and evaluation with maximum overlap discrete wavelet transform-online sequential extreme learning machines algorithms," *Energies*, vol. 13, no. 9, p. 2307, 2020.
[59] F. Diebold and R. Mariano, "Comparing predictive accuracy," *J. Bus. Econ. Statist.*, vol. 20, no. 1, pp. 134–144, 1995.
[60] H. Farouk, R. H. Hamid, H. K. Elminir, and A. Abulwfa, "Ground-based measurements of UV index (UVI) at helwan," *NRIAG J. Astron. Geophys.*, vol. 1, no. 2, pp. 159–164, Dec. 2012.
[61] R. C. Deo, R. H. Grant, A. Webb, S. Ghimire, D. P. Igoe, N. J. Downs, M. S. Al-Musaylh, A. V. Parisi, and J. Soar, "Forecasting photosynthetic photon flux density under cloud effects: Novel predictive model using convolutional neural network integrated with long short-term memory network," *Stochastic Environ. Res. Risk Assessment*, pp. 1–52, Nov. 2021, doi: 10.21203/rs.3.rs-1069113/v1.
[62] A. H. Murphy, "Skill scores based on the mean square error and their relationships to the correlation coefficient," *Monthly Weather Rev.*, vol. 116, no. 12, pp. 2417–2424, Dec. 1988.
[63] M. S. Al-Musaylh, R. C. Deo, and Y. Li, "Electrical energy demand forecasting model development and evaluation with maximum overlap discrete wavelet transform-online sequential extreme learning machines algorithms," *Energies*, vol. 13, no. 9, p. 2307, May 2020.

SALVIN S. PRASAD received the B.Sc. degree in physics and mathematics and the M.Sc. degree in physics from the University of the South Pacific, Fiji. He is currently pursuing the Ph.D. degree with the Advanced Data Analytics Laboratory, School of Mathematics, Physics and Computing, University of Southern Queensland, Australia. His research interests include artificial intelligence (machine learning and deep learning), data analytics, solar UV radiation, environmental sciences, and renewable energy systems.

RAVINESH C. DEO (Senior Member, IEEE) leads the Advanced Data Analytics Laboratory as a Professor with the University of Southern Queensland, Australia. He is a Clarivate Highly Cited Researcher with publications ranking in top 1% by citations for field and publication year in the Web of Science citation index and is among scientists and social scientists who have demonstrated significant broad influence, reflected in the publication of multiple papers frequently cited by their peers. He leads cross-disciplinary research in deep learning and artificial intelligence, supervising 20+ Ph.D./M.Sc. degrees. He has received Employee Excellence Awards, Elsevier Highly Cited Paper Awards, and Publication Excellence and Teaching Commendations. He has published more than 235 articles, 150 journals, and seven books in Elsevier, Springer, and IGI with 23 book chapters. He has cumulative citations that exceed 8,700 with an H-index of 51.

NATHAN DOWNS is an Associate Professor with the School of Sciences, University of Southern Queensland, Australia, where he is actively involved in the quantification of personal solar ultraviolet exposure through the use of smartphone technologies, assessing occupational exposure risks in global population groups, and the measurement of spectral radiation during extreme aerosol events. His research interests include photobiology, atmospherics, and skin cancer epidemiology.

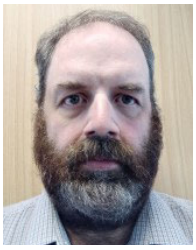

DAMIEN IGOE is an Adjunct Lecturer with the School of Sciences, University of Southern Queensland, Australia. He is an experienced Teacher in science and mathematics. His research interests include the development of methods to measure solar ultraviolet radiation, particularly using smartphone technology, urban air quality, data analysis and modeling, and STEM education.

ALFIO V. PARISI is a Physicist and an Honorary Professor with the School of Sciences, University of Southern Queensland, Australia. His research interests include the development of techniques in solar ultraviolet (UV) dosimetry, radiometry, and spectroradiometry, including the development of new methods for solar measurement applied to provide improved characterization of the solar UV environment, and measurement of solar exposures to plants.

JEFFREY SOAR came to academic research from a long and distinguished career in industry including as a Chief Information Officer in government agencies in Australia and New Zealand. He is the Personal Chair of Human-Centered Technology with the School of Business, University of Southern Queensland. His research interests include AI, e-business, e-health, technology and development, and social and organizational change.

4.3. **Links and implications**

The newly developed hybrid DL system, denoted as the W-O-convLSTM model integrated antecedent lagged memory of cloud statistical properties and SZA to generate more precise UVI forecasts at multi-step horizons. The applicability of the prescribed model is highly suitable for the regions around Toowoomba as the model was trained on the time-lagged Bentham UVI datasets that already captured some ozone and aerosol effects for this study site. However, the predictive performance may slightly decrease for other distant geographical locations as the proposed model did not train on the site-specific aerosol and ozone datasets due to their unavailability at 10-minute time resolution for Toowoomba. It is known that to some extent, the ground-level UVI is influenced by the absorption and scattering processes led by aerosol and ozone effects (Deo et al. 2017).

To overcome the influence of aerosol and ozone effects in modelling, it is more practical to forecast the UV-A component of the ground-level UV radiation by training the predictive model on the available cloud statistical properties. The forecasts of UV radiation generated in terms of UVI are depicted as the combined effects of UV-A and UV-B wavebands. Among the two, the absorption and scattering effects of the stratospheric ozone are negligible on the UV-A component (Kudish et al. 2005). Additionally, the incident UV-A radiation at the Toowoomba experimental site is much less affected by aerosols as the study area is located approximately 100 km inland relative to the ocean and experiences limited aerosol and anthropogenic effects (Deo et al. 2017). So, without the aerosol and ozone datasets, it is essential to construct a UV-A forecasting model by integrating the available 10-minute cloud statistical properties extracted from the sky images and SZA datasets. Due to the reasons that aerosol and ozone effects exhibit much less influence on UV-A radiation, the UV-A forecasting model developed for the Toowoomba hotspot can further extend its practical utility at other geographical locations, particularly for most remote areas.

The design of a UV-A radiation predictive model has not been examined extensively in the literature, though it poses detrimental exposure effects on the people, and the terrestrial animal and plant life on earth. So far, some previous studies have been conducted in exploring models for predicting UV-B radiation as this waveband is known to cause premature ageing and skin cancer in humans and animals (Sterenborg & VanDerLeun 1987; Zhao & He 2022). On the same notion, UV-A radiation is highly abundant and its harmful exposure is also linked to greater risks

of skin cancer because high doses of the UV-A waveband can penetrate much deeper into the skin tissues to cause severe biological damage (Lavker et al. 1995). It is known that 95% of the UV waveband is represented by the UV-A component, which is much greater than the UV-B component (Courdavault et al. 2004). In plant cells, exposure to harmful UV-A wavelengths escalates photosynthetic damage as it minimizes the electron transport efficiency and enhances radical formations (White & Jahnke 2002). When compared with the UV-B waveband, the UV-A component can easily transmit through glass (Parisi et al. 2007). In this scenario, the glass-transmitted UV-A rays pose harmful exposure risks for people participating in recreational activities or those at work. Therefore, the detrimental UV-A exposure effects on people and terrestrial environments also need adequate monitoring and exploration. By designing robust decision support tools using an AI-inspired predictive framework, more accurate and reliable UV-A exposure risk information can be provided to the end-users, including the general public and UV radiation researchers.

Additionally, the predictive performance and reliability of the AI-based DL systems can be further improved through model calibration. In this regard, the predictive model can be calibrated by adopting the uncertainty quantification approach that requires an ensemble of several single-point models trained on different key loss functions (Stevenson et al. 2022). On this notion, the first objective designed a UVI forecasting model but the model calibration strategy was not applied. Thus, a UV-A forecasting data-intelligent framework can be constructed by integrating a model calibration and uncertainty quantification approach with a robust DL algorithm to further explore the predictive performance and model reliability.

CHAPTER 5: PAPER 2 – VERY SHORT-TERM SOLAR ULTRAVIOLET-A RADIATION FORECASTING SYSTEM WITH CLOUD COVER IMAGES AND A BAYESIAN OPTIMIZED INTERPRETABLE ARTIFICIAL INTELLIGENCE MODEL

5.1. Introduction

This chapter is an exact copy of the published article in *Expert Systems with Applications* journal, Vol. 236, Page 121273 (2023) (Scopus Impact Factor 8.665).

The chapter describes the construction of a hybrid UV-A forecasting model at a 20-minute horizon. The vital stages of developing the hybrid ensemble N-BEATS model are illustrated in the schematic structure in Figure 5. In the first stage, the cross-correlations of the input predictors with UV-A radiation were assessed and the most significant time-lagged predictor inputs were selected. The N-BEATS base model was hybridized by applying a NCA algorithm for feature selection and a Bayesian optimizer for hyperparameter tuning. Further hybridization was achieved by developing an ensemble of 15 single-point models trained on three different key loss functions. To attain enhanced performance capability, the model was calibrated by carrying out uncertainty quantification. To explore the intermittent cloud cover effects on ground-level UV-A, the proposed model was trained on the cloud statistical properties extracted from sky images, along with SZA. These input datasets were only available for the Toowoomba experimental site at a desired time resolution, and due to this reason, the Toowoomba hotspot was only explored for constructing the UV-A forecasting model. Though this study site, which has been selected for objective 2 was the same as that in objective 1, the length of datasets and the target variables were different for both objectives. Moreover, objective 2 adopts a remarkable modelling strategy by implementing the concept of model calibration and uncertainty quantification. The newly designed hybrid ensemble model, designated as B-E-NBEATS was rigorously assessed for its forecasting performance alongside four other competing counterpart models, where one of them was a hybrid ensemble model (B-E-LSTM) and the other three were non-ensemble-based models (B-NBEATS, B-LSTM and B-BRR).

The results of the rigorous evaluation with robust statistical score metrics show that the proposed B-E-NBEATS model outperforms all the other benchmarked models in forecasting near-real-time UV-A. The model also offers seasonality and trend as interpretable outputs for the observed and predicted UV-A. Through model calibration, the stochastic effects of the cloud cover conditions on the forecasting performance are reduced and a better version of uncertainty estimations and model reliability was obtained. The robust forecasting skill of the newly developed data-intelligent model with interpretable outcomes affirms its practical applications in providing more accurate UV-A radiation information for the end-users and researchers to help mitigate the UV-exposure-related detrimental effects on people and terrestrial animal and plant life.

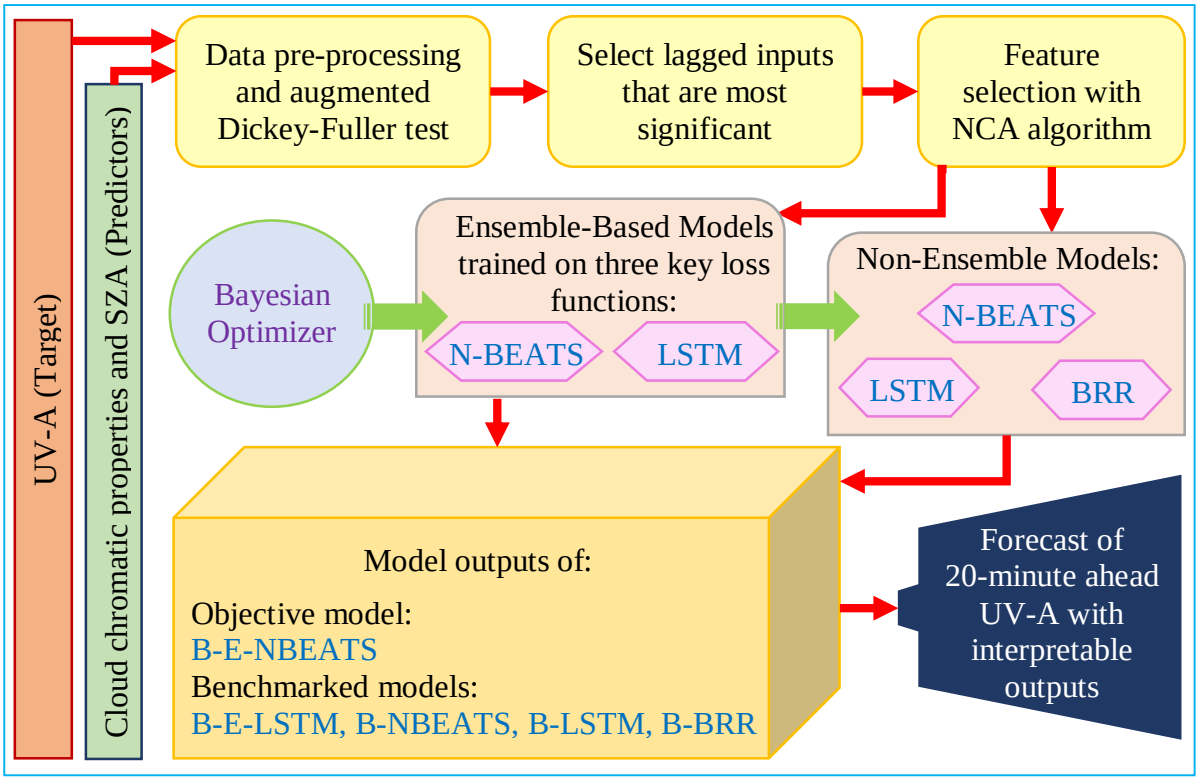

Figure 5 Schematic structure of the prescribed UV-A forecasting framework with cloud cover images using a hybrid ensemble N-BEATS model (B-E-NBEATS).

5.2. **Published paper**

5.3. **Links and implications**

A hybrid ensemble DL predictive framework, denoted as B-E-NBEATS model constructed to achieve objective 2 of this PhD research robustly demonstrates its performance superiority in forecasting short-term UV-A with interpretable outputs. In regards to the architecture of the DL models, these are “black-box” with highly complex and non-explainable hidden internal workings (Vilone & Longo 2021). Some recent studies have applied the xAI architecture to better understand the DL “black-box” generated outcomes (Joseph et al. 2022; Van der Velden et al. 2022). The model-agnostic xAI tools generate explainable and interpretable outcomes that make the DL models transparent and more trustworthy for respective end-users and decision-makers (Vilone & Longo 2021). These model-agnostic tools are capable of explaining the DL models locally using the LIME method (Zdravković et al. 2022) and globally using the SHAP and PFI approaches (Qin et al. 2022). For the purpose of forecasting UV radiation with explainable outcomes, there appears to be a significant gap in the literature, as the xAI architectures have not been integrated previously in modelling UVI. Thus, it is important that the model-agnostic xAI tools are applied to the DL UVI forecasting framework so that the feature interactions and the predictive behaviour of this “black-box” system is clearly explained.

In objectives 1 and 2, cloud cover effects were applied as input predictors for establishing the UVI and UV-A radiation predictive models, respectively using the sky image-based cloud statistical properties extracted from the Toowoomba experimental sites. However, it is important that other geographical sites are also explored to validate the merits of a DL-based UV radiation forecasting model. Some other Australian hotspots having high UV radiation exposure include Darwin, Alice Springs, Townsville and Emerald and these regions have not been explored for designing an explainable UVI forecasting framework in previous research. Unfortunately, the sky images are not available for these sites, so the satellite-derived predictor variables, including cloud cover effects, can be implemented to establish a UVI forecasting framework integrated with the xAI tools. Among the satellite-derived products, the cloud cover conditions, atmospheric aerosol column, ozone effects, dust concentrations and water vapour content are highly interconnected with the solar UV radiation and it is vital that these atmospheric variables are applied in modelling UVI.

The short-term UVI forecasting model constructed using the satellite-derived atmospheric variables and SZA can be implemented as an early warning decision support tool for the Australian hotspots that receive high UV exposure. In particular, the DL UVI forecasting model trained on several important atmospheric variables can be applicable to many different sites and other temperate countries, including most remote locations. Through integrating the UVI predictive model with the xAI tools, the influence of respective predictor variables on the model outcome can be explained locally and globally to further aid the end-users and UV researchers in better decision-making. In this respect, the design of a DL xAI framework tailored for short-term forecasting of UVI can provide more accurate and explainable sun-protection behaviour recommendations to the general public and help mitigate UV-exposure-related eye and skin diseases, including skin cancers.

CHAPTER 6: PAPER 3 – ENHANCED JOINT HYBRID DEEP NEURAL NETWORK EXPLAINABLE ARTIFICIAL INTELLIGENCE MODEL FOR 1-HR AHEAD SOLAR ULTRAVIOLET INDEX PREDICTION MODEL

6.1. Introduction

This chapter is an exact copy of the published article in *Computer Methods and Programs in Biomedicine* journal, Vol. 241, Page 107737 (2023) (Scopus Impact Factor 7.027).

The chapter describes the development of a joint hybrid explainable model for forecasting hourly ahead UVI using a DNN as a base model. It explores the influence of satellite-derived atmospheric variables, such as cloud cover conditions, atmospheric aerosol column, ozone effects, dust concentrations and water vapour content on ground-level UV radiation using xAI tools. Along with these predictors, SZA is also utilized as an input in modelling UVI for the four Australia hotspots of Darwin, Alice Springs, Townsville and Emerald.

The schematic diagram presented in Figure 6 describes the important phases in designing the proposed enhanced joint hybrid explainable DNN model. It entails the selection of the most significant time-lagged inputs by assessing the CCF in terms of r_{cross} and PACF. Consequently, the DNN model was hybridized by applying model-specific and filter-based algorithms for dual-phase feature selection, a Bayesian optimizer algorithm for hyperparameter optimization and the xAI-based model-agnostic tools for providing model explanations. To affirm the model transparency and trustworthiness, the local and global explainable outcomes of this “black-box” model were extracted using the LIME, SHAP and PFI algorithms. The proposed enhanced joint hybrid explainable model, designated as EJH-X-DNN was stringently evaluated against six skilful comparative models (EJH-FCN, EJH-ANN, EJH-MLP, EJH-AB, EJH-SGD and EJH-DT) using a plethora of performance metrics for forecasting the UVI.

Model evaluation outcomes indicate that the prescribed EJH-X-DNN framework demonstrates optimal performance in forecasting short-term UVI. The combined xAI-based explainable outcomes of the local and global model-agnostic approaches reveal that the major contributing predictor variables in forecasting short-term UVI were the antecedent lagged memory of UVI (at a lag of t – 1) and SZA. The feature attributes

associated with cloud cover conditions, ozone effects and precipitation also showed some significant impact on model predictions. The performance superiority and trustworthiness of this explainable forecasting system avers its practicality as an early warning tool for UV exposure through an online or mobile mode for most temperate countries, including remote locations. The explainable forecasted outcomes of UVI can aid the expert end-users as a decision support tool to provide more accurate sun protection information and help mitigate the deleterious UV radiation exposure effects that can cause skin diseases (including skin cancers) and eye health ailments.

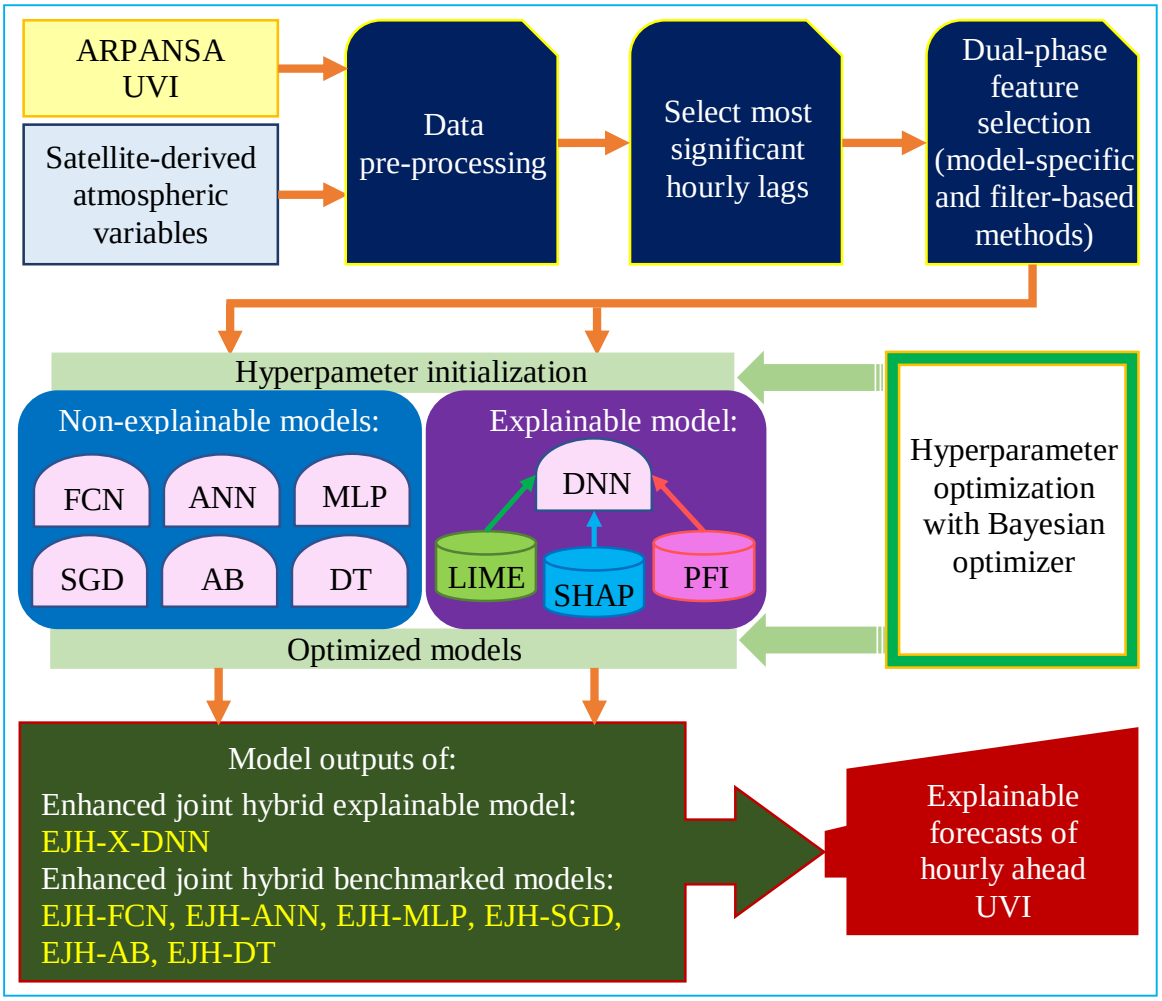

Figure 6 Schematic diagram of the proposed enhanced joint hybrid explainable UVI forecasting framework (EJH-X-DNN) integrated with satellite-derived predictors.

6.2. **Published paper**

Computer Methods and Programs in Biomedicine 241 (2023) 107737

Contents lists available at ScienceDirect

Computer Methods and Programs in Biomedicine

journal homepage: www.elsevier.com/locate/cmpb

Enhanced joint hybrid deep neural network explainable artificial intelligence model for 1-hr ahead solar ultraviolet index prediction

Salvin S. Prasad [a], Ravinesh C. Deo [a,*], Sancho Salcedo-Sanz [a,c], Nathan J. Downs [b], David Casillas-Pérez [d], Alfio V. Parisi [b]

[a] School of Mathematics, Physics and Computing, University of Southern Queensland, Springfield, QLD 4300, Australia
[b] School of Mathematics, Physics and Computing, University of Southern Queensland, Toowoomba, QLD 4350, Australia
[c] Department of Signal Processing and Communications, Universidad de Alcalá, Alcalá de Henares, 28805, Madrid, Spain
[d] Department of Signal Processing and Communications, Universidad Rey Juan Carlos, Fuenlabrada, 28942, Madrid, Spain

ARTICLE INFO

MSC:
0000
1111

Keywords:
Ultraviolet index
Explainable artificial intelligence (xAI)
Model-agnostic
Black-box models
Deep neural networks
Bayesian optimization

ABSTRACT

Background and Objective: Exposure to solar ultraviolet (UV) radiation can cause malignant keratinocyte cancer and eye disease. Developing a user-friendly, portable, real-time solar UV alert system especially or wearable electronic mobile devices can help reduce the exposure to UV as a key measure for personal and occupational management of the UV risks. This research aims to design artificial intelligence-inspired early warning tool tailored for short-term forecasting of UV index (*UVI*) integrating satellite-derived and ground-based predictors for Australian hotspots receiving high UV exposures. The study further improves the trustworthiness of the newly designed tool using an explainable artificial intelligence approach.

Methods: An enhanced joint hybrid explainable deep neural network model (called EJH-X-DNN) is constructed involving two phases of feature selection and hyperparameter tuning using Bayesian optimization. A comprehensive assessment of EJH-X- DNN is conducted with six other competing benchmarked models. The proposed model is explained locally and globally using robust model-agnostic explainable artificial intelligence frameworks such as Local Interpretable Model-Agnostic Explanations (LIME), Shapley additive explanations (SHAP), and permutation feature importance (PFI).

Results: The newly proposed model outperformed all benchmarked models for forecasting hourly horizons *UVI*, with correlation coefficients of 0.900, 0.960, 0.897, and 0.913, respectively, for Darwin, Alice Springs, Townsville, and Emerald hotspots. According to the combined local and global explainable model outcomes, the site-based results indicate that antecedent lagged memory of *UVI* and solar zenith angle are influential features. Predictions made by EJH-X-DNN model are strongly influenced by factors such as ozone effect, cloud conditions, and precipitation.

Conclusion: With its superiority and skillful interpretation, the *UVI* prediction system reaffirms its benefits for providing real-time UV alerts to mitigate risks of skin and eye health complications, reducing healthcare costs and contributing to outdoor exposure policy.

1. Introduction

Exposure to solar ultraviolet (UV) radiation (290-400 nm) poses both beneficial and harmful effects on people, as well as terrestrial animal and plant life. In terms of benefits, exposure to UV radiation enables the human body to produce a sufficient amount of vitamin D that helps strengthen muscles, bones and the overall immune system [1]. The ability of UV radiation to inactivate potentially harmful micro-organisms (such as protozoa) has led to its application as a disinfectant in the water and food industry [2]. Recently, UV light was increasingly utilized as a significant disinfectant for coronavirus-contaminated surfaces during the COVID-19 pandemic [3]. Contrary to the benefits, elevated exposure to UV light radiation causes temporary or irreversible damage to the process of photosynthesis in plants [4]. Above all, the most pressing

* Corresponding author.
E-mail addresses: salvin.prasad@usq.edu.au (S.S. Prasad), ravinesh.deo@usq.edu.au (R.C. Deo), sancho.salcedo@uah.es (S. Salcedo-Sanz), nathan.downs@usq.edu.au (N.J. Downs), david.casillas@urjc.es (D. Casillas-Pérez), alfio.parisi@usq.edu.au (A.V. Parisi).

https://doi.org/10.1016/j.cmpb.2023.107737
Received 1 June 2023; Received in revised form 16 July 2023; Accepted 27 July 2023
Available online 5 August 2023

concern for the health sector is the detrimental effects of erythemally-effective UV irradiance at the short end of the spectrum (290 to 315 nm) that poses high exposure risks for human skin and eyes [5,6]. Prolonged UV exposure may result in skin-based malignant keratinocyte cancers and eye diseases that include cataracts and pterygium [7].

UV radiation-induced skin cancers have led to an increased mortality rate in most temperate countries. In 2018, there was a significant mortality of 126,000 for skin cancer on a global basis, which imposes a profound economic burden on healthcare services [8]. Having a high ambient UV irradiance and prevalence of fair skin types in the Australian and New Zealand population, the two countries recorded the highest incidence of melanoma and keratinocyte carcinoma on a global basis in 2021 [9]. In Australia, such skin-related public health problems are more severe and they impose a huge burden on the Australian health sector with an annual estimated expenditure of $1.7 billion (AUD) on skin cancer treatment [10].

In order to develop engineering-based solutions for wearable electronics and other personal protection tools that can implement sun protection and mitigate the impacts of sun-exposure-related skin and eye health risks, the World Health Organization (WHO), International Commission on Non-Ionizing Radiation Protection (ICNIRP), World Meteorological Organization (WMO) and United Nations Environment Programme (UNEP) have developed the global solar UV index (*UVI*). This is a numeric-scale indicator of the public health risk of UV, ranging from 0 to 11^{+} [11]. With a high *UVI*, the associated UV exposure severity and potential damage to the skin and eye is expected to rise. Preventative interventions with innovative decision support tools capable of providing sun exposure information to individuals can help mitigate the detrimental effects of UV exposure, as well as reduce healthcare costs. For some decades, ground-based [5] and satellite-based [6] instrumentations have been commonly employed to estimate the incoming solar UV irradiance. Though the two approaches can deliver accurate sun-exposure information, the major drawback of their practical utility is the high costs of installation, maintenance and operation [12].

Predictive frameworks designed through the application of artificial intelligence (AI) modeling can pragmatically deliver more accurate forecasts of UV exposure metrics that are adaptable to changing physical conditions in the atmosphere and useful to users of mobile technology. Machine learning (ML) and deep learning (DL) algorithms are widely used AI-based forecasting systems that are cost-effective, robust and user-friendly for time-dependent forecasting [13]. Recent studies reveal that the DL technology is gaining more prominence in its application, particularly in the *UVI* forecasting framework where simulations of *UVI* forecasts have captured high predictive accuracy [14,15]. However, the DL models have a black-box architecture with hidden internal workings that are highly complex and non-explainable. To better understand the DL black-box-generated outcomes, most recent studies have utilized explainable artificial intelligence (xAI) architecture [16,17]. The xAI architectures enable the DL models to become transparent, as the outcomes are interpretable and more trustworthy for the end users and decision-makers [16]. A plethora of innovative research methodologies has applied the model-agnostic tools in the xAI domain that include the local and global model explainability. At the local level, the local interpretable model-agnostic explanations (LIME) technique robustly explains the individual prediction of the black-box model [18]. In regards to global explanations, the Shapley additive explanations (SHAP) and permutation feature importance (PFI) frameworks are capable of explaining the entire decision of the black-box predictive model [19]. The applications of xAI technique further allow the layperson to clarify the logic underlying the process of decision-making by a black-box model. Currently, there appears to be a significant gap in the literature on integrating xAI in modeling *UVI*, as no previous studies have applied the xAI architecture in the *UVI* forecasting framework.

This paper focuses on designing an xAI-based enhanced *UVI* forecasting system using DL technology to offer local and global explainability regarding the influence of the predictor variables on model outcomes. Solar zenith angle (SZA) is one important attribute that influences the level of solar UV radiation on the earth's surface. This variable is known to govern the optical path length while the incident radiation traverses through the earth's atmosphere [5]. At any given SZA, the unbroken cloud cover condition is another meteorological variable that significantly reduces the solar *UVI* by 50 to 60% and even more during precipitation [20]. However, the scattering of solar irradiation by partial intermittent cloud cover can cause an escalated spike in ground-level UV radiation, thus exceeding the nominal cloud-free surface UV radiation [5]. In this scenario, the general public can be subjected to more severe UV exposure, which poses even greater damaging effects on the skin and eyes. Aerosols are another important atmospheric variable that impacts the surface-level *UVI* [15]. Furthermore, the *UVI* is also affected by absorption and scattering due to stratospheric ozone [21].

The objective of the current study is to design an enhanced joint hybrid explainable deep neural network (DNN) to deliver more accurate short-term forecasts of solar *UVI* using satellite-derived variables (including SZA as a ground-based variable) and the partial autocorrelation function (PACF) of the *UVI* data generated at the most significant lags. Our model is an enhanced joint hybrid (EJH) for the reason that a dual-phase feature selection is carried out, followed by an application of Bayesian optimization to enhance the model performance. A remarkable xAI framework (denoted as X) is further utilized to offer local and global model explanations.

Thus, this objective model is denoted as EJH-X-DNN. The primary contributions of this paper are summarized as follows:

- A robust DL architecture, known as DNN is proposed and applied to a *UVI* forecasting domain using satellite-derived and ground-based datasets for four Australian hotspots (Darwin, Alice Springs, Townsville and Emerald) with high solar UV radiation.
- Dual-phase feature selection is employed for dimensionality reduction. In the first phase, the informative attributes are selected using model-specific feature importance by integrating random forest (RF) as the base model. In the second phase, the redundant predictors are identified and eliminated with respect to high correlation (r).
- Further enhancement of the predictive performance is achieved through efficient tuning of the model hyperparameters using a Bayesian optimizer (BO).
- Model-agnostic xAI is applied to interpret the predictive behavior of the model, where LIME is used to explain the model outcomes at the local level, while SHAP and PFI are used for explanations at the global level.
- The accurate and interpretable forecasts of short-term *UVI* by the predictive framework can facilitate the end-users to deliver more precise sun protection behavior recommendations to the general public and mitigate UV-exposure-related skin and eye health risks.

The remainder of the paper is organized as follows: Section 2 reviews the background and related literature; Section 3 discusses the theoretical overview of the focused concepts; Section 4 describes the different methods adopted in designing an explainable *UVI* forecasting system; Section 5 presents the results and deliberates related discussions; Section 6 discourses the concluding remarks of this study and future research directions.

2. Related works

Conventional mechanistic methods with instruments such as spectroradiometers and radiometers have been commonly utilized by most health sectors to extract UV exposure information and deliver timely sun protection advice to the general public [22]. However, the real-time application of these devices can be constrained by the high costs of equipment, installation, calibration and maintenance [5]. With such flaws and the issue of accessibility for most remote locations, an alter-

native deterministic method has been applied in developing the *UVI* forecasting framework. Though the deterministic approach seems to be promising, limitations caused by the use of estimated and assumed fixed initial conditions continue to affect the overall prediction accuracy [5,23].

The advent of AI-inspired expert predictive systems can robustly address the drawbacks of mechanistic and deterministic methods, particularly in forecasting solar *UVI*. The AI-based ML and DL forecasting platforms are known to exhibit immense computational efficiency and these algorithms are highly skillful in handling the non-linearity in input datasets [14]. The potential of the ML technique has been explored by [24] in forecasting long-term *UVI* on a global scale using a feed-forward multi-layered artificial neural network (ANN). Additionally, an extreme learning machine integrated with SZA was applied by [5] to forecast short-term *UVI* for a study site in Toowoomba, Australia. However, other studies have opted to employ DL technology over the ML approach, as the former employs a non-linear model of multiple hidden layer architecture that enables the framework to learn the complex relationship between outputs and inputs [25]. The ML technique also entails some overfitting issues [26]. In a recent work, three days ahead *UVI* was forecasted in a global context by exploiting a DL long short-term memory (LSTM) network [27]. Similarly, the daily *UVI* was forecasted for the state of Western Australia using a hybrid DL convolution long short-term memory (CNN-LSTM) network [14]. In another study, a wavelet hybrid convolutional LSTM (convLSTM) network was integrated with sky images and SZA in forecasting multi-step *UVI* for a Toowoomba-based study site in Australia [15].

In terms of model interpretability, none of the aforementioned predictive systems have applied xAI to extract model-agnostic local and global explanations that are instrumental in understanding the influences of different attributes on *UVI* predictions. Some relevance may be drawn from a recent study where an xAI-inspired model-agnostic SHAP and PFI explainers were integrated with a RF model to offer global interpretations based on interactions of the feature variables in predicting solar radiation [28]. Another similar research applied the LIME model-agnostic tool to extract local explanations for heat demand forecasting using different configurations of the LSTM networks [18]. SHAP explanation technique was also integrated with LSTM networks to analyze the global influence of input variables on energy consumption forecasting [29]. A recent survey highlighted that the SHAP explainer displays powerful performance in generating global post-hoc explanations based on the input perturbations using DNN [30].

The model-agnostic LIME, SHAP and PFI explainers have their separate strengths and shortcomings. The LIME technique is highly effective in delivering local post-hoc explanations by exploiting surrogate interpretable and reliable representations that best approximate the reference predictive model [31]. In comparison with SHAP, LIME is faster in execution as the latter algorithm generates instance-based interpretations [32]. On the positive side, the SHAP method efficiently offers explanations for the entire decision of the reference model at a global level. Although the SHAP tool can elegantly offer global explanations, the execution time of the algorithm is a bit high [17]. Keeping in mind the benefits of LIME and SHAP explainers, most researchers have opted to implement these methods simultaneously to extract more rigorous and faithful black-box model interpretations both at local and global levels for better decision-making [16,17]. Furthermore, PFI is another remarkable algorithm that provides black-box model explanations at the global level. However, like the SHAP tool, the PFI method also takes a slightly higher execution time to generate effective model explainability [33].

As mentioned earlier, a knowledge gap has been identified as the model-agnostic xAI architectures are not yet integrated with any DL black-box model to offer local and global explanations. Henceforth, the current study advocates a more comprehensive combination of LIME, SHAP and PFI explainers to provide model transparency, as well as to overcome any embedded biases of the *UVI* simulating black-box model for better decision-making. Through xAI decision support tools, more reliable and credible sun-exposure behavior recommendations can be delivered to the public in the risk zone.

3. Methodology

In this study, the design phase of DL hybrid explainable *UVI* forecasting framework entails multiple modeling stages. The flowchart presented in Fig. 1 summarizes the significant stages affiliated with the modeling of *UVI* forecasts. In accordance with the flow chart summary, the first stage involves retrieval of satellite-derived and ground-based predictors plus the target variable for the four Australian hotspots with high UV radiation exposure. The second stage involves pre-processing and imputation of extracted datasets. In the third stage, the cross-correlation and partial auto-correlation of the features and the label are determined at the most significant hourly lag. The fourth stage entails dual-phase feature selection, where the first phase involves an application of a model-specific feature selection technique with RF and in the second phase the redundant features are eliminated on the basis of having higher r. In stage five, a DL hybrid explainable EJH-X-DNN model is designed and benchmarked with competing counterparts to forecast hourly ahead *UVI*. A BO is further applied to fine-tune the model hyperparameters. To assess the performance of the proposed EJH-X-DNN model against the benchmarked models, robust statistical score metrics are used. In the final stage, we exploit xAI-based model-agnostic tools (LIME, SHAP and PFI) to offer local and global explanations based on the black-box EJH-X-DNN model predictions.

Hereafter, the sub-sections provide a detailed methodology of the aforementioned stages involved in constructing the DL hybrid explainable *UVI* forecasting system.

3.1. Study site and data extraction

To establish and validate the merits of the proposed hybrid explainable EJH-X-DNN model in generating hourly forecasts of *UVI*, four Australian hotspots that are at high risk of harmful exposure to solar UV radiation are selected.

Table 1 shows the geographical description of the study sites and the inferential statistics of *UVI*. Two of these study sites are Darwin and Alice Springs from the Northern Territory (NT) while the other two are Townsville and Emerald from the State of Queensland (QLD). These hotspots are known to be subtropical regions that receive a large number of sunshine hours on an annual basis [5]. The health sector within these hotspots is significantly burdened by UV-exposure-related impacts on skin and eye health. Table 1 (a) details the geographical description of the four selected research hotspots.

In constructing the proposed model pipeline to forecast hourly horizon *UVI*, the first stage involves data extraction. The Australian Radiation Protection and Nuclear Safety Agency (ARPANSA) provided the ground data for the target variable *UVI*, which has been accessed from https://www.arpansa.gov.au and for all four Australian hotspots. Considering that one unit of *UVI* is equivalent to 25 $\mathrm{mW\,m^{-2}}$ of erythemally effective irradiance [20,5], *UVI* is mathematically represented as:

$$UVI = \frac{1}{25\ \mathrm{mW\,m^{-2}}} \int_{290}^{400} S(\lambda) \cdot E_{UV}(\lambda) \cdot d\lambda, \tag{1}$$

where E_{UV} is the spectral energy in $\mathrm{W\,m^{-2}\,nm^{-1}}$ measured over the terrestrial wavelengths of 290 to 400 nm, and $S(\lambda)$ is the relative erythema effectiveness at each discrete wavelength. To ensure cost-effectiveness and accurate procedure, the ARPANSA data is closely monitored by regular data assessment and quality checks. For each selected site, Table 1 (b) presents the inferential statistics of ARPANSA-sourced *UVI* in terms of mean, standard deviation, median, maximum value, minimum value, skewness and kurtosis. All the statistical descriptions are very significant. For instance, the *UVI* values showing low kurtosis indicate

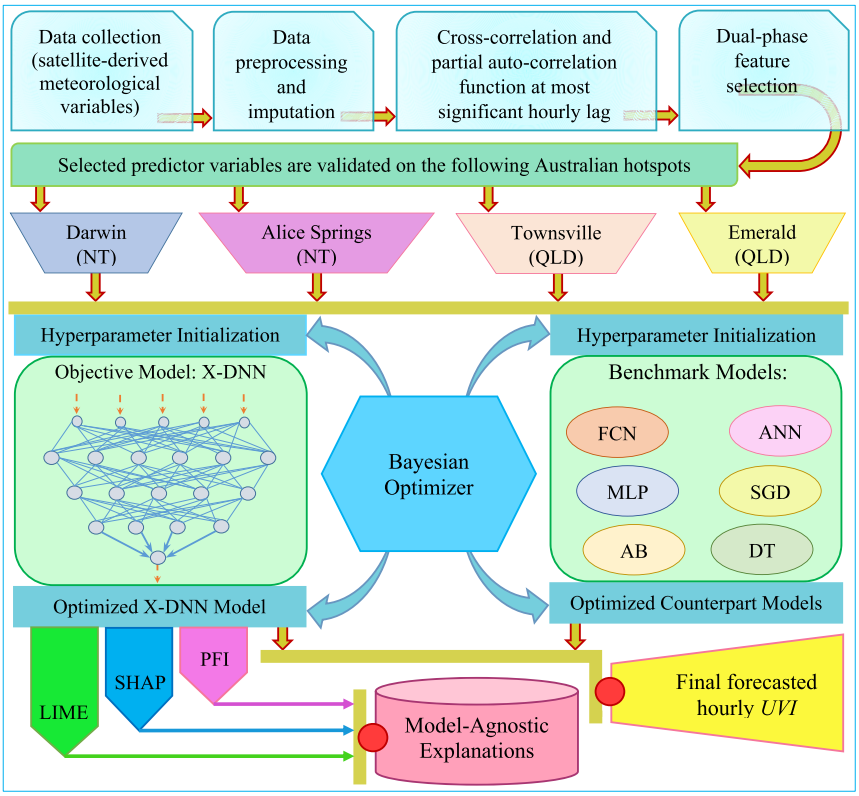

Fig. 1. Flowchart highlighting the major stages in the design phase of proposed hybrid EJH-X-DNN model for generating hourly ahead forecasts of *UVI* with model-agnostic explanations.

Table 1
(a) The geographical description of the study sites, (b) Inferential statistics of *UVI*.

(a) Site Name, State		Location		
		Latitude (°E)	Longitude (°E)	Elevation (m)
Darwin, NT		12.43	130.89	28
Alice Springs, NT		23.80	133.89	576
Townsville, QLD		23.53	148.16	15
Emerald, QLD		19.33	146.76	189

(b) Target Variable	Location	Mean	St. Dev.	Median	Max.	Min.	Skewness	Kurtosis
UVI	Darwin	4.99	3.72	4.45	16.63	0.01	0.53	-0.62
	Alice Springs	4.72	3.67	3.97	16.72	0.01	0.71	-0.45
	Townsville	4.69	3.57	3.89	16.65	0.03	0.80	-0.17
	Emerald	4.50	3.45	3.86	16.20	0.01	0.78	-0.20

that the datasets are light-tailed relative to a normal distribution. Having light-tailed distribution implies a lack of outliers in the overall *UVI* dataset.

In selecting the model inputs, satellite-derived predictors have been sourced from the National Aeronautics and Space Administration (NASA) database, particularly the Goddard Online Interactive Visualization and Analysis Infrastructure (GIOVANNI) geoscience data repository from https://giovanni.gsfc.nasa.gov/giovanni/. GIOVANNI acquires data for over 2000 satellite variables, for which it eminently provides online-based visualizations and analytical platforms [34]. Due to the inadequacy of ground-based datasets, most meteorological problems have been alternatively addressed using satellite-based remote sensing data [35].

For the purpose of this study, we preferably adopted the satellite-derived products captured by the Modern-Era Retrospective Analysis for Research and Applications (MERRA) satellite to simulate forecasts of hourly horizon *UVI*. Considering that the variations in incident UV radiation are significantly interconnected with cloud cover conditions, ozone effects, atmospheric aerosol column, dust concentrations and content of water vapor [5,36], eight relative predictor variables were extracted from the MERRA satellite for fusion with the proposed DL *UVI* simulating framework.

Additionally, the ground-based SZA that is known to highly affect the intensity of solar UV-radiation was acquired by integrating a deterministic Pro6UV method [5]. Table 2 details the eight MERRA-derived predictors and the ground-based SZA with corresponding acronyms, data extraction source, units, instrument/model for data acquisition and spatial resolution in degrees.

To construct the hybrid explainable EJH-X-DNN model, two years of datasets for the aforementioned ground-based and satellite-derived meteorological variables were extracted from 1st January 2020 to 31st December 2021, as indicated in Table 3. These datasets were extracted at a time resolution of 1 hour from 7.30 am to 4.30 pm on a daily basis. After having extracted these important meteorological parameters, the *UVI* (target input) and the nine predictors (feature inputs) datasets were ready for further preprocessing toward modeling *UVI*.

Table 2
Description of the input features (ground-based and satellite-derived) used to construct the proposed hybrid explainable EJH-X-DNN model.

Attribute Name	Acronym	Source	Units	Instrument/Model	Spatial Resolution
Solar zenith angle	SZA	Ground	°	Pro6UV	-
Cloud area fraction for high clouds	CAFHC	MERRA-2	-	M2T1NXRAD v5.12.4	0.5°×0.625°
Cloud area fraction for middle clouds	CAFMC	MERRA-2	-	M2T1NXRAD v5.12.4	0.5°×0.625°
Cloud area fraction for low clouds	CAFLC	MERRA-2	-	M2T1NXRAD v5.12.4	0.5°×0.625°
Total aerosol angstrom parameter	TAAP	MERRA-2	-	M2T1NXAER v5.12.4	0.5°×0.625°
Total aerosol scattering AOT	TAS	MERRA-2	-	M2T1NXAER v5.12.4	0.5°×0.625°
Dust scattering AOT	DS	MERRA-2	-	M2T1NXADG v5.12.4	0.5°×0.625°
Total column ozone	TCO	MERRA-2	Dobsons	M2T1NXSLV v5.12.4	0.5°×0.625°
Total precipitable water vapor	TPWV	MERRA-2	$kg\,m^{-2}$	M2T1NXSLV v5.12.4	0.5°×0.625°

Table 3
Site-based segregation of input datasets into training, validation and testing during the model design phase.

Sites	Period	Data Points	Training Points (≈80%)	Validation Points	Testing Points (≈20%)
Darwin	01-Jan-2020 to 31-Dec-2021	7265	5815		1450
Alice Springs	01-Jan-2020 to 31-Dec-2021	7267	5815	10% of	1452
Townsville	01-Jan-2020 to 31-Dec-2021	7276	5817	Training	1459
Emerald	01-Jan-2020 to 31-Dec-2021	7273	5815		1458

3.2. Data preprocessing

The second stage of *UVI* modeling for the four sites in Australia entails data preprocessing. It was important to carefully scrutinize the extracted datasets to locate any missing data. There were very few instances when some datasets were missing and these were duly recovered by imputing with the monthly median of the respective variable at the same daily time domain. For this study, the median imputation technique among the three imputation methods of mean, median and listwise deletion was adopted. Imputation using the median approach is robust and generates more accurate imputed values in comparison with the mean and listwise deletion methods [37]. Once the complete sets of data were obtained through imputation, the stationarity in these datasets was further tested by applying the augmented Dickey-Fuller Test [38]. The test outcome disclosed that all the input datasets were stationary for the four hotspots.

In the third stage, the cross-correlation coefficient (r_{cross}) and partial autocorrelation function (PACF) were assessed with the aid of correlogram plots to obtain time-lagged inputs at the most significant lag for modeling *UVI*. For instance, Fig. 2 (a) illustrates the r_{cross} plots to investigate the co-variances between *UVI* and feature variables for the Darwin hotspot. A 95% confidence band was used as a reference where the lags of any variable within this boundary were considered insignificant. After evaluating r_{cross} of each feature with *UVI*, the most significant historically preceding values of the predictor variables were selected as inputs to construct the proposed hourly ahead *UVI* forecasting system for all four sites.

Fig. 2 (b) presents the PACF plot of the *UVI* time series that displays the antecedent behavior in terms of hourly lags of *UVI* for the Darwin hotspot. After analyzing the PACF of *UVI* time series, the four most significant antecedent lagged *UVI* were considered as model inputs. For the purpose of this study, the four antecedent lags of *UVI* at t - 1, t - 2, t - 3 and t - 4 are denoted as PACF1, PACF2, PACF3 and PACF4, respectively, where t represents real-time. The time-lagged inputs for the other three sites of Alice Springs, Townsville and Emerald were also extracted via assessment of r_{cross} and PACF in a similar manner. Thereafter, a historical lagged matrix was created for the ground-based and satellite-derived predictors at a lag of (t - 1) as inputs toward feature selection for each site.

3.3. Feature selection

The fourth stage of model building involves dual-phase feature selection of the ground and satellite-acquired predictor variables. In the first phase, a wrapper-based model-specific approach was exploited to select the most pertinent attributes. The feature datasets were first subjected to a base ML model to search the space of all possible subsets of the feature inputs in terms of their importance. In this study, a RF model is applied as the base ML model to fit the attribute datasets and assess all possible combinations with respect to the evaluation criterion in selecting the most informative features. After evaluation, the base model ranked the input predictor variables in accordance with their overall importance to the model.

Fig. 3 shows the model-specific feature importance generated by the base model for the four selected sites. With respect to the displayed ranked attributes, the base model has considered SZA as the most pertinent feature with the highest importance score for each selected site. The criterion was to eliminate any inapt predictor variable that captures zero feature importance scores. As per the feature selection outcomes described in Fig. 3, it is observed that none of the attributes within the feature space yielded zero feature importance scores for all four sites. Consequently, all the features were considered important using the model-specific feature selection approach.

Having none of the attributes eliminated from the feature set in the first phase, the study adopted a second phase of filter-based feature selection by assessing the degree of correlation between the attributes within the feature space. The correlations among the nine predictor variables of the four sites are described with an aid of a color-coded heatmap in Fig. 4.

The criterion was to drop one of the attributes having a high correlation, preferably $r > 0.8$ or $r < -0.8$ for this study. Any two predictor variables displaying high correlation become redundant as they contribute very similar information towards model training and eliminating one of them improves the computational efficiency. In conformity with Fig. 4, none of the features were observed to be redundant for all four sites. No two attributes among the feature space captured high correlations as per the selection criteria and for this reason, all the features were considered pertinent inputs for the model construction phase. Together with the selected feature variables, the four historical lagged

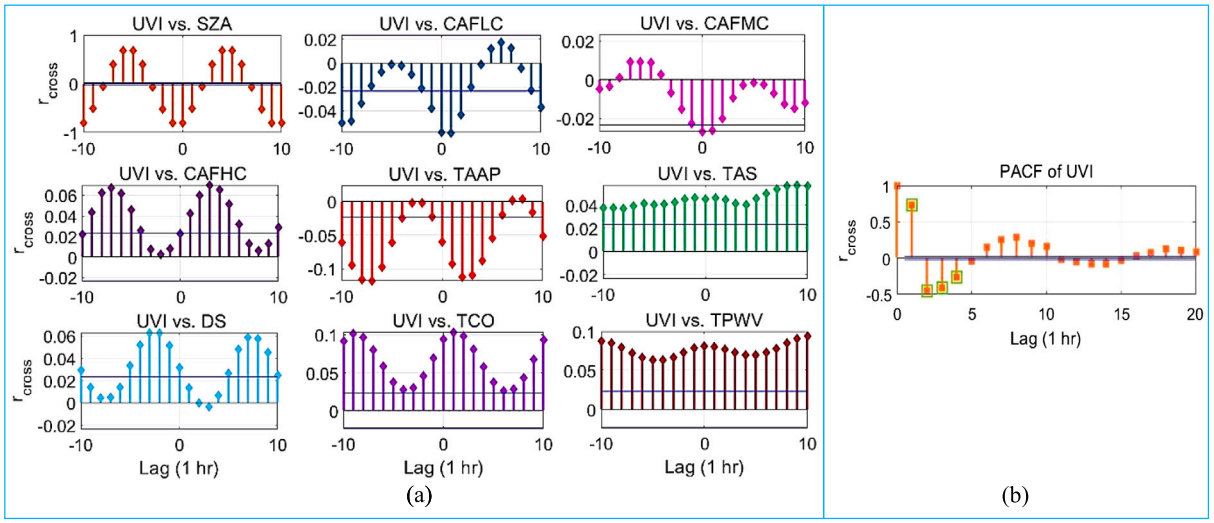

Fig. 2. Hourly lagged correlograms showing (a) cross-correlation coefficient (r_{cross}) for *UVI* versus the nine predictor variables (acronyms described in Table 2) for the Darwin site, (b) Partial autocorrelation function (PACF) of the *UVI* series showing the four most significant lags for the Darwin site.

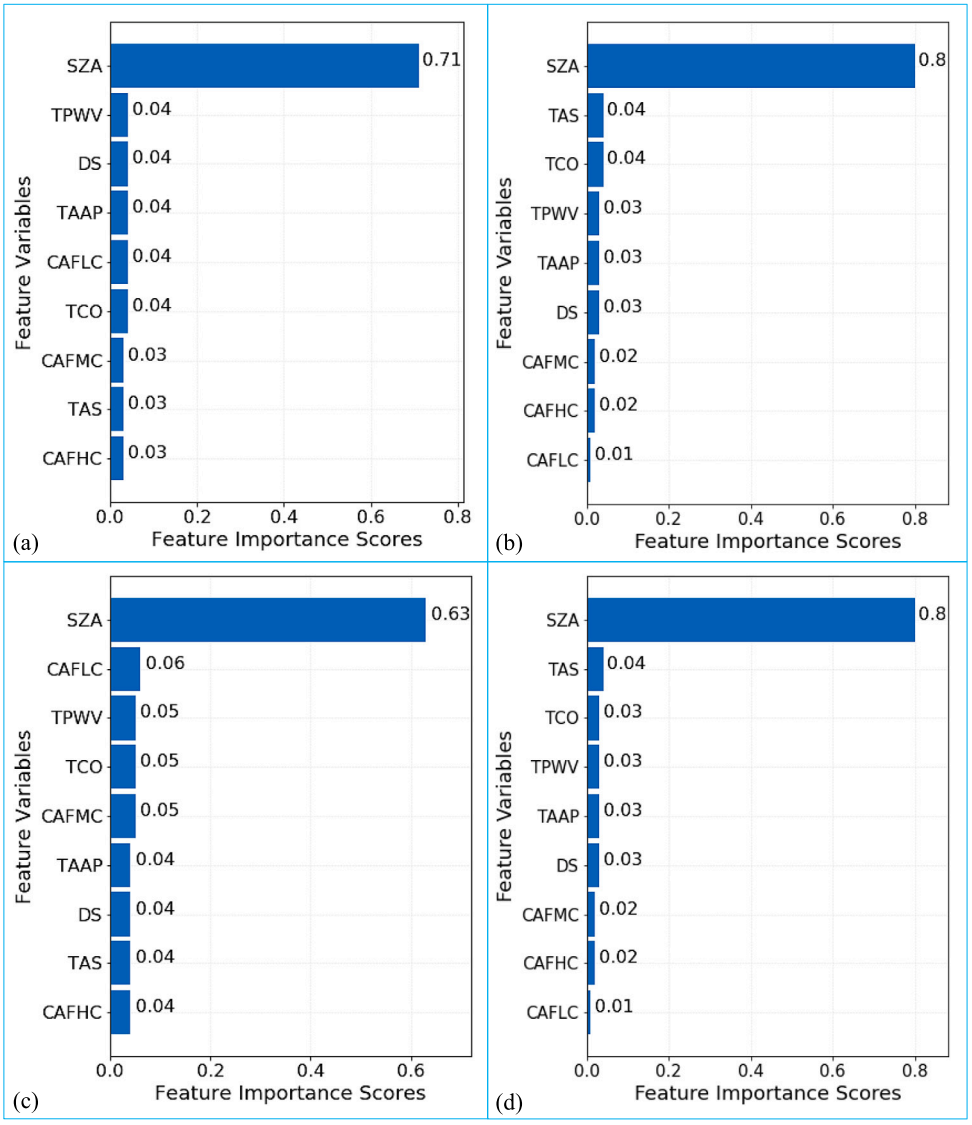

Fig. 3. First phase of feature selection using model-specific feature importance with the base model of random forest for (a) Darwin, (b) Alice Springs, (c) Townsville and (d) Emerald; where any predictor variable having feature importance scores equal to zero is eliminated from the design phase of the hybrid EJH-X-DNN model.

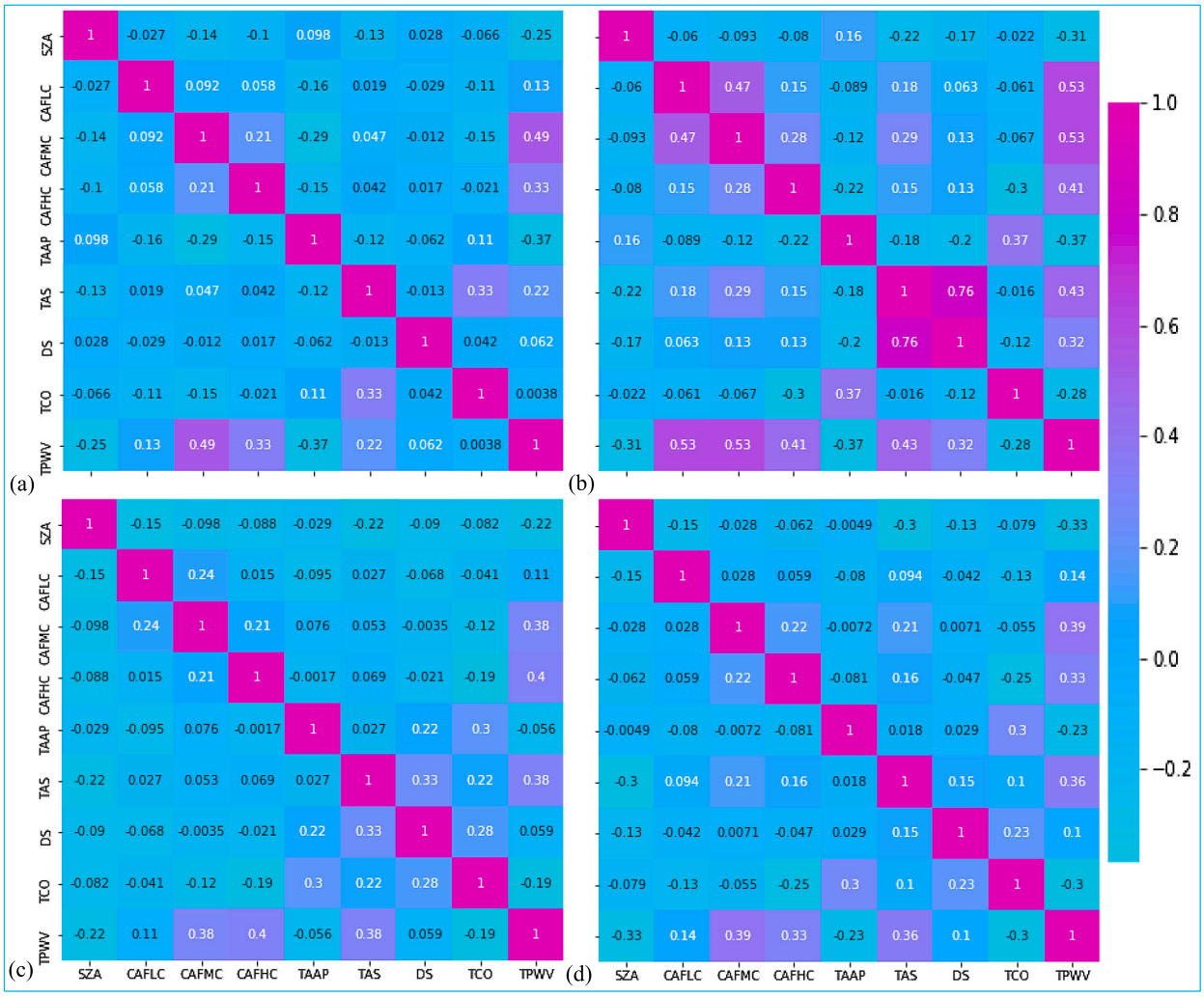

Fig. 4. Second phase of feature selection using a color-coded heat map highlighting a visual overview of low, average and high correlation (r) of the predictor inputs considered for (a) Darwin, (b) Alice Springs, (c) Townsville and (d) Emerald; where any two variables having high r (preferably r > 0.8 or r < -0.8 for this study) are regarded redundant and one of them is eliminated from the design phase of the hybrid explainable EJH-X-DNN model.

memories of *UVI* (PACF1, PACF2, PACF3 and PACF4) were applied as overall inputs towards simulating the next hourly *UVI* series.

3.4. Design of the UVI predictive model

In the fifth stage, the actual hybrid explainable EJH-X-DNN model is designed. For developing the model pipeline, an eminent Python programming language was implemented via a Google Colab platform with a freely available Jupyiter Notebook interface supported by a tensor processing unit (TPU) and graphical processing unit (GPU). The virtual environment of the powerful python tool provides remarkable packages for the execution of ML and DL algorithms, which include Scikit-learn [39], Keras [40] and TensorFlow [41]. Additionally, the MATLAB programming tool was employed for plotting the correlograms of the predictand and predictors [42].

Prior to feeding the target and predictor inputs to the model, the datasets were normalized in the range of [0-1] so that each variable would exhibit the same order of magnitude. This was achieved by applying a min-max normalization [43], defined as follows:

$$X_{NORM} = \frac{X_{ACT} - X_{MIN}}{X_{MAX} - X_{MIN}}, \tag{2}$$

where X_{NORM} is normalized input data, X_{ACT} is actual input data, X_{MIN} is the minimum value and X_{MAX} is the maximum value. Through the normalization process, stable convergence of biases and weights is guaranteed for efficient training and testing of the predictive model [44].

Consequently, a train-test split was carried out by partitioning the input datasets into training, validation and testing, as shown in Table 3. Data segregation is a critical phase of model building as the forecasting capability and overall feasibility of the predictive model are largely dependent on the partitioning ratio. Since there is no standard rule for data partitioning, this study adopts an earlier research strategy [45,46] to segregate 80% of the site-based input datasets for training and 20% for testing. Additionally, 10% of the training data was utilized for model validation, primarily to overcome the issues regarding model biases via a 10-fold cross-validation approach. On the same notion, the modeling constraints led by over-fitting can also be addressed using the cross-validation process [47]. While partitioning, the training and testing datasets were cut-off using date-time to ensure that the future patterns of the training set do not leak into the testing set.

The scope of this study was to design a hybrid explainable EJH-X-DNN model that could simulate more accurate forecasts of hourly horizon *UVI* with local and global model-agnostic interpretability based on the influences of the input features on predicted outcomes. For comprehensive benchmarking of the newly proposed model, we further designed some skillful competing models, which include EJH-FCN, EJH-ANN, EJH-MLP, EJH-AB, EJH-SGD and EJH-DT. The designations of the

Table 4
Designations of the enhanced joint hybrid deep learning and machine learning models developed to simulate hourly ahead forecasts of *UVI*.

Model Type		Model Designation
Proposed xAI Model:	Enhanced Joint Hybrid Explainable DNN	EJH-X-DNN
Benchmarked Models:	Enhanced Joint Hybrid FCN	EJH-FCN
	Enhanced Joint Hybrid ANN	EJH-ANN
	Enhanced Joint Hybrid MLP	EJH-MLP
	Enhanced Joint Hybrid AdaBoost	EJH-AB
	Enhanced Joint Hybrid SGD	EJH-SGD
	Enhanced Joint Hybrid DT	EJH-DT

objective model along with the benchmarked models are distinctly described in Table 4.

In constructing the EJH-X-DNN model, a robust DL DNN was integrated as a suitable base model. The DL-based models are less explored in *UVI* forecasting and their supremacy over conventional ML-based models is well known [15]. A DNN is an extension of an ANN that is constructed by concatenating three principle layers in the architecture: an input layer, one or more fully connected hidden layers and an output layer [48]. The depth of DNN architecture is defined by the number of hidden layers and each layer of the network has available one or more interconnected artificial neurons. By having networks of multiple hidden layers and nodes in the design architecture, the DNN model automatically extracts relevant features or information from the input datasets [49]. For generating time-series predictions, the most suitable number of neurons in the output layer is one. A feed-forward mode is utilized for information processing, which begins from the input layer, goes through the hidden layers, and finally arrives at the output layers. For each layer, the inputs are multiplied by weights, followed by the addition of a bias to the sum of the resulting product. Mathematically, the neural network forward propagation model [45] can be best described as:

$$a_i^l = f\left(\sum_{j=1}^{N^{l-1}} w_{ij}^l a_j^{l-1} + b_i^l\right), \tag{3}$$

where a_i^l is the output value from the i^{th} neurons in the l^{th} layer neural network, a_j^{l-1} is the output value from the i^{th} neurons in the $(l-1)^{th}$ layer neural network, w_{ij}^l is the weight from the j^{th} neurons in the $(l-1)^{th}$ layer to the i^{th} neurons in the l^{th} layer, b_i^l is the bias term from the i^{th} neurons in the l^{th} layer neural network, N^{l-1} is the number of neurons in the $(l-1)^{th}$ layer and $f(\cdot)$ is the activation function of the neurons.

A common DL DNN architecture comprising a feed-forward back propagation network (FFBPN) is applied in this study. Generally, the FFBPN in the architecture enables the model to efficiently learn and map the input-output relationships. Through the processes of learning and mapping, the model's weight and threshold values are adjusted so that the predictive error is minimized and the overall performance is optimized. Selection of an optimal number of hidden layers, neurons, activation functions (such as sigmoid function, hyperbolic tangent (tanh) function, rectified linear unit (ReLU) function and exponential linear unit (ELU) function) further optimizes the model performance [48]. Additionally, the issue of overfitting in DNN is significantly reduced by exploiting a regularization approach that includes a weight penalty and early stopping (or dropout) during model training [45]. In constructing the enhanced joint hybrid benchmarked models, the architecture of base models includes a fully convolutional network (FCN), artificial neural network (ANN), multilayer perceptrons (MLP), AdaBoost (AB), stochastic gradient descent (SGD) and decision tree (DT), respectively. The conceptual and architectural details of the benchmarked models are elucidated elsewhere, as these are well-known methods [50–55].

3.5. Hyperparameter tuning using Bayesian optimizer

While the DNNs exhibit superior performance capability, the forecasting accuracy can be affected by improper tuning of model hyperparameters during training and validation. To enhance the predictive performance, a powerful BO was applied with a Gaussian process surrogate algorithm for optimizing the hyperparameters of the DNN architecture. BO is an elegant hyperparameter tuning algorithm that directs the search for a global optimization problem based on Bayes' rule of conditional probability [56]. The Bayes' rule of conditional probability [57] is given as:

$$p(w|D) = \frac{p(D|w)\ p(w)}{p(D)}, \tag{4}$$

where $p(w|D)$ is the posterior distribution, $p(D|w)$ is the likelihood, $p(w)$ is the prior distribution, $p(D)$ is the marginal, w is an unobserved quantity and D is the input dataset.

The BO approaches the optimal point more efficiently than random sampling because the optimization process selects the values of the next iteration by considering the outcomes of prior iterations [56]. In comparison with other common optimization techniques such as grid search and random search, BO has higher hyperparameter tuning efficiency [58]. For grid and random search, each evaluation in its iterations is independent of prior iterations. In such cases, the hyperparameter search space regions with unsatisfactory performance are unavoidably assessed, which finally leads to high computational costs.

During optimization, the BO fits a surrogate function over an unknown objective function using randomly selected data points. A highly robust and flexible Gaussian process [59], which is also utilized for the purpose of this study, forms the posterior distribution over the objective function to consequently update the surrogate function. In this instance, an acquisition function is generated using the posterior distribution to explore new regions within the search space, as well as to make use of the regions captured with optimal results [60]. These processes continue to feed the surrogate model with updated outcomes and terminate just after meeting a pre-defined stopping criterion. In this case, the acquisition function, known as the expected improvement (EI) [58] is applied where the criterion is to maximize this function to locate the next sampling point. The EI is given as:

$$\mathrm{EI}(\theta) = \frac{P_{good}(\theta)}{P_{bad}(\theta)}, \tag{5}$$

where P_{good} is the probability that θ is in the good group, P_{bad} is the probability that θ is in the bad group and θ represents the hyperparameter set.

Table 5 details the search space and the optimal architecture of the proposed model that includes the number of neurons in the input layer and hidden layers, batch size, number of epochs, activation function, optimizer, learning rate and the parameters of the backpropagation algorithm (β_1, β_2 and Epsilon) for the four selected sites. The input layer of DNN architecture was selected using the dual-phase feature selection approach. To achieve a deep architecture of DNN, four hidden layers were utilized. The output layer was assigned a single neuron to generate the predicted *UVI*. While we selected a good learning rate of 0.001,

Table 5
Optimal architecture of the hybrid explainable EJH-X-DNN model and the competing counterparts designed to generate hourly ahead *UVI* forecasts.

Predictive Models	Hyperparameters	Search Space	Optimal Hyperparameters			
			Darwin	Alice Springs	Townsville	Emerald
EJH-X-DNN	Input neurons	[100, 110, 120]	100	120	100	110
	Hidden neurons 1	[70, 80, 90]	70	70	90	90
	Hidden neurons 2	[40, 50, 60]	60	60	40	40
	Hidden neurons 3	[20, 25, 30]	20	25	30	20
	Hidden neurons 4	[5, 10, 15]	10	10	15	15
	Batch size, Epochs	[200, 300], [150, 200]	200, 150	200, 150	200, 200	200, 200
	Activation function	[ReLU]	ReLU			
	Optimizer, Learning rate	[Adam], [0.001]	Adam, 0.001			
	β_1, β_1, Epsilon	[0.9], [0.999], [1×10^{-10}]	0.9, 0.999, 1×10^{-10}			
EJH-FCN	Filters 1	[50, 80, 100]	80	100	80	50
	Filters 2	[40, 50, 60]	50	40	60	50
	Filters 3	[20, 30, 40]	30	40	30	40
	Batch size, Epochs	[200, 300], [150, 200]	300, 150	200, 150	200, 200	200, 150
	Activation function	[ReLU]	ReLU			
	Optimizer, Learning rate	[Adam], [0.001]	Adam, 0.001			
	β_1, β_1, Epsilon	[0.9], [0.999], [1×10^{-10}]	0.9, 0.999, 1×10^{-10}			
EJH-ANN	Input neurons	[100, 110, 120]	100	110	110	100
	Hidden neurons	[30, 40, 50]	40	50	50	40
	Batch size, Epochs	[200, 300], [150, 200]	200, 200	300, 200	200, 200	300, 200
	Activation function	[ReLU]	ReLU			
	Optimizer, Learning rate	[Adam], [0.001]	Adam, 0.001			
	β_1, β_1, Epsilon	[0.9], [0.999], [1×10^{-10}]	0.9, 0.999, 1×10^{-10}			
EJH-MLP	Hidden layer sizes	[30, 50, 80]	50	80	80	80
	Learning rate init	[1×10^{-5}, 1.5×10^{-5}]	1.5×10^{-5}	1.5×10^{-5}	1.5×10^{-5}	1.5×10^{-5}
	Maximum iteration	[1000, 2000, 3000]	3000	3000	3000	3000
	Tol	[1×10^{-8}, 1.5×10^{-8}, 2×10^{-8}]	1×10^{-8}	1.5×10^{-8}	1.5×10^{-8}	2×10^{-8}
	Activation function	[ReLU]	ReLU			
	Solver, Alpha	[Adam] , [0.0001]	Adam, 0.0001			
	β_1, β_1, Epsilon	[0.9], [0.999], [1×10^{-10}]	0.9, 0.999, 1×10^{-10}			
EJH-AB	n estimators	[100, 200, 300]	100	100	200	200
	Learning rate	[1.0, 1.5, 2.0]	1.0	1.0	1.0	1.0
	Loss	[linear]	linear			
EJH-SGD	Eta0	[0.01, 0.02, 0.03]	0.03	0.03	0.02	0.03
	Power_t	[0.25, 0.30, 0.35]	0.25	0.25	0.25	0.25
	Maximum iteration	[500, 1000, 1500]	1000	1500	1500	1000
	Tol	[0.001, 0.002, 0.003]	0.002	0.001	0.001	0.001
	Alpha	[0.0001]	0.0001			
EJH-DT	Minimum samples split	[2, 4, 6]	6	6	4	6
	Maximum depth	[5, 10, 15]	5	15	5	10
	Minimum samples leaf	[1, 5, 10]	5	10	10	10
	Maximum features	['auto', 'sqrt', 'log2']	'auto'			

the activation function was selected as ReLU. To further handle the issue of over-fitting, an early stopping technique was employed through monitoring the model performance during the validation phase. The BO algorithm was also implemented to tune the hyperparameters of the counterpart models, for which the search details and optimized architectures are described in Table 5.

3.6. Model performance criteria

The study applied a range of performance metrics for rigorous evaluation of the newly constructed EJH-X-DNN model against the benchmarked models in forecasting hourly ahead *UVI* for the four Australian sites. The set of these statistical metrics includes Pearson's Correlation Coefficient (*r*), Mean Absolute Error (*MAE*), Root Mean Squared Error (*RMSE*) and the Legate-McCabe Efficiency Index (*LME*) [23,61]. Mathematically, these metrics can be represented as:

$$r = \frac{\sum_{i=1}^{N}\left(UVI_i^O - \overline{UVI}^O\right)\left(UVI_i^F - \overline{UVI}^F\right)}{\sqrt{\sum_{i=1}^{N}\left(UVI_i^O - \overline{UVI}^O\right)^2}\sqrt{\sum_{i=1}^{N}\left(UVI_i^F - \overline{UVI}^F\right)^2}}, \quad (6)$$

$$RMSE = \sqrt{\frac{1}{N}\sum_{i=1}^{N}(UVI_i^O - UVI_i^F)^2}, \quad (7)$$

$$MAE = \frac{1}{N}\sum_{i=1}^{N}\left|UVI_i^O - UVI_i^F\right|, \quad (8)$$

and

$$LME = 1 - \frac{\sum_{i=1}^{N}\left|UVI_i^O - UVI_i^F\right|}{\sum_{i=1}^{N}\left|UVI_i^O - \overline{UVI}^O\right|}, \quad (9)$$

where N is the total number, UVI_i^O and UVI_i^F are observed and forecasted *UVI* for the i^{th} observation, $\overline{UVI}^O$ and $\overline{UVI}^F$ are average observed and average forecasted *UVI*. The values of r range between -1 to +1, where the two extremes are ideal values. The error values of *MAE* and *RMSE* range from 0 to ∞, where 0 and ∞ imply a perfect fit and worst fit, respectively. The *LME* can robustly address the predictive limitations and it ranges between 0 to 1, where 1 is an ideal value.

3.7. Explainability of model outcomes

In the next stage, xAI-based model-agnostic tools were exploited to explain the predictions of the newly designed EJH-X-DNN model for the four hotspots. To extract local explainability, the LIME algorithm was applied to reveal the instance-based local impact of respective predictor variables fed in the *UVI* simulating system. To obtain global explainability, the SHAP and PFI tools were applied.

3.8. xAI-based local interpretable model-agnostic explanations (LIME)

The LIME algorithm is an eminent xAI tool that efficiently explains the predictions of a regression or classification "black-box" model by approximating it locally with a surrogate interpretable model [62]. To generate model explanations, LIME supports three formats of input datasets that include image, text and tabular data [63]. For the current study, LIME is applied with a tabular data format to derive local interpretability. The model explanations offered by LIME allow the end users to understand and interpret the predictive decisions. The LIME-defined explanation [64] is given as:

$$\xi(x) = \underset{g \in G}{\operatorname{argmin}}\, \mathcal{L}(f, g, \pi_x) + \Omega(g), \tag{10}$$

where f denotes the explained black-box model, π_x is the proximity measure defining the neighborhood size around instance x, G represents the set of interpretable models, $\mathcal{L}(f, g, \pi_x)$ is the measurement of the unfaithfulness of explanation model g in approximating prediction of the original black-box model f, and $\Omega(g)$ component measures the complexity of the explanation for all $g \in G$. The first goal is to have a low $\Omega(g)$ component so that the model is simple enough to offer better interpretability. The second and major goal is to minimize the $\mathcal{L}(f, g, \pi_x)$ component to achieve an interpretable approximation of the original reference model.

LIME enumerates local explanations that highlight the contribution of individual feature variables toward the black-box prediction of a sample data [16]. In accomplishing this, LIME replicates the feature data by perturbing the input observations several times, thereafter generating a prediction with the black-box model based on the perturbed data. By benchmarking the perturbed data with the original data point, LIME determines the Euclidean distance between them. Finally, LIME uses the calculated distance of the original observation from the perturbed data point and indicates which input features are useful for the black-box model in generating predictions.

3.9. xAI-based Shapley additive explanations (SHAP)

SHAP algorithm robustly extracts global explanations in terms of interactions and influences of the feature variables on decisions of a black-box model in delivering predictions [65]. For this purpose, the SHAP tool is deployed to enhance the global interpretability of the *UVI* predictive framework. The foundation of SHAP is derived from the concept of Shapley value in game theory, which has a major goal of fairly distributing the players' contributions in achieving a particular outcome collectively [66,67]. Similarly, Shapely values can be applied in black-box models, to quantify the contribution of individual predictor variables for generating predictions. For a given predictor, X_j in a black-box model, the SHAP value [66,65] is given as:

$$Shapely(X_j) = \sum_{S \subseteq N \setminus \{j\}} \frac{k!\,(p-k-1)!}{p!} \left(f(S \cup \{j\}) - f(S)\right), \tag{11}$$

where $N \setminus \{j\}$ defines the set of all possible combinations of feature variables excluding X_j, S represents a feature set in $N \setminus \{j\}$, p denotes the total number of features, $f(S)$ represents the black-box model prediction with features in S and $f(S \cup \{j\})$ represents the black-box model prediction with both features in S and feature X_j. The $Shapely(X_j)$ represents the SHAP value of a feature, which is the weighted average of the marginal contribution over all possible models with different combinations of feature variables [66]. Though SHAP takes up some computational time in executing, the process utilizes all the subsets of the input data to deliver consistent, transparent and more accurate global interpretations. For the purpose of this study, a skillful kernel explainer was utilized while implementing the SHAP algorithm to reveal the impact of the predictor variables on the overall decisions and predictions of the proposed hybrid explainable model.

3.10. Permutation feature importance (PFI)

PFI is another effective xAI tool that is model-agnostic and offers global explanations for the black-box processes in generating predictions. Basically, the PFI is determined by permuting the values of a predictor variable i, followed by the calculation of the increment in prediction error due to this permutation [28]. The PFI score (PFI_s) is given as:

$$PFI_s = e^p - e^o, \tag{12}$$

where e^o is the estimated original model error and e^p is the calculated new error after permuting the values of the feature variable i. A feature with a large PFI score has a higher influence on the model's predictions. PFI can be executed with different error functions, yet the common ones are mean absolute error (*MAE*) and root mean square error (*RMSE*) [28, 68]. For this study, PFI is applied with an error function of *MAE* to globally explain the decisions of the DL *UVI* predictive system.

4. Results

This section consolidates the extensive performance evaluation and model-agnostic explanations of the prescribed EJH-X-DNN model to demonstrate the superiority of the proposed *UVI* forecasting tool against six benchmarked models that include EJH-FCN, EJH-ANN, EJH-MLP, EJH-AB, EJH-SGD and EJH-DT. To appraise the merits of the proposed model based on the statistical score metrics described in (6)-(9) and visual plots, all models were meticulously assessed for generating hourly horizon forecasts using the testing datasets for four solar-rich hotspots in Australia. Table 6 enumerates the testing phase performance of the EJH-X-DNN model against the comparative counterparts for all four sites. Almost all the experimentally captured modeling statistics reveal that the objective model outperforms the competing counterpart models in forecasting *UVI* with the highest Pearson's correlation coefficient (r), lowest root mean square error (*RMSE*) and lowest mean absolute error (*MAE*) for all four hotspots. The proposed model demonstrates superior forecasting capability for each of site by yielding the highest accuracies (i.e. r = 0.897 - 0.960; *RMSE* = 1.071 - 1.638; *MAE* = 0.633 - 1.081) against its counterparts (i.e. r = 0.842 - 0.954; *RMSE* = 1.139 - 2.025; *MAE* = 0.682 - 1.641). We aver that our hybrid explainable EJH-X-DNN model approaches the best predictive precision by capturing r values that approach 1, *RMSE* values that approach 0 and *MAE* values that approach 0 as well.

The assessment of the newly constructed EJH-X-DNN model using the most stringent performance indicator of the Legate-McCabe Efficiency Index (*LME*) further revealed its outstanding performance in Fig. 5. For almost all the hotspots, the objective model yields the highest values of *LME* (i.e. *LME* = 0.652 - 0.804) and outshines the comparative models (i.e. *LME* = 0.466 - 0.789). Having captured the highest *LME* statistics indicates that the proposed model exhibits the lowest stringent errors in forecasting short-term *UVI*.

Consequently, the xAI-inspired model-agnostic tools were applied to robustly offer explanations on the predictive contributions of the input variables that included satellite-derived predictors, ground-based predictors and the antecedent lagged memory of *UVI*. The satellite-derived xAI inputs for this research include cloud cover effects (i.e. CAFHC,

Table 6
Testing phase performance of the newly designed EJH-X-DNN model against the counterpart models in terms of correlation coefficient (*r*), root mean square error (*RMSE*) and mean absolute error (*MAE*) in forecasting hourly ahead *UVI* for the four sites.

UVI Forecast Model	Darwin			Alice Springs			Townsville			Emerald		
	r	*MAE*	*RMSE*	*r*	*MAE*	*RMSE*	*r*	*MAE*	*RMSE*	*r*	*MAE*	*RMSE*
EJH-X-DNN	0.900	1.638	1.081	0.960	1.071	0.633	0.897	1.601	1.068	0.913	1.359	0.883
EJH-FCN	0.889	1.865	1.239	0.950	1.273	0.809	0.872	1.840	1.342	0.906	1.462	1.036
EJH-ANN	0.898	1.659	1.069	0.954	1.139	0.682	0.891	1.675	1.114	0.903	1.473	0.930
EJH-MLP	0.888	1.729	1.133	0.950	1.179	0.704	0.871	1.777	1.271	0.878	1.631	1.112
EJH-AB	0.871	1.966	1.598	0.910	1.872	1.569	0.842	2.025	1.641	0.864	1.771	1.410
EJH-SGD	0.889	1.713	1.138	0.947	1.214	0.757	0.866	1.798	1.315	0.870	1.658	1.170
EJH-DT	0.882	1.776	1.177	0.946	1.228	0.708	0.869	1.793	1.262	0.875	1.701	1.040

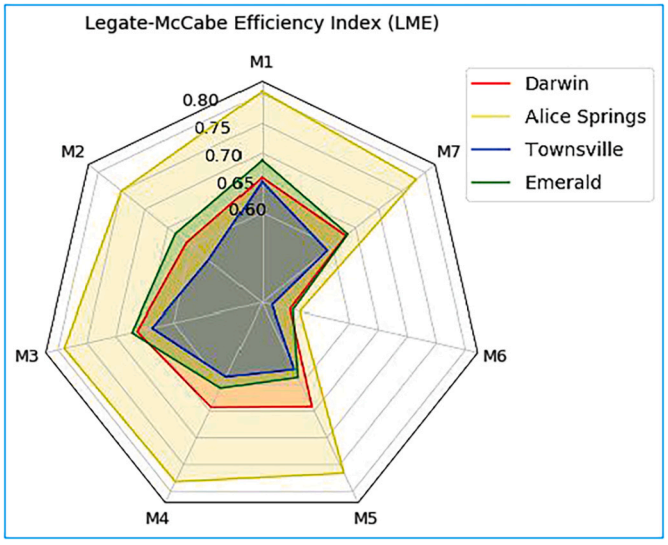

Fig. 5. Rader plot of the Legate-McCabe Efficiency Index (*LME*) elucidating the performance of the newly designed EJH-X-DNN model (M1) alongside the competing benchmarked models of EJH-FCN (M2), EJH-ANN (M3), EJH-MLP (M4), EJH-SGD (M5), EJH-AB (M6) and EJH-DT (M7) in forecasting *UVI* for the four selected sites.

CAFMC and CAFLC), aerosol scattering (i.e. TAS and TAAP), ozone effect (i.e. TCO), dust particles (i.e. DS) and water vapor (i.e. TPWV). Other xAI inputs include the ground-based predictor of solar zenith angle (i.e. SZA) and the antecedent lagged memory of *UVI* at lags of t - 1, t - 2, t - 3 and t - 4 (i.e. PACF1, PACF2, PACF3 and PACF4) for all the selected sites.

To retrieve the local explanations on the predictions of the hybrid explainable model, the study applied an elegant LIME model-agnostic framework. In this study, the number of LIME-explainable instances was equal to the number of hourly *UVI* datum points in the testing data series that ranged from instance 0 to instance 5815. For the purpose of visualization, the LIME-generated local explainability analysis on instance-based prediction is displayed in Fig. 6 for instance 25 and instance 175. The local interpretability presented with the aid of bar graphs reflects individual feature contributions towards the forecasting of these instances for the four Australian hotspots that have high ground-level UV exposures. On the bar graphs, the y-axis displays the features with corresponding feature values, while the x-axis shows the relative strengths of individual features in terms of their numerical contributions. The attributes that have increased or supported the predicted value of the *UVI* forecast are emphasized in green. Conversely, the attributes that have decreased or negatively impacted the predicted instance are highlighted in red. Additionally, the predicted value of *UVI* is represented on a bar in orange color.

The comparisons of LIME outputs at instance 25 and instance 175 for the Darwin, Alice Springs and Townsville sites in Fig. 6 (a)-(c) reveal that the feature attributes of PACF1 and SZA are the major contributors towards the outcome of *UVI* forecasting. However, for the Emerald site in Fig. 6 (d), PACF1 is the major contributor in predicting *UVI* for both instances. Moreover, SZA shows a positive effect on *UVI* predictions for all four hotspots. It is also observed that PACF1 has contributed positively for most instances, except for instance 175 of the Darwin site and instance 25 of the Emerald site, where the predictive contributions were negative. As per the LIME values presented on the x-axis, PACF1 is the largest predictive contributor at instance 175 for the Alice Springs and Emerald site where PACF1 > 6.38 strongly envisages the outcome of the *UVI* forecast. However, as per instance 25 of Emerald site where 1.52 < PACF1 < 3.71, it has the highest negative effect on this predictive outcome. SZA is shown to be largely responsible for the prediction outcomes for both instances at the Darwin site. At this site, SZA > 30.21° highly favors the prediction outcome. Other predictors that include TCO, PACF3, TPWV, CAFMC and CAFHC also displayed significant predictive contributions at different sites. The overall outputs of the LIME tool offer substantial instance-based local interpretations that can boost the trustworthiness of the hybrid explainable EJH-X-DNN model.

For extracting the global explanations on the entire predictions of the hybrid explainable model, the study applied a classic SHAP model-agnostic framework. The SHAP feature importance bar plots presented on the left-hand side in Fig. 7 illustrate the mean absolute Shapley values of individual features on the x-axis and the ranked input features on the y-axis. These attributes are ranked by prioritizing the features with larger absolute Shapley values. The SHAP summary violin plots presented on the right-hand side in Fig. 7 display the feature effects of the ranked attributes based on the feature importance. In outlining the violin plot, each instance equal to the number of hourly *UVI* datum points in the testing data series is plotted with the corresponding Shapley value for each feature attribute on the x-axis against ranked input features on the y-axis. The feature value at each instance is denoted by different colors with pink and light blue representing high and low feature values, respectively. The higher feature values of all the predictor variables denoted in pink imply positive Shapley values that highly contribute towards the outcome of *UVI* prediction. In contrast, the lower feature values shown in light blue have negative Shapley values that do not favor the outcome of predicted *UVI*.

The inforgraphics presented in Fig. 7 reveals that PACF1 and SZA have the most impact on the outcome of the *UVI* forecast for all four Australian hotspots. For the Darwin site in Fig. 7 (a), SZA contributes more than PACF1 towards the predictive outcome on the Shapley scale. However, PACF1 is more dominant in impacting the outcome of predicted *UVI* for the Alice Springs, Townsville and Emerald hotspots in Fig. 7 (b)-(d). For these highly impactful predictors, the higher feature values in pink favor the outcomes of *UVI* predictions, while those in light blue with lower values of features do not favor the predicted outcomes. Together with PACF1 and SZA, other influential attributes on *UVI* predictions include TCO, PACF3, TPWV, PACF2, CAFMC and CAFLC for most sites. It is further observed that the importance of the DS attribute is negligible on the SHAP summary plots for all four hotspots. Further descriptions of the variations in model predictions

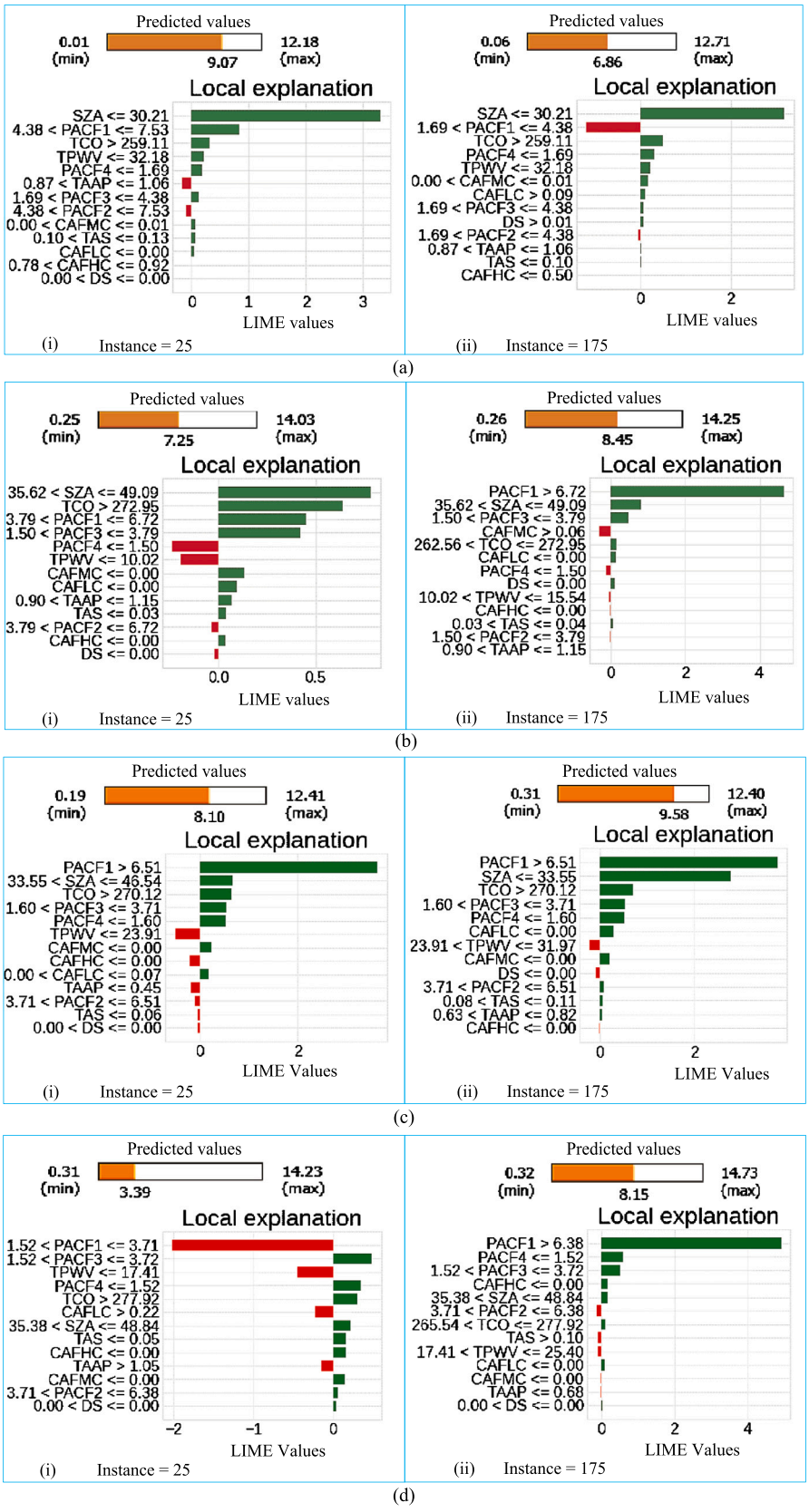

Fig. 6. LIME explanation bar plots at (i) instance 25 and (ii) instance 175 for the sites (a) Darwin, (b) Alice Springs, (c) Townsville and (d) Emerald, where the green bars indicate that the features have a positive impact on the model (increase the model score) and the red bars indicate that the features have a negative impact on the model (decrease the model score).

with respect to the feature importance values and respective feature interactions can be obtained using a SHAP dependence plot.

The SHAP dependence plots shown in Fig. 8 can help understand the marginal effect of two attributes on the predicted outcome of the hy-

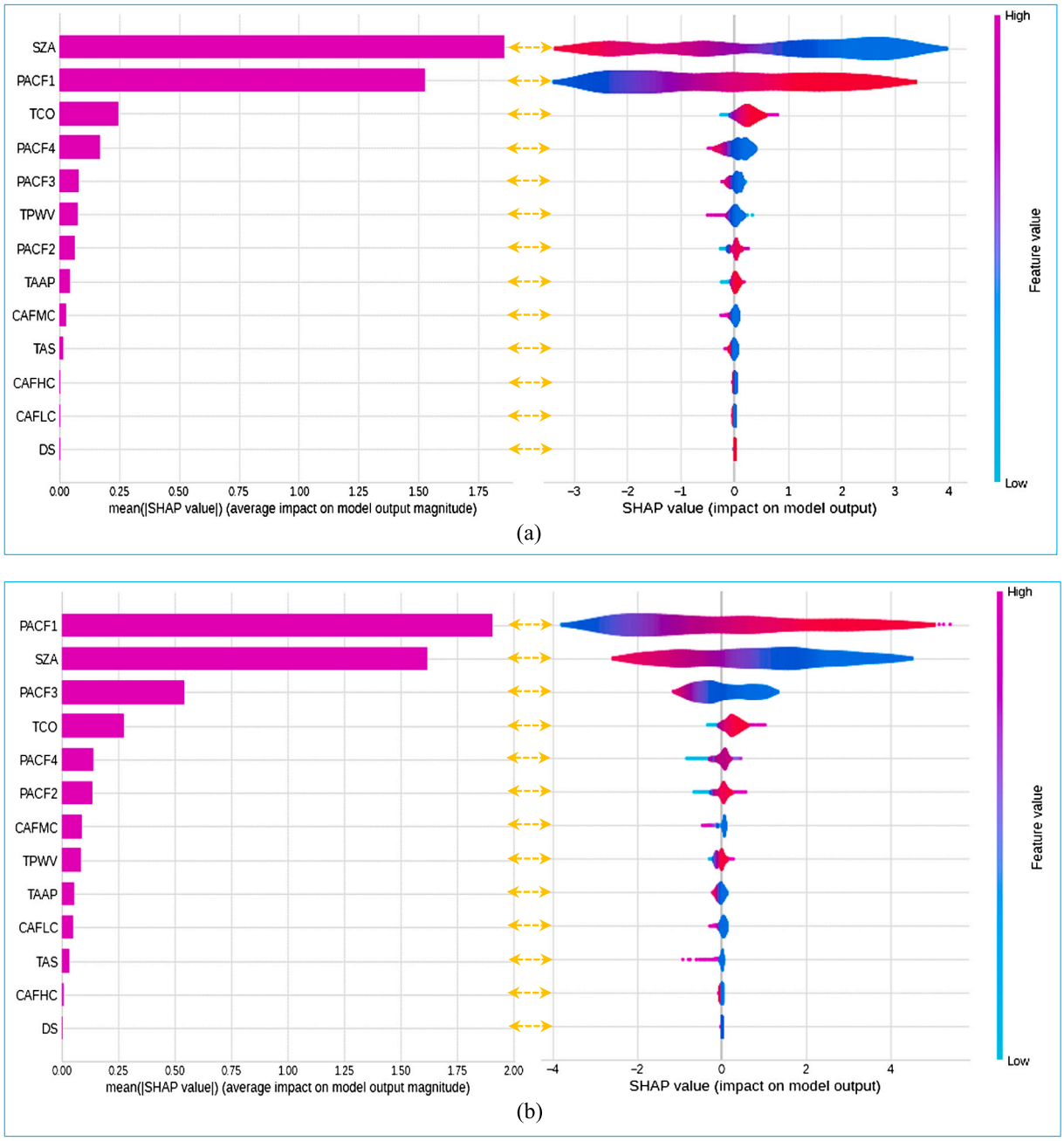

Fig. 7. SHAP feature importance bar plots and SHAP summary violin plots for the sites (a) Darwin, (b) Alice Springs, (c) Townsville and (d) Emerald.

brid explainable EJH-X-DNN model. For the purpose of this study, these plots were utilized to explore the testing phase interactions between the most influential predictor variables i.e. PACF1 and SZA towards the model prediction outcomes. For the Darwin hotspot, the SHAP dependence plot in Fig. 8 (a) reveals that the predicted values of *UVI* are more likely to be favored when SZA < 47° and PACF1 values are high. In the case of the Alice Springs site, the SHAP dependence plot in Fig. 8 (b) indicates that with SZA < 52° and high values of PACF1, it is more likely that the predicted *UVI* values are favored. Similarly, interactions between these two features in Fig. 8 (c) show that the predicted *UVI* values are more likely to be favored at high values of PACF1 and SZA < 36° for the Townsville site. Moreover, the predicted *UVI* values for the Emerald hotspot in Fig. 8 (d) are more likely to be favored when SZA < 46° and PACF1 values are high. For all the sites, it is observed that the feature interactions between the two most influential predictor variables of SZA and PACF1 highly favor the prediction outcomes of the proposed EJH-X-DNN model at lower values of SZA and higher values of PACF1.

For further veracity and comparisons of the global interpretable results generated by SHAP, a prominent PFI model-agnostic framework was applied. The PFI bar plots presented in Fig. 9 rank the predictor variables with respect to their PFI values and illustrate that SZA and PACF1 are the most influential attributes in impacting the prediction outcomes of the newly developed EJH-X-DNN model. It is observed that the results of the PFI bar plots and the SHAP summary plots (Fig. 7) are almost in conformity. According to the PFI plots, Fig. 9 (a) and Fig. 9 (c) reveal that the most impactful features for the Darwin and Townsville site are SZA and PACF1, while TAS and DS have very less impact on the prediction outcome. Fig. 9 (b) shows that PACF1 and SZA are the most influential predictor variables, while TAAP has the least influence in predicting *UVI* for the Alice Springs hotspot. For the Emerald hotspot in Fig. 9 (d), PACF1 and SZA are the most important attributes in gen-

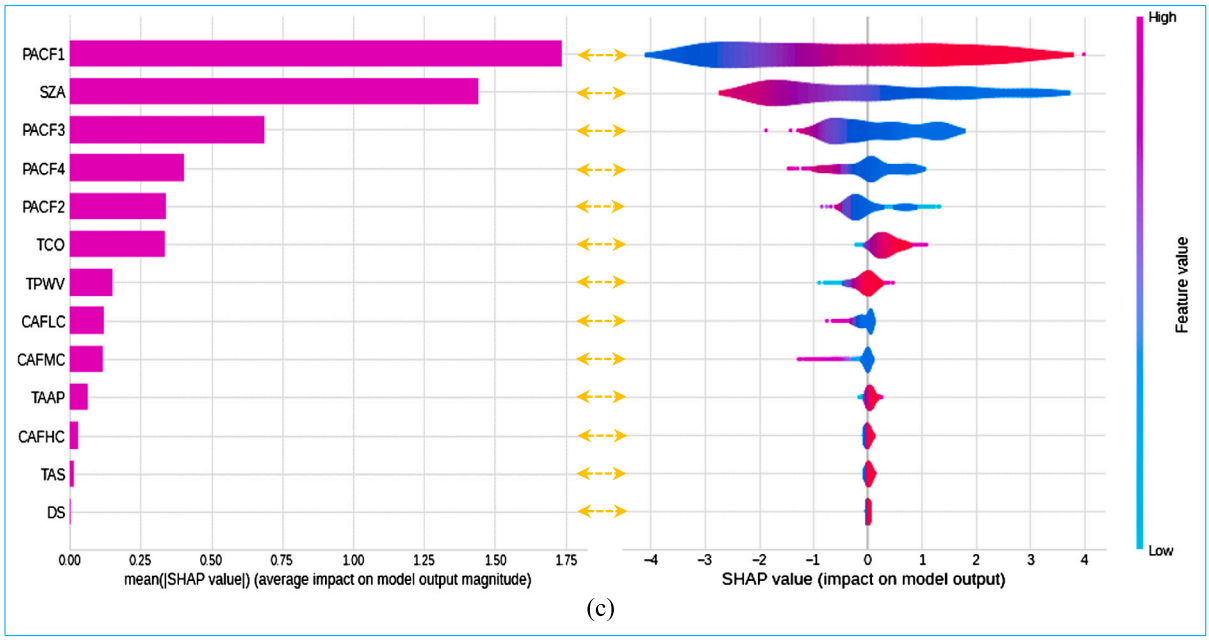

Fig. 7. (*continued*)

erating *UVI* prediction outcomes, while TAAP and DS show the lowest importance. The implementation of the PFI model-agnostic tool along with the SHAP framework offers more reliable and in-depth global explanations of the *UVI* prediction outcome by the proposed model for the usefulness of the end-users.

5. Discussion

The artificial intelligence predictive system designed in this study robustly forecasts short-term *UVI* to demonstrate its efficacy as a decision support tool that can deliver more accurate sun-exposure information to the public and help mitigate UV radiation-associated skin diseases and eye health ailments. The performance evaluation aptitudes, such as those illustrated in Table 6 and Fig. 5 offer compelling evidence to establish the hybrid explainable EJH-X-DNN model as a credible *UVI* forecasting system for all four Australian hotspots that are exposed to high ground-level UV radiation. Alongside the comparative models, the proposed model is the most superior forecasting framework as its assessment demonstrates high-performance efficiencies with all the performance measurement criteria. After testing on four different datasets of Darwin, Alice Springs, Townsville and Emerald hotspots, we further assert that the prescribed model exhibits remarkable forecasting stability as it captured the lowest error values of *RMSE* and *MAE* on almost all four datasets. Though the proposed model outperformed the benchmarked models for all four sites, it delivered the best site-based performance for the Alice Springs hotspot. The site-to-site variations in performance are largely led by the intermittent and stochastic nature of the cloud cover effects. For instance, the evaluation outcomes of the Darwin site have recorded slightly better *MAE* and *LME* values by the EJH-ANN model while the *r* and *RMSE* values are dominated by the proposed EJH-X-DNN model. Despite these subtle variations in performance, all other captured aptitudes affirm the prescribed model as the best overall performer in forecasting hourly ahead *UVI* for the four sites.

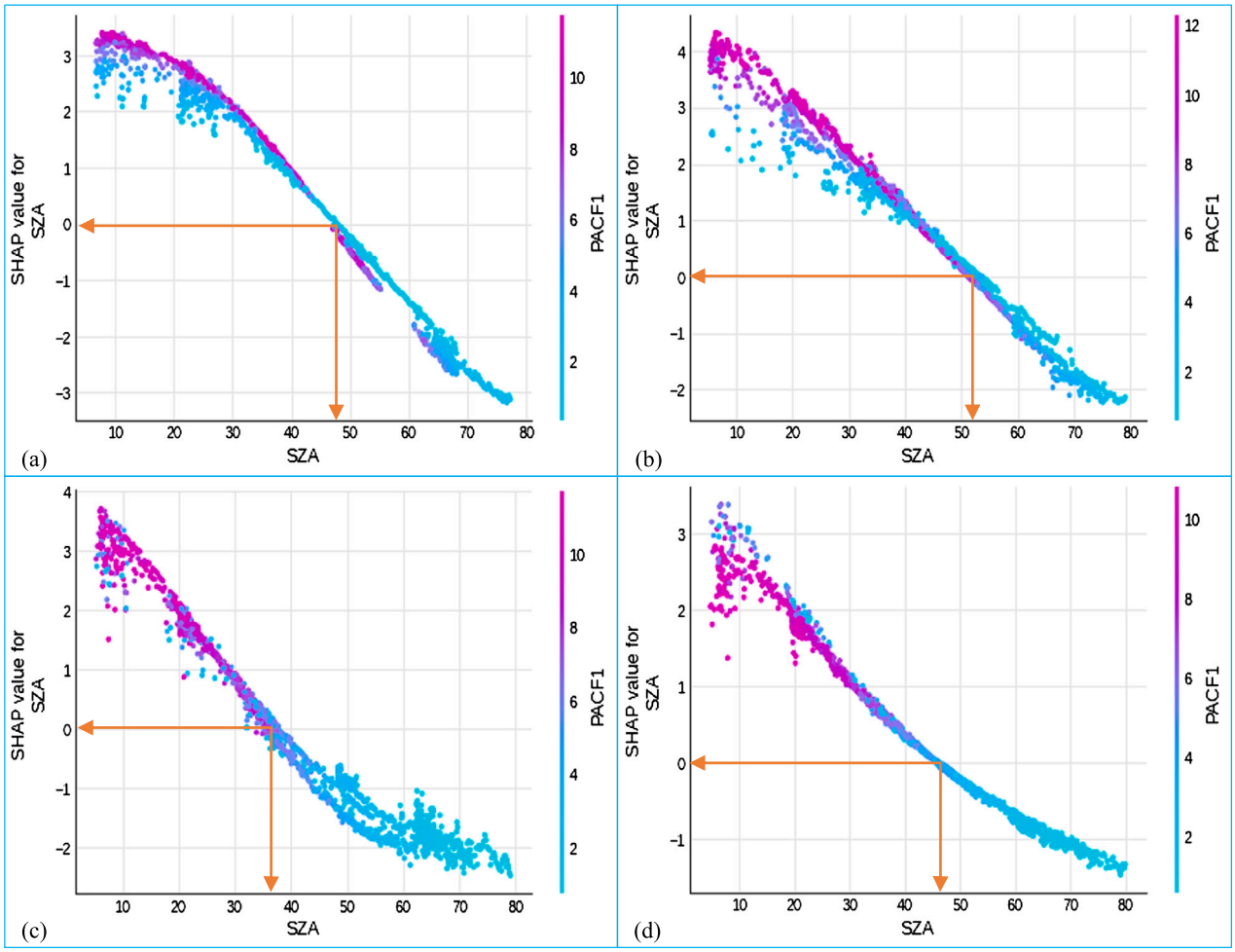

Fig. 8. SHAP dependence plots for interaction between SZA and PACF1, which are the most important features in the UVI forecasting framework for (a) Darwin, (b) Alice Springs, (c) Townsville and (d) Emerad.

Though the outcomes of the newly designed EJH-X-DNN model are promising, this study employed the xAI tool to further expand the model's transparency and reliability for its practical applications. According to the literature, some previous studies have developed AI-based ML and DL models to forecast solar *UVI* for different sites [14,5,27,15]. However, it is evident that none of the previous studies have designed a *UVI* forecasting system by integrating the xAI tool to explain the predictive outcomes of their models. Thus, by applying a model-agnostic xAI approach to offer the predictive explanations of the proposed DL "black-box" model, the current research fills this gap in the literature. Through the applications of xAI in this study, the "black-box" model interpretations of the decisions taken in simulating *UVI* forecasts were obtained both in terms of local and global explanations. [69] proposed the applications of the fascinating LIME, SHAP and PFI algorithms to extract local and global post-hoc explanations based on the input perturbations using a classification-based predictive model to classify oropharyngeal cancer. The current study also applied the xAI frameworks of LIME, SHAP and PFI, but with a major focus on explaining a forecasting-based model in predicting hourly horizon *UVI*.

The advantage of applying LIME is its ability to offer instance-based model explanations for the time-series *UVI* forecasting system developed in this study. LIME has the capacity to obtain better coverage values in terms of weighted sums so that the end users could easily comprehend how the predictions are made for each instance [17,64]. The applications of SHAP and PFI framework are also highly beneficial as these tools provide global explanations of the newly designed *UVI* forecasting system. The SHAP values based on coalitional game theory capture the mean marginal contribution of individual feature attributes to the single prediction made by a "black-box" model [69]. Here, the motivation for the approach is that the SHAP-extracted explainable outcomes are statistically more reliable. For the purpose of this study, the SHAP xAI algorithm offers a complete explanation between the global average and the model output as the overall interpretation of the predicted *UVI*. Considering the PFI algorithm [28], this tool presents global explanations of the "black-box" model predictions by using the aggregated importance scores to account for the impact of feature attributes on the entire performance of the prescribed *UVI* simulating system. The study applied both the SHAP and PFI frameworks, to generate remarkable comparisons of the global explanations for the proposed *UVI* predictive system for the four Australian hotspots.

The overall instance-based model explanations acquired using LIME indicate that PACF1 and SZA are the two major contributors towards predicting short-term *UVI* for all four Australian hotspots. Similarly, the outcomes of SHAP and PFI tools have revealed PACF1 and SZA as the most impactful predictor variables in generating *UVI* predictions for these four hotspots. Further model explainability extracted using the LIME, SHAP and PFI xAI frameworks show that the contribution of the DS feature variable towards *UVI* predictions is very low. This indicates that the scattering of solar UV radiation by the atmospheric dust particles has very less impact on ground-level UV radiation. The analysis of the SHAP summary and feature importance plots highlight that the effect of the TAS attribute is also significantly low on the model predictions for almost all the sites. In terms of the cloud cover effects, the attributes of CAFMC and CAFLC show some significant influence on the

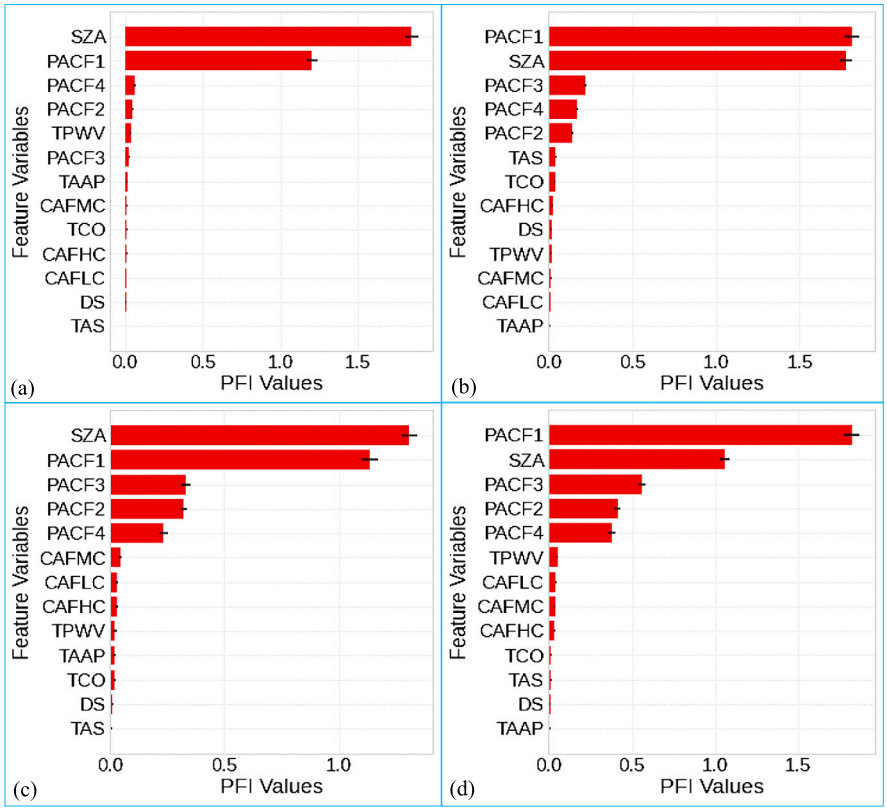

Fig. 9. Permutation feature importance (PFI) bar plots for (a) Darwin, (b) Alice Springs, (c) Townsville and (d) Emerald.

forecasted *UVI*. It is known that the scattering by partial cloud cover may cause a sudden escalated spike in the stochastic UV, which can exceed nominal cloud-free surface solar UV radiation [5]. The SHAP summary and feature importance plots offer vivid global explanations of how each attribute impacts the model decisions in generating the predictive outcomes of the *UVI* forecasts. The global explainability outcomes of the SHAP summary plots, together with the PFI results offer a generic overview of the ranked impacts that each feature has on the model forecasts.

The findings of forecasting performance and model explainability outcomes presented in this research have indicated remarkable practical applications of the newly designed EJH-X-DNN model to forecast short-term *UVI* by replacing the previously used mechanistic measurement and deterministic modeling techniques. It is known that the traditional mechanistic method is highly constrained by the issue of accessibility for most remote regions, along with high installation, operation and maintenance costs [15]. The proposed hybrid explainable EJH-X-DNN model can robustly substitute the mechanistic approach as it is potentially portable, cost-effective and user-friendly for the benefit of the end-users. Our proposed model can also substitute the conventional deterministic method that is constrained by the applications of assumed fixed initial conditions [5]. There are no assumed initial conditions being integrated into the architectural design of this hybrid explainable *UVI* forecasting framework.

The prescribed DL model trained with atmospheric variable datasets avers its practical utility in forecasting short-term *UVI* for most temperate countries, particularly for remote regions. For instance, our model trained with cloud cover conditions datasets can overcome the complex intermittency issue to successfully predict the cloud-affected *UVI*. It is known that the unbroken cloud cover condition attenuates the ground-level *UVI* by 50 to 60% and even more during precipitation [5]. However, under partial cloud cover conditions, the sudden spikes of scattered intermittent UV radiation are escalated above the nominal cloud-free surface solar UV radiation. Due to the significant influence of stochastic cloud cover effects on the ground-level *UVI*, this study adopted a short-term forecasting horizon instead of a long-term to ensure that the escalated spikes of UV radiation are effectively captured. The proposed model is also trained with aerosol, ozone, dust scattering and precipitation datasets to enhance the forecasting capability and applicability of the hybrid explainable model for most geographical locations outside the range of the current ARPANSA network in Australia, as well as other temperate countries where the general public is at high risk of harmful UV exposure effects.

Considering the enhanced performance and ability to offer explainable outcomes, we have further exemplified the potential real-life application of the proposed *UVI* forecasting system in Fig. 10. The predictive system works on online and offline modes to deliver short-term forecasted sun exposure information to the public at risk of UV exposure. The online system is a pre-trained EJH-X-DNN model that can integrate the new unlabeled datasets as inputs to forecast hourly ahead *UVI*. This early warning UV exposure tool can deliver the predictions in terms of low, moderate and high *UVI*, together with the evaluated aptitudes that present the predictive correctness in terms of *r*, *MAE*, *RMSE* and *LME* on the user interface. The user interface can also offer local and global model-agnostic explanations to increase the reliability and trustworthiness of model predictions. Through the offline framework, the proposed model can be continuously trained, fine-tuned and updated with the newly labeled datasets derived from the databases. The updated model via the offline framework can replace the pre-trained online model on a periodic basis to maintain robust and credible forecasting performance. Through further analysis of the user interface outputs, an expert end-user (preferably a UV specialist or a forecaster) can provide real-time sun-protection behavior recommendations to the general public to mitigate UV-exposure-related eye and skin diseases, including skin cancers.

Most of the powerful AI-inspired technologies suffer from the fact that it becomes difficult to explain why a certain outcome was predicted. The robustness of the “black-box” models is affected by even the smallest perturbations in the input data that induce dramatic effects

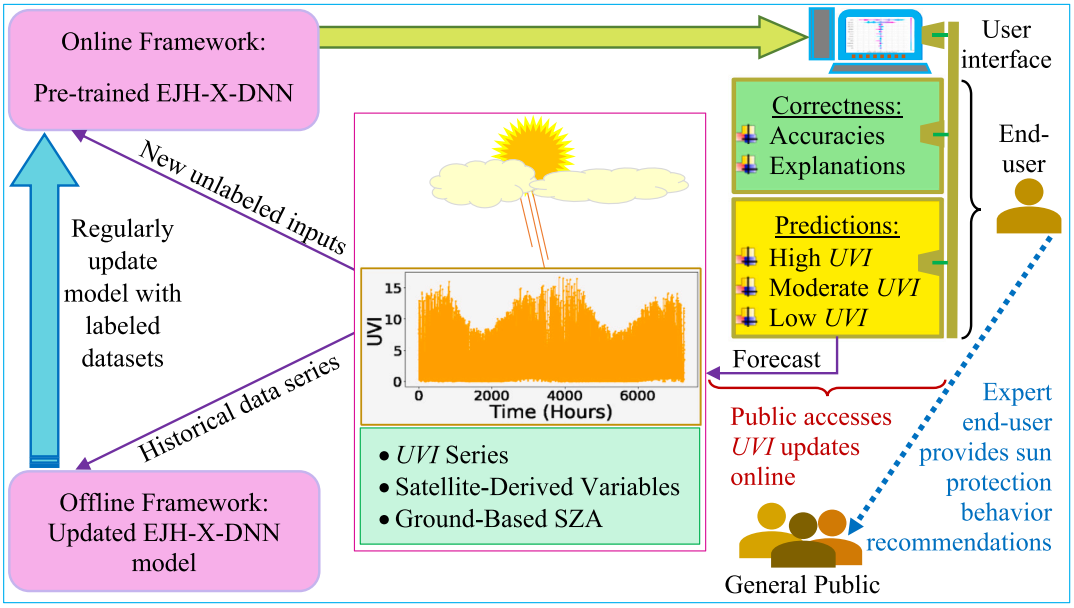

Fig. 10. Flowchart with real-life application of the online and offline hybrid explainable EJH-X-DNN framework in generating short-term UVI forecasts.

on the output and lead to completely different results. This is relevant in virtually all critical domains that are constrained by poor data quality due to a lack of expected independent and identically distributed (i.i.d.) datasets [70,71]. These limitations also affect the sensitive medical domain where AI-based predictive models suffer from low data quality. Consequently, the demand for trustworthy medical AI capable of explaining the "black-box" model outcomes has escalated considerably. In this regard, the regulatory requirements for AI applications in the medical domain that impacts human life have now made it mandatory to provide model explainability through traceability, transparency and interpretability capabilities [70]. On the same notion, it is imperative to include the ethical and legal aspects in the context of future trustworthy medical AI, so that all future AI-derived solutions are ethically responsible and legally compliant [71]. Explainability and robustness can promote reliability and confidence in results and enable human experts to remain in control. It ensures that human intelligence is complemented by artificial intelligence. For this purpose, the current study integrated remarkable xAI tools that enable the predictions of the newly designed DL "black-box" model to become more interpretable and trustworthy.

Though the newly constructed EJH-X-DNN model with satellite-derived predictors, ground-based SZA and lagged memory of *UVI* delivers promising forecasting capability and model explanations, future research can further boost its performance by incorporating real-time sky images as features that depict the stochastic cloud movements. Using the sky images, the temporal intermittent cloud cover effects can be extracted by integrating the merits of convolutional neural networks (CNNs) in some future research. Moreover, this research is contextualized primarily on short-term forecasting to successfully capture and predict the sudden escalated spikes of UV radiation. These spikes are led by partial cloud cover conditions that do not obscure the sun and can cause more severe skin damage with high risks of malignant keratinocyte cancer. If an investigation in the context of long-term forecasting is deemed important, future research could consider re-training the EJH-X-DNN model on long-term datasets.

6. Conclusions

Erythemally-effective UV radiation poses harmful exposure risks that can cause severe skin diseases such as malignant keratinocyte cancers and eye health ailments in humans. The engineering solutions provided by this study, in respect to developing an expert system that can deliver an accurate, reliable and trustworthy sun protection behaviour recommendations could be classified as an effective way to mitigate UV-exposure-related risks and provide benefits for the general public.

To address this serious issue, a hybrid explainable EJH-X-DNN model was constructed to forecast hourly ahead *UVI* for the four Australian hotspots that included Darwin, Alice Springs, Townsville and Emerald. The model was successfully trained and tested on satellite-derived and ground-based disparate datasets of the four sites. Through robust evaluation metrics and visual infographics, it was found that the prescribed model outperformed all the six benchmarked models in forecasting hourly *UVI*. The objective model displayed superior predictive performance for all four hotspots by capturing high values of r and *LME* with lower error values (i.e. *MAE* and *RMSE*). Through dual-phase feature selection and hyperparameter optimization by BO, the prediction capability of the newly designed *UVI* forecasting system was further enhanced. The model-agnostic LIME tool successfully offered instance-based local interpretations, while the SHAP and PFI frameworks were highly effective in delivering global explainability of *UVI* forecasts. In accordance with the combined interpretable outcomes of the local and global model-agnostic approaches, PACF1 (i.e. antecedent lagged memory of *UVI* at a lag of $t-1$) and solar zenith angle were found to be the major contributing predictor variables in forecasting short-term *UVI* for all four sites. It was also found that the feature attributes associated with ozone effects, cloud cover conditions and precipitation showed some significant impact on model predictions.

The newly designed hybrid explainable EJH-X-DNN model in this research can aid the end-users in decision-making to provide more accurate, transparent and credible *UVI* exposure risk information to the general public. The performance superiority and trustworthiness of this intelligent framework can potentially extend its practical utility as an early warning tool for UV exposure through an online or mobile mode for most temperate countries. This may also be advantageous for users situated in remote locations outside the range of the current ARPANSA network.

CRediT authorship contribution statement

Salvin S. Prasad: Conceptualization, Data curation, Formal analysis, Investigation, Methodology, Project administration, Resources, Software, Validation, Visualization, Writing – original draft, Writing – re-

view & editing. **Ravinesh C. Deo:** Project administration, Resources, Supervision, Writing – review & editing. **Sancho Salcedo-Sanz:** Resources, Writing – review & editing. **Nathan J. Downs:** Project administration, Resources, Supervision, Writing – review & editing. **David Casillas-Pérez:** Writing – review & editing. **Alfio V. Parisi:** Supervision, Writing – review & editing.

Declaration of competing interest

The authors declare that they have no known competing financial interests or personal relationships that could have appeared to influence the work reported in this paper.

Acknowledgement

This work is supported through the University of Southern Queensland (UniSQ) Postgraduate Research Scholarship awarded to the first author by the Graduate Research School (GRS) of UniSQ under Grant number 2020-2023. His research has also been partially supported by the project PID2020-115454GB-C21 of the Spanish Ministry of Science and Innovation (MICINN). Additionally, the authors are grateful to NASA GIOVANNI and ARPANSA for the data.

Appendix A. List of acronyms (Table A.1)

Table A.1
List of acronyms.

Acronym	Definition
AB	AdaBoost
AI	Artificial Intelligence
ANN	Artificial Neural Network
ARPANSA	Australian Radiation Protection and Nuclear Safety Agency
AUD	Australian Dollars
BO	Bayesian Optimizer
CNN	Convolution Neural Network
DL	Deep Learning
DNN	Deep Neural Network
DT	Decision Tree
ELU	Exponential Linear Unit
FCN	Fully Convolutional Network
FFBPN	Feed-Forward Back Propagation Network
GIOVANNI	Goddard Online Interactive Visualization and Analysis Infrastructure
GPU	Graphical Processing Unit
ICNIRP	International Commission on Non-Ionizing Radiation Protection
LIME	Local Interpretable Model-Agnostic Explanations
LME	Legate-Mccabe Efficiency Index
LSTM	Long Short-Term Memory
MAE	Mean Absolute Error
MERRA	Modern-Era Retrospective Analysis for Research and Applications
ML	Machine Learning
MLP	Multilayer Perceptrons
NT	Northern Territory
PACF	Partial Autocorrelation Function
PFI	Permutation Feature Importance
QLD	Queensland
r	Correlation
r	Pearson's Correlation Coefficient
r_{cross}	Cross-Correlation Coefficient
ReLU	Rectified Linear Unit
RF	Random Forest
RMSE	Root Mean Squared Error
SGD	Stochastic Gradient Descent
SHAP	Shapley Additive Explanations
SZA	Solar Zenith Angle
TPU	Tensor Processing Unit
UNEP	United Nations Environment Programme
UV	Solar Ultraviolet
UVI	Ultraviolet Index
WHO	World Health Organization
WMO	World Meteorological Organization
xAI	Explainable Artificial Intelligence

References

[1] A. Juzeniene, J. Moan, Beneficial effects of UV radiation other than via vitamin D production, Dermato-Endocrinol. 4 (2) (2012) 109–117.
[2] W. Hijnen, E. Beerendonk, G.J. Medema, Inactivation credit of UV radiation for viruses, bacteria and protozoan (oo)cysts in water: a review, Water Res. 40 (1) (2006) 3–22.
[3] C.S. Heilingloh, U.W. Aufderhorst, L. Schipper, U. Dittmer, O. Witzke, D. Yang, X. Zheng, K. Sutter, M. Trilling, M. Alt, et al., Susceptibility of SARS-CoV-2 to UV irradiation, Am. J. Infect. Control 48 (10) (2020) 1273–1275.
[4] E. Piri, M. Babaeian, A. Tavassoli, Y. Esmaeilian, et al., Effects of UV irradiation on plants, Afr. J. Microbiol. Res. 5 (14) (2011) 1710–1716.
[5] R.C. Deo, N. Downs, A.V. Parisi, J.F. Adamowski, J.M. Quilty, Very short-term reactive forecasting of the solar ultraviolet index using an extreme learning machine integrated with the solar zenith angle, Environ. Res. 155 (2017) 141–166.
[6] A. Kazantzidis, A. Smedley, R. Kift, J. Rimmer, J.L. Berry, L.E. Rhodes, A.R. Webb, A modeling approach to determine how much UV radiation is available across the UK and Ireland for health risk and benefit studies, Photochem. Photobiol. Sci. 14 (6) (2015) 1073–1081.
[7] J. Turner, D. Igoe, A.V. Parisi, A.J. McGonigle, A. Amar, L. Wainwright, A review on the ability of smartphones to detect ultraviolet (UV) radiation and their potential to be used in UV research and for public education purposes, Sci. Total Environ. 706 (2020) 135873.
[8] E.R. Parker, The influence of climate change on skin cancer incidence–a review of the evidence, Int J. Women's Dermatol. 7 (1) (2021) 17–27.
[9] L.G. Gordon, W. Leung, R. Johns, B. McNoe, D. Lindsay, K.M. Merollini, T.M. Elliott, R.E. Neale, C.M. Olsen, N. Pandeya, et al., Estimated healthcare costs of melanoma and keratinocyte skin cancers in Australia and aotearoa New Zealand in 2021, Int. J. Environ. Res. Public Health 19 (6) (2022) 3178.
[10] L. Gordon, S. Shih, C. Watts, D. Goldsbury, A. Green, The economics of skin cancer prevention with implications for Australia and New Zealand: where are we now?, Public Health Res. Pract. 32 (1) (2022).
[11] W.H. Organization, I.C. on Non-Ionizing Radiation Protection, et al., Global solar UV index: a practical guide, Tech. Rep., World Health Organization, 2002.
[12] G.H. Bernhard, R.E. Neale, P.W. Barnes, P. Neale, R.G. Zepp, S.R. Wilson, A.L. Andrady, A.F. Bais, R.L. McKenzie, P.J. Aucamp, et al., Environmental effects of stratospheric ozone depletion, UV radiation and interactions with climate change: UNEP environmental effects assessment panel, update 2019, Photochem. Photobiol. Sci. 19 (5) (2020) 542–584.
[13] H. Majidifard, Y. Adu-Gyamfi, W.G. Buttlar, Deep machine learning approach to develop a new asphalt pavement condition index, Constr. Build. Mater. 247 (2020) 118513.
[14] A.M. Ahmed, M.H. Ahmed, S.K. Saha, O. Ahmed, A. Sutradhar, Optimization algorithms as training approach with hybrid deep learning methods to develop an ultraviolet index forecasting model, Stoch. Environ. Res. Risk Assess. 36 (10) (2022) 3011–3039.
[15] S.S. Prasad, R.C. Deo, N. Downs, D. Igoe, A.V. Parisi, J. Soar, Cloud affected solar UV prediction with three-phase wavelet hybrid convolutional long short-term memory network multi-step forecast system, IEEE Access 10 (2022) 24704–24720.
[16] G. Vilone, L. Longo, Notions of explainability and evaluation approaches for explainable artificial intelligence, Inf. Fusion 76 (2021) 89–106.
[17] L.P. Joseph, E.A. Joseph, R. Prasad, Explainable diabetes classification using hybrid Bayesian-optimized tabnet architecture, Comput. Biol. Med. 151 (2022) 106178.
[18] M. Zdravković, I. Ćirić, M. Ignjatović, Explainable heat demand forecasting for the novel control strategies of district heating systems, Annu. Rev. Control (2022).
[19] R. Qin, L.K. Mahal, D. Bojar, Deep learning explains the biology of branched glycans from single-cell sequencing data, iScience 25 (10) (2022) 105163.
[20] M. Allaart, M. van Weele, P. Fortuin, H. Kelder, An empirical model to predict the UV-index based on solar zenith angles and total ozone, Meteorol. Appl. 11 (1) (2004) 59–65.
[21] F. Orte, E. Wolfram, J. Salvador, R. D'Elia, J. Quiroga, E. Quel, A. Mizuno, Attenuation by clouds of UV radiation for low stratospheric ozone conditions, in: AIP Conference Proceedings, vol. 1810, AIP Publishing LLC, 2017, p. 110009.
[22] U. Feister, G. Meyer, U. Kirst, Solar UV radiation exposure of seamen–measurements, calibration and model calculations of erythemal irradiance along ship routes, in: AIP Conference Proceedings, vol. 1531, American Institute of Physics, 2013, pp. 860–863.
[23] S. Ghimire, B. Bhandari, D. Casillas-Perez, R.C. Deo, S. Salcedo-Sanz, Hybrid deep CNN-SVR algorithm for solar radiation prediction problems in Queensland, Australia, Eng. Appl. Artif. Intell. 112 (2022) 104860.
[24] J.N. Latosińska, M. Latosińska, J. Bielak, Towards modelling ultraviolet index in global scale. Artificial neural networks approach, Aerosp. Sci. Technol. 41 (2015) 189–198.
[25] N.K. Chauhan, K. Singh, A review on conventional machine learning vs deep learning, in: 2018 International Conference on Computing, Power and Communication Technologies (GUCON), IEEE, 2018, pp. 347–352.
[26] F. Barboza, H. Kimura, E. Altman, Machine learning models and bankruptcy prediction, Expert Syst. Appl. 83 (2017) 405–417.
[27] P. Oliveira, B. Fernandes, C. Analide, P. Novais, Multi-step ultraviolet index forecasting using long short-term memory networks, in: Distributed Computing and Artificial Intelligence, 17th International Conference, Springer, 2021, pp. 187–197.

[28] M. Chaibi, E. Benghoulam, L. Tarik, M. Berrada, A.E. Hmaidi, An interpretable machine learning model for daily global solar radiation prediction, Energies 14 (21) (2021) 7367.
[29] T. Sim, S. Choi, Y. Kim, S.H. Youn, D.-J. Jang, S. Lee, C.-J. Chun, eXplainable AI (XAI)-based input variable selection methodology for forecasting energy consumption, Electronics 11 (18) (2022) 2947.
[30] R. Saleem, B. Yuan, F. Kurugollu, A. Anjum, L. Liu, Explaining deep neural networks: a survey on the global interpretation methods, Neurocomputing (2022).
[31] S.S. Amiri, S. Mottahedi, E.R. Lee, S. Hoque, Peeking inside the black-box: explainable machine learning applied to household transportation energy consumption, Comput. Environ. Urban Syst. 88 (2021) 101647.
[32] M.S. Islam, M.A. Awal, J.N. Laboni, F.T. Pinki, S. Karmokar, K.M. Mumenin, S. Al-Ahmadi, M.A. Rahman, M.S. Hossain, S. Mirjalili, HGSORF: Henry gas solubility optimization-based random forest for C-section prediction and XAI-based cause analysis, Comput. Biol. Med. 147 (2022) 105671.
[33] R. Machlev, L. Heistrene, M. Perl, K. Levy, J. Belikov, S. Mannor, Y. Levron, Explainable artificial intelligence (XAI) techniques for energy and power systems: review, challenges and opportunities, Energy and AI (2022) 100169.
[34] C. Chen, H. Jiang, Y. Zhang, Y. Wang, Investigating spatial and temporal characteristics of harmful algal bloom areas in the East China Sea using a fast and flexible method, in: 2010 18th International Conference on Geoinformatics, IEEE, 2010, pp. 1–4.
[35] G. Huang, X. Li, C. Huang, S. Liu, Y. Ma, H. Chen, Representativeness errors of point-scale ground-based solar radiation measurements in the validation of remote sensing products, Remote Sens. Environ. 181 (2016) 198–206.
[36] N. Downs, H. Butler, A. Parisi, Solar ultraviolet attenuation during the Australian (red dawn) dust event of 23 September 2009, Bull. Am. Meteorol. Soc. 97 (11) (2016) 2039–2050.
[37] F. Ochieng'Odhiambo, Comparative study of various methods of handling missing data, Math. Model. Appl. 5 (2) (2020) 87–93.
[38] J. Yang, X. Zou, W. Zhang, H. Han, Microblog sentiment analysis via embedding social contexts into an attentive LSTM, Eng. Appl. Artif. Intell. 97 (2021) 104048.
[39] F. Pedregosa, G. Varoquaux, A. Gramfort, V. Michel, B. Thirion, O. Grisel, M. Blondel, P. Prettenhofer, R. Weiss, V. Dubourg, et al., Scikit-learn: machine learning in python, J. Mach. Learn. Res. 12 (2011) 2825–2830.
[40] N. Ketkar, N. Ketkar, Introduction to keras, in: Deep Learning with Python: A Hands-on Introduction, 2017, pp. 97–111.
[41] M. Abadi, P. Barham, J. Chen, Z. Chen, A. Davis, J. Dean, M. Devin, S. Ghemawat, G. Irving, M. Isard, et al., Tensorflow: a system for large-scale machine learning, in: OSDI, Savannah, GA, USA, vol. 16, 2016, pp. 265–283.
[42] T.M. Inc., Matlab version: 9.13.0 (r2022b), https://www.mathworks.com, 2022.
[43] H. Dai, H.-G. Hwang, V.S. Tseng, Convolutional neural network based automatic screening tool for cardiovascular diseases using different intervals of ECG signals, Comput. Methods Programs Biomed. 203 (2021) 106035.
[44] M. Alebooyeh, R.J. Urbanic, Neural network model for identifying workspace, forward and inverse kinematics of the 7-DOF YuMi 14000 ABB collaborative robot, IFAC-PapersOnLine 52 (10) (2019) 176–181.
[45] S. Ghimire, R.C. Deo, N. Raj, J. Mi, Deep learning neural networks trained with modis satellite-derived predictors for long-term global solar radiation prediction, Energies 12 (12) (2019) 2407.
[46] O. Martinez, C. Martinez, C.A. Parra, S. Rugeles, D.R. Suarez, Machine learning for surgical time prediction, Comput. Methods Programs Biomed. 208 (2021) 106220.
[47] S. Hashem, M. ElHefnawi, S. Habashy, M. El-Adawy, G. Esmat, W. Elakel, A.O. Abdelazziz, M.M. Nabeel, A.H. Abdelmaksoud, T.M. Elbaz, et al., Machine learning prediction models for diagnosing hepatocellular carcinoma with HCV-related chronic liver disease, Comput. Methods Programs Biomed. 196 (2020) 105551.
[48] X. Luo, L.O. Oyedele, A.O. Ajayi, O.O. Akinade, H.A. Owolabi, A. Ahmed, Feature extraction and genetic algorithm enhanced adaptive deep neural network for energy consumption prediction in buildings, Renew. Sustain. Energy Rev. 131 (2020) 109980.
[49] A.T. Keleko, B. Kamsu-Foguem, R.H. Ngouna, A. Tongne, Health condition monitoring of a complex hydraulic system using Deep Neural Network and DeepSHAP explainable XAI, Adv. Eng. Softw. 175 (2023) 103339.
[50] S. Phithakkitnukooon, K. Patanukhom, M.G. Demissie, Predicting spatiotemporal demand of dockless e-scooter sharing services with a masked fully convolutional network, ISPRS Int.l J. Geo-Inf. 10 (11) (2021) 773.
[51] H.-H. Rau, C.-Y. Hsu, Y.-A. Lin, S. Atique, A. Fuad, L.-M. Wei, M.-H. Hsu, Development of a web-based liver cancer prediction model for type II diabetes patients by using an artificial neural network, Comput. Methods Programs Biomed. 125 (2016) 58–65.
[52] N. Shukla, M. Hagenbuchner, K.T. Win, J. Yang, Breast cancer data analysis for survivability studies and prediction, Comput. Methods Programs Biomed. 155 (2018) 199–208.
[53] L. Xiao, Y. Dong, Y. Dong, An improved combination approach based on adaboost algorithm for wind speed time series forecasting, Energy Convers. Manag. 160 (2018) 273–288.
[54] A.B. Nassif, Short term power demand prediction using stochastic gradient boosting, in: 2016 5th International Conference on Electronic Devices, Systems and Applications (ICEDSA), IEEE, 2016, pp. 1–4.
[55] M.M. Ghiasi, S. Zendehboudi, A.A. Mohsenipour, Decision tree-based diagnosis of coronary artery disease: cart model, Comput. Methods Programs Biomed. 192 (2020) 105400.
[56] S. Shin, Y. Lee, M. Kim, J. Park, S. Lee, K. Min, Deep neural network model with Bayesian hyperparameter optimization for prediction of nox at transient conditions in a diesel engine, Eng. Appl. Artif. Intell. 94 (2020) 103761.
[57] B. Shahriari, K. Swersky, Z. Wang, R.P. Adams, N. De Freitas, Taking the human out of the loop: a review of Bayesian optimization, Proc. IEEE 104 (1) (2015) 148–175.
[58] H.-P. Nguyen, J. Liu, E. Zio, A long-term prediction approach based on long short-term memory neural networks with automatic parameter optimization by Tree-structured Parzen Estimator and applied to time-series data of NPP steam generators, Appl. Soft Comput. 89 (2020) 106116.
[59] R. Martinez-Cantin, Bayesian optimization with adaptive kernels for robot control, in: 2017 IEEE International Conference on Robotics and Automation (ICRA), IEEE, 2017, pp. 3350–3356.
[60] M. Injadat, F. Salo, A.B. Nassif, A. Essex, A. Shami, Bayesian optimization with machine learning algorithms towards anomaly detection, in: 2018 IEEE Global Communications Conference (GLOBECOM), IEEE, 2018, pp. 1–6.
[61] E. Sharma, R.C. Deo, J. Soar, R. Prasad, A.V. Parisi, N. Raj, Novel hybrid deep learning model for satellite based PM10 forecasting in the most polluted Australian hotspots, Atmos. Environ. 279 (2022) 119111.
[62] M.T. Ribeiro, S. Singh, C. Guestrin, "Why should I trust you?" explaining the predictions of any classifier, in: Proceedings of the 22nd ACM SIGKDD International Conference on Knowledge Discovery and Data Mining, 2016, pp. 1135–1144.
[63] A. Agarwal, A. Bhatia, A. Malhi, P. Kaler, H.S. Pannu, et al., Machine learning based explainable financial forecasting, in: 2022 4th International Conference on Computer Communication and the Internet (ICCCI), IEEE, 2022, pp. 34–38.
[64] M. Kuzlu, U. Cali, V. Sharma, Ö. Güler, Gaining insight into solar photovoltaic power generation forecasting utilizing explainable artificial intelligence tools, IEEE Access 8 (2020) 187814–187823.
[65] A.E. Roth, The Shapley Value: Essays in Honor of Lloyd S. Shapley, Cambridge University Press, 1988.
[66] Z. Li, Extracting spatial effects from machine learning model using local interpretation method: an example of SHAP and XGBoost, Comput. Environ. Urban Syst. 96 (2022) 101845.
[67] Z. Jiang, L. Bo, Z. Xu, Y. Song, J. Wang, P. Wen, X. Wan, T. Yang, X. Deng, J. Bian, An explainable machine learning algorithm for risk factor analysis of in-hospital mortality in sepsis survivors with ICU readmission, Comput. Methods Programs Biomed. 204 (2021) 106040.
[68] R. Taghizadeh-Mehrjardi, N. Hamzehpour, M. Hassanzadeh, B. Heung, M.G. Goydaragh, K. Schmidt, T. Scholten, Enhancing the accuracy of machine learning models using the super learner technique in digital soil mapping, Geoderma 399 (2021) 115108.
[69] R.O. Alabi, A. Almangush, M. Elmusrati, I. Leivo, A.A. Mäkitie, An interpretable machine learning prognostic system for risk stratification in oropharyngeal cancer, Int. J. Med. Inform. 168 (2022) 104896.
[70] A. Holzinger, The next frontier: AI we can really trust, in: Joint European Conference on Machine Learning and Knowledge Discovery in Databases, Springer, 2021, pp. 427–440.
[71] A. Holzinger, M. Dehmer, F. Emmert-Streib, R. Cucchiara, I. Augenstein, J. Del Ser, W. Samek, I. Jurisica, N. Díaz-Rodríguez, Information fusion as an integrative cross-cutting enabler to achieve robust, explainable, and trustworthy medical artificial intelligence, Inf. Fusion 79 (2022) 263–278.

6.3. **Implications**

The newly constructed enhanced joint hybrid explainable model, denoted as EJH-X-DNN demonstrates remarkable performance in forecasting hourly ahead UVI. Alongside the competing counterpart models, the prescribed predictive model is the most superior forecasting system as its evaluation validates high-performance efficiencies with all the performance measurement criteria for each of the four Australian hotspots of Darwin, Alice Springs, Townsville and Emerald. The integration of xAI tools robustly offers explanations on the predictive contributions of the input predictor variables. The collective interpretable outcomes using the model-agnostic tools reveal that the antecedent memory of UVI behaviour (at a lag of t - 1) and SZA had the most influence in predicting the hourly UVI for all four sites. The variables of cloud cover conditions and precipitation also showed some significant contributions towards the model predictions.

The explainable outcomes and robust forecasting performance of the data-intelligent model ascertain its practical utility as an early warning tool in forecasting UVI for most temperate countries, including remote regions. The proposed model is trained on some important atmospheric variables, including cloud cover conditions with aerosol and ozone effects, which further affirms its applicability to other geographical locations that receive high solar UV radiation. Thus, the newly developed model is a likely tool to be adopted in real-life applications for benefiting the end-users (including UV researchers), by delivering more accurate and explainable UV radiation exposure information. The implementation of this robust UV radiation monitoring framework can help mitigate the subsequent harmful UV exposure risks for the general public, and terrestrial animal and plant life. Moreover, the highly accurate UV radiation forecasts and explainable outcomes generated by this novel predictive model can guide policymakers in the health sector to mitigate skin-based malignant keratinocyte cancers and eye health ailments that include cataracts and pterygium.

CHAPTER 7: CONCLUSIONS AND FUTURE SCOPE

7.1. Synthesis and important findings

This study attempts to advance the technology of solar UV radiation prediction by constructing an accurate and high-precision AI-inspired forecasting framework using the hybridized approach. In this regard, UV radiation is predicted in terms of the UVI and the UV-A waveband at short-term forecast horizons for selected hotspots in the state of Queensland and the Northern Territory receiving high UV exposure. For the two regions, the specifically focused hotspots for validating the newly developed UV radiation forecasting systems include the Toowoomba experiment site, Townsville, Emerald, Darwin and Alice Springs. Given the complexity and intermittency of ground-level UV radiation phenomena, a diverse range of hybridized ML and DL algorithms were implemented by integrating several ground-based and satellite-derived atmospheric variables. Fundamentally, the predictive framework constructed using the hybridized approach is highly beneficial to the end-users, as the hybrid models would be self-adaptive and require minimal human interaction to generate accurate forecasts of UV radiation. The findings of this study can offer new decision support tools designed through a hybridized approach to provide more accurate, reliable and explainable UV-exposure information to expert end-users, including the general public and UV researchers.

The research study addresses some important modelling issues in designing hybridized UV radiation forecasting systems. The first concern was regarding the selection of pertinent predictors from sets of multivariate inputs in UV radiation forecasting. To resolve this problem, the study applied remarkable feature selection algorithms, such as BorutaShap, NCA, model-specific RF model and filter-based methods. Secondly, the issue of non-stationarity and non-linearity in the UV-radiation predictor variables was another important concern. This modelling constraint was addressed by implementing an effective data decomposition approach using SWT. Moreover, the complex and non-linear relationships between the feature variables with large datasets could lead to overfitting issues during the training phase of the UV radiation forecasting framework. To overcome this modelling limitation, the DL technologies were employed in constructing the proposed models for the different objectives. Another important modelling component was the calibration of the DL model and quantifying the uncertainty to enhance model performance and reliability.

For this purpose, the study adopted an ensemble modelling strategy by training several single-point DL models on three different key loss functions to enable model calibration. Additionally, the DL models have a “black-box” architecture and the predictive outcomes are generated through highly complex and non-explainable hidden internal workings. To overcome the model explainability issues, the DL models were integrated with model-agnostic xAI tools.

The findings of this research revealed that hybridized DL models showed improved performance against the competing counterpart models in forecasting short-term UV radiation. The outcomes from objective 1 (Chapter 4) demonstrate the capability of a wavelet hybrid convLSTM predictive system (designated as W-O-convLSTM) to emulate UVI forecasting under the influence of intermittent cloud cover conditions. In accordance with the results, the improved performance was achieved by implementing the BorutaShap algorithm, which was an important feature selection tool that efficiently identified the most informative predictor variables from the set of the sky image-based cloud statistical properties and SZA to model UVI. The high-frequency and low-frequency components of the input variables extracted through the SWT data decomposition tool also enhanced the performance of the predictive model, as the results reveal superior forecasting performance by the wavelet-based models against the non-wavelet-based counterparts. The incorporation of the Optuna hyperparameter algorithm indicated further improvement in the predicted outcomes of UVI at multistep horizons (i.e., 10-minute, 20-minute, 30-minute and hourly time scales). In this respect, forecasts generated at shorter time spans were more precise, as the longer forecast horizons captured slightly lower accuracies. The newly prescribed multiple input multi-step output model can robustly be applied to forecast cloud-affected UVI for regions close to the Toowoomba-based experimental site.

The study from objective 2 (Chapter 5) exemplified the performance superiority of the hybrid ensemble N-BEATS predictive framework (designated as B-E-NBEATS) in forecasting short-term UV-A radiation at a 20-minute horizon. The outcomes from this study served as a milestone for the future influence of harmful UV-A exposure on people and terrestrial plant and animal life. By embedding the NCA algorithm for feature selection, the proposed high-performing model registered superior forecasting accuracies with respect to the benchmarked models. The results of the findings further reveal that the successful hyperparameter optimization using a remarkable Bayesian optimizer enabled the prescribed data-intelligent model to deliver the best forecasting

capability in all four seasons of spring, summer, autumn and winter. Additionally, the proposed ensemble model with hybridized architecture also generated interpretable outcomes in terms of seasonality and trend components by integrating N-BEATS as the base model. The overall performance enhancement and more reliable forecasts were achieved through the calibration and uncertainty quantification of the proposed ensemble model trained on different key loss functions. Therefore, the newly developed UV-A forecasting model through its robust performance capability consolidates its future applications for Toowoomba, as well as in other regions including tropical and sub-tropical countries.

The findings of the study conducted in objective 3 reveal the robustness and trustworthiness of an enhanced joint hybrid explainable DNN model (designated as EJH-X-DNN) as an early warning tool to forecast ground-level UVI at the hourly horizon. The outcomes of precise forecasts and model explainability can aid expert end-users in making better decisions to implement sun protection. High forecasting accuracies were captured by the proposed model by incorporating a dual-phase feature selection approach, which included model-agnostic random forest and filter-based techniques. Further enhancement in the accuracies of the model predictions was achieved by coupling the model architecture with a powerful Bayesian optimizer that fine-tuned the model hyperparameters. To promote reliability and confidence in the results, the study further integrated the model-agnostic xAI tools that offered the explainability of the model outcomes along with robustness. By deploying trustworthy AI using the xAI tools of LIME, SHAP and PFI, the study ensured that human intelligence is effectively complemented by artificial intelligence. The prescribed model constructed using satellite-derived variables, significant antecedent memory of UVI behaviour and ground-based SZA demonstrated superior performance for all the four Australian hotspots of Darwin, Alice Springs, Townsville and Emerald that receive high UV radiation exposure. For all four hotspots, the aggregated local and global model-agnostic explanations indicate that the antecedent lagged memory of UVI (at a lag of t - 1) and SZA are impactful features in generating the predictive outcomes. In addition, the model outcomes are also influenced by the atmospheric factors of the ozone effect, cloud cover conditions, and precipitation. The explainability and robustness of the newly designed UVI forecasting framework integrated with trustworthy AI can potentially extend its practical utility as an early warning system to provide more accurate sun protection information to the general public and UV radiation researchers

to help mitigate UV-exposure-related skin cancers and eye health ailments. On this notion, the performance superiority and trustworthiness of this intelligent predictive model trained on important atmospheric variables (including cloud cover conditions with aerosol and ozone effects) further consolidate its applications in different Australian domains, as well as in other tropical and sub-tropical countries. Additionally, the newly designed hybridized predictive models can also be integrated into advanced forecasting software for mobile devices, such as smartphones to offer real-time UV radiation exposure information to the general public at different geographical locations.

In summary, the construction of intelligent predictive models for forecasting ground-level UV radiation offered some novel contributions. The findings of the study through the results reveal that the hybridized versions of various prescribed models delivered relatively better forecasting performance alongside the comparative counterparts. Thus, after exploring the new innovative approaches, the major contributions of this research are summarized as follows:

- The study investigated some previously unexplored methodologies using hybridized DL technologies in forecasting ground-level UVI for the Toowoomba experimental site, as well as for other Australian hotspots of Darwin, Alice Springs, Townsville and Emerald that receive high solar UV radiation exposure.
- An efficient image segmentation algorithm developed in this study robustly extracted the cloud statistical properties (that depicted cloud cover effects) from sky images.
- In developing the predictive model, the study integrated the sky image-derived cloud statistical properties to forecast UV radiation for the Toowoomba study site. For the other Australian hotspots, the study applied important atmospheric variables derived from next-generation satellite platforms.
- The newly developed hybrid DL models incorporated SWT and augmented the Dickey-Fuller test to address the modelling flaws led by non-stationarity in the input data.
- The general goal of improving the forecasting performance was accomplished by integrating powerful feature selection algorithms that include BorutaShap, NCA, model-specific random forest method and filter-based techniques.

- Remarkable hyperparameter fine-tuning algorithms, such as Optuna and Bayesian optimizer embedded into the design architecture of the DL predictive models optimized the forecasting efficiency.
- The calibration and uncertainty quantification of the newly constructed hybrid ensemble model further enhanced the forecasting performance and model reliability.
- The predictive behaviour of the hybridized DL model in forecasting UV radiation was explained for the first time by integrating model-agnostic xAI tools, where LIME was used to explain the model outcomes at the local level, while SHAP and PFI were used for explanations at the global level.
- The application of remarkable xAI tools aided the predictions of UV radiation by the newly designed DL "black-box" model to become more interpretable and trustworthy.
- The accurate and interpretable forecasts of short-term UV radiation by the newly constructed DL models can facilitate the end-users to offer more accurate sun protection information to the general public and UV radiation researchers.
- Finally, the novel hybrid UV radiation forecasting system constructed in this study can be applied as an early warning tool to help mitigate UV-exposure-related skin and eye diseases, consequently minimizing the growing economic burden on healthcare services.

7.2. **Limitations of the current study and recommendations for future research**

The robustness and promising outcomes of the hybrid UV radiation forecasting models constructed using innovative technological approaches can offer the scientific pathway for integrated on-site decision-support framework to facilitate the health care systems with UV-exposure risk information for the people and to monitor the UV-exposure effects on terrestrial life. However, the study elucidates some minor limitations of these data-intelligent models, which can slightly influence their practical applications.

- Due to the unavailability of actual ozone and aerosol datasets at 10-minute time resolution, the Toowoomba-based UVI and UV-A forecasting models designed using sky image-derived cloud statistical properties used time-lagged Bentham

UVI datasets that already captured some ozone and aerosol effects. However, future studies can integrate the actual measured values of aerosol and ozone effects together with sky image-derived cloud cover effects to forecast ground-level UV radiation.

- This study is contextualized primarily to the short-term forecast horizon for efficient capturing and prediction of the suddenly escalated spikes in UV radiation led by partial cloud cover conditions that do not obscure the sun. Future research could consider re-training the newly constructed hybrid DL models on long-term datasets should an investigation in the context of long-term prediction of UV radiation be deemed important.
- The study integrated cloud statistical properties extracted from the sky images as predictor inputs during the model designing phase. To further boost the forecasting performance, the technique of transfer learning with pre-trained models having CNN-based architecture can be applied to extract the important features from the time-dependent sky images.
- In designing the UV radiation predictive models as early warning UV-exposure tools, the study explored forecasts of UVI and UV-A radiation. In some future research, both UV-A and UV-B radiation forecasting tools can be constructed side-by-side by integrating the xAI tools to explain the contributions of different atmospheric variables towards predicting the UV-A and UV-B radiation, respectively.
- Future studies can also address the spatiotemporal dependency of stations and atmospheric variables in modelling UV radiation, as the nearby stations can contribute pertinent information towards extracting important features.

In closing, this PhD research has made some novel contributions towards addressing the challenges confronted in forecasting ground-level solar UV radiation using DL data-intelligent technologies. These newly constructed predictive frameworks implemented using a hybridized approach are easy to apply and display high computational efficiency with low latency in forecasting UV radiation at short-term horizons. The performance robustness and capability to provide explainable model outcomes affirm that the hybrid UV radiation predicting system developed in this study can serve as an early warning tool to deliver more accurate sun protection behaviour

recommendations to the general public and help mitigate skin-based cancers and eye diseases in humans. Concurrently, this newly developed predictive system can also aid UV radiation researchers as an important decision-support instrument to explore the detrimental UV exposure risks on terrestrial animals and plants to benefit the agricultural sector.

REFERENCES

Ahmed, AAM, Ahmed, MH, Saha, SK, Ahmed, O & Sutradhar, A 2022, 'Optimization algorithms as training approach with hybrid deep learning methods to develop an ultraviolet index forecasting model', *Stochastic Environmental Research and Risk Assessment*, vol. 36, pp. 3011-39.

Ahmed, AM, Deo, RC, Raj, N, Ghahramani, A, Feng, Q, Yin, Z & Yang, L 2021, 'Deep learning forecasts of soil moisture: convolutional neural network and gated recurrent unit models coupled with satellite-derived MODIS, observations and synoptic-scale climate index data', *Remote Sensing*, vol. 13, no. 4, pp. 1-30.

Al-Musaylh, MS, Deo, RC & Li, Y 2020, 'Electrical energy demand forecasting model development and evaluation with maximum overlap discrete wavelet transform-online sequential extreme learning machines algorithms', *Energies*, vol. 13, no. 9, pp. 2-19.

Alabi, RO, Almangush, A, Elmusrati, M, Leivo, I & Mäkitie, AA 2022, 'An interpretable machine learning prognostic system for risk stratification in oropharyngeal cancer', *International Journal of Medical Informatics*, vol. 168, pp. 1-12.

Alados, I, Gomera, M, Foyo-Moreno, I & Alados-Arboledas, L 2007, 'Neural network for the estimation of UV erythemal irradiance using solar broadband irradiance', *International Journal of Climatology: A Journal of the Royal Meteorological Society*, vol. 27, no. 13, pp. 1791-9.

Allaart, M, van Weele, M, Fortuin, P & Kelder, H 2004, 'An empirical model to predict the UV-index based on solar zenith angles and total ozone', *Meteorological Applications*, vol. 11, no. 1, pp. 59-65.

Aun, M, Eerme, K, Ansko, I, Veismann, U & Lätt, S 2011, 'Modification of spectral ultraviolet doses by different types of overcast cloudiness and atmospheric aerosol', *Photochemistry and Photobiology*, vol. 87, no. 2, pp. 461-9.

Barboza, F, Kimura, H & Altman, E 2017, 'Machine learning models and bankruptcy prediction', *Expert Systems with Applications*, vol. 83, pp. 405-17.

Bernhard, GH, Neale, RE, Barnes, PW, Neale, P, Zepp, RG, Wilson, SR, Andrady, AL, Bais, AF, McKenzie, RL & Aucamp, PJ 2020, 'Environmental effects of stratospheric ozone depletion, UV radiation and interactions with climate change: UNEP Environmental Effects Assessment Panel, update 2019', *Photochemical & Photobiological Sciences*, vol. 19, no. 5, pp. 542-84.

Bolón-Canedo, V, Sánchez-Maroño, N & Alonso-Betanzos, A 2015, 'Recent advances and emerging challenges of feature selection in the context of big data', *Knowledge-Based Systems*, vol. 86, pp. 33-45.

Chaibi, M, Benghoulam, E, Tarik, L, Berrada, M & Hmaidi, AE 2021, 'An interpretable machine learning model for daily global solar radiation prediction', *Energies*, vol. 14, no. 21, pp. 1-19.

Chauhan, NK & Singh, K 2018, 'A review on conventional machine learning vs deep learning', *2018 International Conference on Computing, Power and Communication Technologies (GUCON)*, IEEE, pp. 347-52.

Chen, C, Jiang, H, Zhang, Y & Wang, Y 2010, 'Investigating spatial and temporal characteristics of harmful Algal Bloom areas in the East China Sea using a fast and flexible method', *2010 18th International Conference on Geoinformatics*, IEEE, pp. 1-4.

Chen, C, Xu, H, Wang, W, Li, B, Li, B, Chen, L & Zhang, G 2021, 'Communication-efficient federated learning with adaptive parameter freezing', *2021 IEEE 41st International Conference on Distributed Computing Systems (ICDCS)*, IEEE, pp. 1-11.

Cheng, H, Ding, X, Zhou, W & Ding, R 2019, 'A hybrid electricity price forecasting model with Bayesian optimization for German energy exchange', *International Journal of Electrical Power & Energy Systems*, vol. 110, pp. 653-66.

Courdavault, S, Baudouin, C, Charveron, M, Favier, A, Cadet, J & Douki, T 2004, 'Larger yield of cyclobutane dimers than 8-oxo-7, 8-dihydroguanine in the DNA of UVA-irradiated human skin cells', *Mutation Research/Fundamental and Molecular Mechanisms of Mutagenesis*, vol. 556, no. 1-2, pp. 135-42.

Cui, Z, Ke, R, Pu, Z & Wang, Y 2020, 'Stacked bidirectional and unidirectional LSTM recurrent neural network for forecasting network-wide traffic state with missing values', *Transportation Research Part C: Emerging Technologies*, vol. 118, pp. 1-14.

DeBuys, HV, Levy, SB, Murray, JC, Madey, DL & Pinnell, SR 2000, 'Modern approaches to photoprotection', *Dermatologic Clinics*, vol. 18, no. 4, pp. 577-90.

Deo, RC, Downs, N, Parisi, AV, Adamowski, JF & Quilty, JM 2017, 'Very short-term reactive forecasting of the solar ultraviolet index using an extreme learning machine integrated with the solar zenith angle', *Environmental Research*, vol. 155, pp. 141-66.

Dexter, B, King, R, Parisi, A, Harrison, S, Konovalov, D & Downs, N 2020, 'Keratinocyte skin cancer risks for working school teachers: scenarios and implications of the timing of scheduled duty periods in Queensland, Australia', *Journal of Photochemistry and Photobiology B: Biology*, vol. 213, pp. 1-10.

Diffey, B, Larkö, O & Swanbeck, G 1982, 'UV-B doses received during different outdoor activities and UV-B treatment of psoriasis', *British Journal of Dermatology*, vol. 106, no. 1, pp. 33-41.

Downs, N, Butler, H & Parisi, A 2016, 'Solar ultraviolet attenuation during the Australian (Red Dawn) dust event of 23 September 2009', *Bulletin of the American Meteorological Society*, vol. 97, no. 11, pp. 2039-50.

e Silva, PCdL, Junior, CAS, Alves, MA, Silva, R, Cohen, MW & Guimarães, FG 2020, 'Forecasting in non-stationary environments with fuzzy time series', *Applied Soft Computing*, vol. 97, pp. 1-12.

Ghiasi, MM, Zendehboudi, S & Mohsenipour, AA 2020, 'Decision tree-based diagnosis of coronary artery disease: CART model', *Computer Methods and Programs in Biomedicine*, vol. 192, pp. 1-14.

Ghimire, S, Deo, RC, Raj, N & Mi, J 2019a, 'Deep learning neural networks trained with MODIS satellite-derived predictors for long-term global solar radiation prediction', *Energies*, vol. 12, no. 12, pp. 1-39.

Ghimire, S, Deo, RC, Raj, N & Mi, J 2019b, 'Deep solar radiation forecasting with convolutional neural network and long short-term memory network algorithms', *Applied Energy*, vol. 253, pp. 1-20.

Ghimire, S, Bhandari, B, Casillas-Perez, D, Deo, RC & Salcedo-Sanz, S 2022, 'Hybrid deep CNN-SVR algorithm for solar radiation prediction problems in Queensland, Australia', *Engineering Applications of Artificial Intelligence*, vol. 112, pp. 1-26.

Ghosh, I & Chaudhuri, TD 2022, 'Integrating Navier-Stokes equation and neoteric iForest-BorutaShap-Facebook's prophet framework for stock market prediction: An application in Indian context', *Expert Systems with Applications*, vol. 210, pp. 1-19.

Gordon, L, Shih, S, Watts, C, Goldsbury, D & Green, A 2022, 'The economics of skin cancer prevention with implications for Australia and New Zealand: where are we now?', *Public Health Research & Practice*, vol. 32, no. 1, pp. 1-5.

Gordon, L, Leung, W, Johns, R, McNoe, B, Lindsay, D, Merollini, KM, Elliott, TM, Neale, RE, Olsen, CM & Pandeya, N 2022, 'Estimated Healthcare Costs of Melanoma and Keratinocyte Skin Cancers in Australia and Aotearoa New Zealand in 2021', *International Journal of Environmental Research and Public Health*, vol. 19, no. 6, pp. 1-14.

Hanifi, S, Lotfian, S, Zare-Behtash, H & Cammarano, A 2022, 'Offshore wind power forecasting—A new hyperparameter optimisation algorithm for deep learning models', *Energies*, vol. 15, no. 19, pp. 1-21.

Heilingloh, CS, Aufderhorst, UW, Schipper, L, Dittmer, U, Witzke, O, Yang, D, Zheng, X, Sutter, K, Trilling, M & Alt, M 2020, 'Susceptibility of SARS-CoV-2 to UV irradiation', *American Journal of Infection Control*, vol. 48, no. 10, pp. 1273-5.

Hijnen, W, Beerendonk, E & Medema, GJ 2006, 'Inactivation credit of UV radiation for viruses, bacteria and protozoan (oo) cysts in water: a review', *Water Research*, vol. 40, no. 1, pp. 3-22.

Hu, Z, Bao, Y, Xiong, T & Chiong, R 2015, 'Hybrid filter–wrapper feature selection for short-term load forecasting', *Engineering Applications of Artificial Intelligence*, vol. 40, pp. 17-27.

Igoe, D, Parisi, A & Carter, B 2013, 'Characterization of a smartphone camera's response to ultraviolet A radiation', *Photochemistry and Photobiology*, vol. 89, no. 1, pp. 215-8.

Indolia, S, Goswami, AK, Mishra, SP & Asopa, P 2018, 'Conceptual understanding of convolutional neural network-a deep learning approach', *Procedia Computer Science*, vol. 132, pp. 679-88.

Islam, MS, Awal, MA, Laboni, JN, Pinki, FT, Karmokar, S, Mumenin, KM, Al-Ahmadi, S, Rahman, MA, Hossain, MS & Mirjalili, S 2022, 'HGSORF: Henry Gas Solubility Optimization-based Random Forest for C-Section prediction and XAI-based cause analysis', *Computers in Biology and Medicine*, vol. 147, pp. 1-14.

Jayasinghe, WLP, Deo, RC, Ghahramani, A, Ghimire, S & Raj, N 2021, 'Deep multi-stage reference evapotranspiration forecasting model: Multivariate empirical mode decomposition integrated with the boruta-random forest algorithm', *IEEE Access*, vol. 9, pp. 166695-708.

Jayasinghe, WLP, Deo, RC, Ghahramani, A, Ghimire, S & Raj, N 2022, 'Development and evaluation of hybrid deep learning long short-term memory network model for pan evaporation estimation trained with satellite and ground-based data', *Journal of Hydrology*, vol. 607, pp. 1-19.

Joseph, LP, Joseph, EA & Prasad, R 2022, 'Explainable diabetes classification using hybrid Bayesian-optimized TabNet architecture', *Computers in Biology and Medicine*, vol. 151, pp. 1-22.

Juzeniene, A & Moan, J 2012, 'Beneficial effects of UV radiation other than via vitamin D production', *Dermato-Endocrinology*, vol. 4, no. 2, pp. 109-17.

Keleko, AT, Kamsu-Foguem, B, Ngouna, RH & Tongne, A 2023, 'Health condition monitoring of a complex hydraulic system using Deep Neural Network and DeepSHAP explainable XAI', *Advances in Engineering Software*, vol. 175, pp. 1-20.

Koskela, T, Heikkilä, A, Kaurola, J, Lindfors, A, Tanskanen, A & den Outer, P 2006, 'Spectral solar UV monitoring: worth it?', *Remote Sensing of Clouds and the Atmosphere XI*, SPIE, pp. 534-47.

Kudish, A, Lyubansky, V, Evseev, E & Ianetz, A 2005, 'Inter-comparison of the solar UVB, UVA and global radiation clearness and UV indices for Beer Sheva and Neve Zohar (Dead Sea), Israel', *Energy*, vol. 30, no. 9, pp. 1623-41.

Lakshminarayanan, B, Pritzel, A & Blundell, C 2017, 'Simple and scalable predictive uncertainty estimation using deep ensembles', *Advances in Neural Information Processing Systems*, vol. 30, pp. 1-12.

Latosińska, JN, Latosińska, M & Bielak, J 2015, 'Towards modelling ultraviolet index in global scale. Artificial neural networks approach', *Aerospace Science and Technology*, vol. 41, pp. 189-98.

Lavker, RM, Gerberick, GF, Veres, D, Irwin, CJ & Kaidbey, KH 1995, 'Cumulative effects from repeated exposures to suberythemal doses of UVB and UVA in human skin', *Journal of the American Academy of Dermatology*, vol. 32, no. 1, pp. 53-62.

Lee, SW & Kim, HY 2020, 'Stock market forecasting with super-high dimensional time-series data using ConvLSTM, trend sampling, and specialized data augmentation', *Expert Systems with Applications*, vol. 161, pp. 1-20.

Machlev, R, Heistrene, L, Perl, M, Levy, K, Belikov, J, Mannor, S & Levron, Y 2022, 'Explainable Artificial Intelligence (XAI) techniques for energy and power systems: Review, challenges and opportunities', *Energy and AI*, pp. 1-13.

Moishin, M, Deo, RC, Prasad, R, Raj, N & Abdulla, S 2021, 'Designing deep-based learning flood forecast model with ConvLSTM hybrid algorithm', *IEEE Access*, vol. 9, pp. 50982-93.

Moosavi, SHS & Bardsiri, VK 2017, 'Satin bowerbird optimizer: A new optimization algorithm to optimize ANFIS for software development effort estimation', *Engineering Applications of Artificial Intelligence*, vol. 60, pp. 1-15.

Morid, MA, Sheng, ORL, Kawamoto, K & Abdelrahman, S 2020, 'Learning hidden patterns from patient multivariate time series data using convolutional neural networks: A case study of healthcare cost prediction', *Journal of Biomedical Informatics*, vol. 111, pp. 1-11.

Okut, H, Wu, X-L, Rosa, GJ, Bauck, S, Woodward, BW, Schnabel, RD, Taylor, JF & Gianola, D 2013, 'Predicting expected progeny difference for marbling score in Angus cattle using artificial neural networks and Bayesian regression models', *Genetics Selection Evolution*, vol. 45, no. 1, pp. 1-13.

Olarte Saucedo, M, Sánchez Rodríguez, SH, Arechiga Flores, CF, Banuelos Valenzuela, R & López Luna, MA 2019, 'Effects of ultraviolet radiation (UV) in domestic animals. Review', *Revista Mexicana De Ciencias Pecuarias*, vol. 10, no. 2, pp. 416-32.

Oliveira, P, Fernandes, B, Analide, C & Novais, P 2020, 'Multi-step ultraviolet index forecasting using long short-term memory networks', *International Symposium on Distributed Computing and Artificial Intelligence*, Springer, pp. 187-97.

Oreshkin, BN, Carpov, D, Chapados, N & Bengio, Y 2019, 'N-BEATS: Neural basis expansion analysis for interpretable time series forecasting', *arXiv preprint arXiv:1905.10437*, pp. 1-31.

Ospina, J, Newaz, A & Faruque, MO 2019, 'Forecasting of PV plant output using hybrid wavelet-based LSTM-DNN structure model', *IET Renewable Power Generation*, vol. 13, no. 7, pp. 1087-95.

Parisi, AV & Kimlin, MG 1999, 'Horizontal and sun-normal spectral biologically effective ultraviolet irradiances', *Journal of Photochemistry and Photobiology B: Biology*, vol. 53, no. 1-3, pp. 70-4.

Parisi, AV, Turnbull, DJ & Kimlin, MG 2007, 'Dosimetric and Spectroradiometric Investigations of Glass-Filtered Solar UV', *Photochemistry and Photobiology*, vol. 83, no. 4, pp. 777-81.

Parisi, AV, Kimlin, MG, Lester, R & Turnbull, D 2003, 'Lower body anatomical distribution of solar ultraviolet radiation on the human form in standing and sitting postures', *Journal of Photochemistry and Photobiology B: Biology*, vol. 69, no. 1, pp. 1-6.

Parker, ER 2021, 'The influence of climate change on skin cancer incidence–A review of the evidence', *International Journal of Women's Dermatology*, vol. 7, no. 1, pp. 17-27.

Paul, ND & Gwynn-Jones, D 2003, 'Ecological roles of solar UV radiation: towards an integrated approach', *Trends in Ecology & Evolution*, vol. 18, no. 1, pp. 48-55.

Pecenak, ZK, Mejia, FA, Kurtz, B, Evan, A & Kleissl, J 2016, 'Simulating irradiance enhancement dependence on cloud optical depth and solar zenith angle', *Solar Energy*, vol. 136, pp. 675-81.

Petch, J, Di, S & Nelson, W 2022, 'Opening the black box: the promise and limitations of explainable machine learning in cardiology', *Canadian Journal of Cardiology*, vol. 38, no. 2, pp. 204-13.

Phithakkitnukooon, S, Patanukhom, K & Demissie, MG 2021, 'Predicting spatiotemporal demand of dockless e-scooter sharing services with a masked fully convolutional network', *ISPRS International Journal of Geo-Information*, vol. 10, no. 11, pp. 1-17.

Pirbazari, AM, Chakravorty, A & Rong, C 2019, 'Evaluating feature selection methods for short-term load forecasting', *2019 IEEE International Conference on Big Data and Smart Computing (BigComp)*, IEEE, pp. 1-8.

Piri, E, Babaeian, M, Tavassoli, A & Esmaeilian, Y 2011, 'Effects of UV irradiation on plants', *African Journal of Microbiology Research*, vol. 5, no. 14, pp. 1710-6.

Prasad, R, Deo, RC, Li, Y & Maraseni, T 2018, 'Ensemble committee-based data intelligent approach for generating soil moisture forecasts with multivariate hydro-meteorological predictors', *Soil and Tillage Research*, vol. 181, pp. 63-81.

Putatunda, S & Rama, K 2019, 'A modified bayesian optimization based hyper-parameter tuning approach for extreme gradient boosting', *2019 Fifteenth International Conference on Information Processing (ICINPRO)*, IEEE, pp. 1-6.

Qin, R, Mahal, LK & Bojar, D 2022, 'Deep learning explains the biology of branched glycans from single-cell sequencing data', *Iscience*, vol. 25, no. 10, pp. 1-22.

Rajput, UK, Kumar, R & Kumar, G 2015, 'Comparison between discrete wavelet transform and the stationary wavelet transform based techniques for the fusion of multi-focus images', *Emerging Trends in Electronics & Communication*, vol. 1, no. 2, pp. 1-9.

Ryo, M, Angelov, B, Mammola, S, Kass, JM, Benito, BM & Hartig, F 2021, 'Explainable artificial intelligence enhances the ecological interpretability of black-box species distribution models', *Ecography*, vol. 44, no. 2, pp. 199-205.

Salcedo-Sanz, S, Rojo-Álvarez, JL, Martínez-Ramón, M & Camps-Valls, G 2014, 'Support vector machines in engineering: an overview', *Wiley Interdisciplinary Reviews: Data Mining and Knowledge Discovery*, vol. 4, no. 3, pp. 234-67.

Saleem, R, Yuan, B, Kurugollu, F, Anjum, A & Liu, L 2022, 'Explaining deep neural networks: A survey on the global interpretation methods', *Neurocomputing*, vol. 513, pp. 165-80.

Saraiya, M, Glanz, K, Briss, PA, Nichols, P, White, C, Das, D, Smith, SJ, Tannor, B, Hutchinson, AB & Wilson, KM 2004, 'Interventions to prevent skin cancer by reducing exposure to ultraviolet radiation: a systematic review', *American Journal of Preventive Medicine*, vol. 27, no. 5, pp. 422-66.

Selvakumar, B & Muneeswaran, K 2019, 'Firefly algorithm based feature selection for network intrusion detection', *Computers & Security*, vol. 81, pp. 148-55.

Sharma, E, Deo, RC, Prasad, R & Parisi, AV 2020, 'A hybrid air quality early-warning framework: An hourly forecasting model with online sequential extreme learning machines and empirical mode decomposition algorithms', *Science of the Total Environment*, vol. 709, pp. 1-23.

Shi, Q, Abdel-Aty, M & Lee, J 2016, 'A Bayesian ridge regression analysis of congestion's impact on urban expressway safety', *Accident Analysis & Prevention*, vol. 88, pp. 124-37.

Sivamani, RK, Crane, LA & Dellavalle, RP 2009, 'The benefits and risks of ultraviolet tanning and its alternatives: the role of prudent sun exposure', *Dermatologic Clinics*, vol. 27, no. 2, pp. 149-54.

Sterenborg, H & VanDerLeun, J 1987, 'Action spectra for tumorigenesis by ultraviolet radiation', in *Human Exposure to Ultraviolet Radiation*, pp. 173-92.

Stevenson, E, Rodriguez-Fernandez, V, Minisci, E & Camacho, D 2022, 'A deep learning approach to solar radio flux forecasting', *Acta Astronautica*, vol. 193, pp. 595-606.

Takenaka, H, Nakajima, TY, Higurashi, A, Higuchi, A, Takamura, T, Pinker, RT & Nakajima, T 2011, 'Estimation of solar radiation using a neural network based on radiative transfer', *Journal of Geophysical Research: Atmospheres*, vol. 116, no. D8, pp. 1-26.

Torres, JF, Gutiérrez-Avilés, D, Troncoso, A & Martínez-Álvarez, F 2019, 'Random hyper-parameter search-based deep neural network for power consumption forecasting', *Advances in Computational Intelligence: 15th International Work-Conference on Artificial Neural Networks, IWANN 2019, Gran Canaria, Spain, June 12-14, 2019, Proceedings, Part I 15*, Springer, pp. 259-69.

Turner, J, Igoe, D, Parisi, AV, McGonigle, AJ, Amar, A & Wainwright, L 2020, 'A review on the ability of smartphones to detect ultraviolet (UV) radiation and their potential to be used in UV research and for public education purposes', *Science of the Total Environment*, vol. 706, pp. 1-48.

Van der Velden, BH, Kuijf, HJ, Gilhuijs, KG & Viergever, MA 2022, 'Explainable artificial intelligence (XAI) in deep learning-based medical image analysis', *Medical Image Analysis*, vol. 79, pp. 1-21.

Vilone, G & Longo, L 2021, 'Notions of explainability and evaluation approaches for explainable artificial intelligence', *Information Fusion*, vol. 76, pp. 89-106.

White, AL & Jahnke, LS 2002, 'Contrasting effects of UV-A and UV-B on photosynthesis and photoprotection of β-carotene in two Dunaliella spp', *Plant and Cell Physiology*, vol. 43, no. 8, pp. 877-84.

World Health Organization, World Meteorological Organization, United Nations Environment Programme & International Commission on Non-Ionizing Radiation Protection 2002, *Global solar UV index: a practical guide*, World Health Organization, Switzerland, viewed 02 August 2021, <https://apps.who.int/iris/bitstream/handle/10665/42459/9241590076.pdf>.

Xiao, L, Dong, Y & Dong, Y 2018, 'An improved combination approach based on Adaboost algorithm for wind speed time series forecasting', *Energy Conversion and Management*, vol. 160, pp. 273-88.

Xingjian, S, Chen, Z, Wang, H, Yeung, D-Y, Wong, W-K & Woo, W-c 2015, 'Convolutional LSTM network: A machine learning approach for precipitation nowcasting', *Advances in Neural Information Processing Systems (NIPS)*, Montreal, Canada, pp. 802-10.

Yagli, GM, Yang, D & Srinivasan, D 2019, 'Automatic hourly solar forecasting using machine learning models', *Renewable and Sustainable Energy Reviews*, vol. 105, pp. 487-98.

Zdravković, M, Ćirić, I & Ignjatović, M 2022, 'Explainable heat demand forecasting for the novel control strategies of district heating systems', *Annual Reviews in Control*, vol. 53, pp. 405-13.

Zhai, T & Wang, H 2022, 'Online passive-aggressive multilabel classification algorithms', *IEEE Transactions on Neural Networks and Learning Systems*, pp. 1-14.

Zhang, J, Yi, S, Liang, G, Hongli, G, Xin, H & Hongliang, S 2020, 'A new bearing fault diagnosis method based on modified convolutional neural networks', *Chinese Journal of Aeronautics*, vol. 33, no. 2, pp. 439-47.

Zhang, L, Zhang, B, He, F & Yang, J 2013, 'Impact analyzing based on new method of phase space reconstruction', *2013 IEEE International Conference on Mechatronics and Automation*, IEEE, pp. 587-92.

Zhao, R & He, T 2022, 'Estimation of 1-km Resolution All-Sky Instantaneous Erythemal UV-B with MODIS Data Based on a Deep Learning Method', *Remote Sensing*, vol. 14, no. 2, pp. 1-29.

Zheng, Y, Guo, Z, Zhang, Y, Shang, J, Yu, L, Fu, P, Liu, Y, Li, X, Wang, H & Ren, L 2022, 'Rapid triage for ischemic stroke: a machine learning-driven approach in the context of predictive, preventive and personalised medicine', *EPMA Journal*, vol. 13, no. 2, pp. 285-98.

APPENDIX A

Table A1 Designations of the ultraviolet radiation forecasting models constructed in the three objectives.

	Model Type	Model Designation
Objective 1		
Proposed Model	Hybrid wavelet-Optuna convLSTM	W-O-convLSTM
Benchmarked Models	Non-wavelet-Optuna convLSTM	O-convLSTM
	Non-wavelet-Optuna CNN	O-CNN
	Non-wavelet-Optuna SVR	O-SVR
	Non-wavelet-Optuna PA	O-PA
Baseline Model	Hybrid wavelet-Optuna convLSTM trained on SZA only	W-O-convLSTMsza
Objective 2		
Proposed Model	Hybrid Bayesian ensemble N-BEATS	B-E-NBEATS
Benchmarked Models	Hybrid ensemble LSTM	B-E-LSTM
	Non-ensemble N-BEATS	B-NBEATS
	Non-ensemble LSTM	B-LSTM
	Non-ensemble BRR	B-BRR
Objective 3		
Proposed Model	Enhanced Joint Hybrid Explainable DNN	EJH-X-DNN
Benchmarked Models	Enhanced Joint Hybrid FCN	EJH-FCN
	Enhanced Joint Hybrid ANN	EJH-ANN
	Enhanced Joint Hybrid MLP	EJH-MLP
	Enhanced Joint Hybrid AB	EJH-AB
	Enhanced Joint Hybrid SGD	EJH-SGD
	Enhanced Joint Hybrid DT	EJH-DT

APPENDIX B

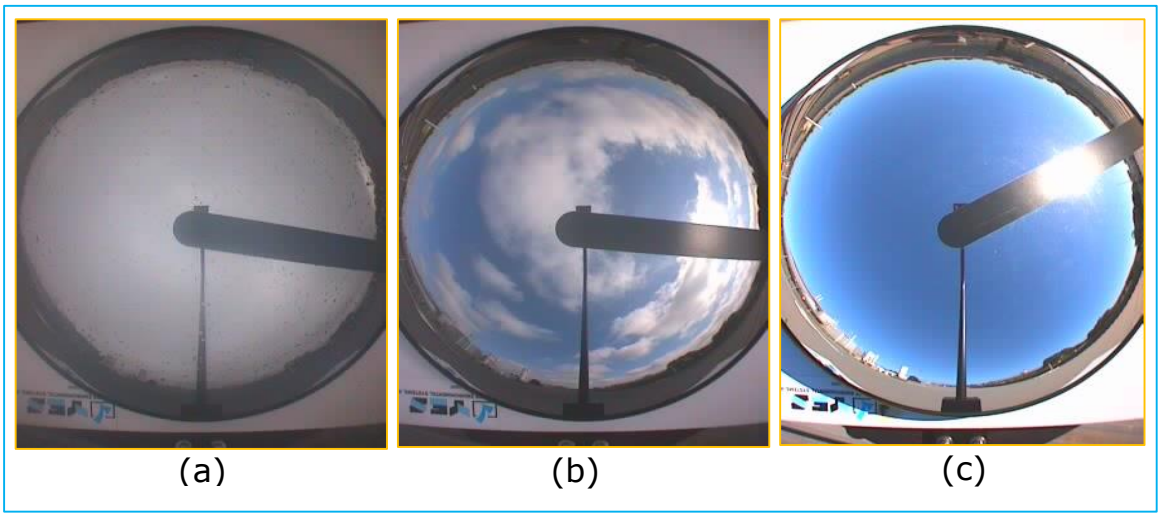

Figure B1 Samples of sky image extracted from the total sky imager showing (a) total cloud cover, (b) partial cloud cover, and (c) no cloud cover.